UNIVERSITY OF OSLO

Department of Physics

ZnO Deposited by Magnetron Sputtering Incorporating Si Nanocrystals

Master's Thesis

Matthew David Schofield

1st June 2011

Abstract

Zinc oxide has attracted a great deal of interest in recent years with a view to potential photovoltaic applications, particularly as a material for transparent conducting electrodes. The material's abundance and low cost make it a potentially attractive alternative to the current standard technology. Silicon nanocrystals have recently been identified as exhibiting properties potentially suitable for multiple exciton generation (MEG), which could theoretically improve the efficiency of solar cells above the thermodynamic limit on the current standard solar cell design.

Silicon-doped ZnO thin films were deposited by a radio frequency co-sputtering technique, using ZnO and Si targets, onto glass substrates and Si wafers. By adjusting the target power ratio, films with various micro-structures could be obtained. This work began with optimisation of the sputtering parameters for deposition of ZnO thin films of ~ 100 nm thickness with a high degree of texturisation and grain sizes $\gtrsim 20$ nm as determined by x-ray diffraction (XRD) and transmission electron microscopy (TEM). Sputter deposition simultaneously from both targets was then performed and XRD, optical transmittance and Hall measurements were used to determine the variation of the resulting films' structural, optical and electrical characteristics with increasing Si/ZnO target power ratio. A Si-doped ZnO film was fabricated with resistivity $\sim 1\times10^{-3}\ \Omega$ cm, carrier concentration of $\sim 10^{20}$ cm^{-3} and transmittance $\gtrsim 80\%$ in the wavelength range $400 < \lambda < 1400$ nm. Finally, TEM imaging techniques were used to confirm the precipitation of Si nanocrystals in a highly doped film.

Acknowledgements

I am grateful to many people who have helped me directly and indirectly in the course of the last two years, culminating in this thesis.

First, my thanks goes to my two supervisors. To Prof. Bengt Gunnar Svensson, for providing me with a stimulating project and for encouragement and very helpful feedback. To Dr. Ramòn Schifano, who was lumbered with the unenviable role of supervising me on a day-to-day basis, for his great patience in introducing me to equipment, scientific concepts and understanding that equipped me for the task. His tireless work in proof-reading drafts of this thesis and general positive attitude were also essential and greatly appreciated.

Several colleagues and members of staff at MiNaLab have helped me in practical ways. In particular, Protima Rauwel, with the Centre for Material Science and Nanotechnology (SMN), who provided the TEM images and much help with their analysis and interpretation. Thanks go to Victor Bobal for introducing me to several pieces of equipment and practises in the clean room, as well as calmly solving technical issues along the way. To Dr. Esben Lund and Vishnukanthan Venkatachalapathy for valuable training, assistance and discussion regarding XRD measurements, Dr. Lasse Vines, for performing SIMS measurements and Spyridon Diplas for XPS measurements.

I owe much gratitude to my fellow master students - colleagues that have become great friends: Per Lindberg, Frode Kløw and Anne Skogstad. They have played a large role in making these last two years so enjoyable through interesting and entertaining discussions, both on- and off-topic.

Finally, to my incredibly supportive family and to my fiancée, Elise, for always believing in me more than I do myself.

Contents

Chapter 1

Introduction

On planet Earth, we receive far more energy from the Sun than we could ever conceivably make use of. The challenge, of course, is to collect it and to harness it to do useful work. Mankind has been making use of solar energy for household heating since the Egyptians in 7th century B.C.[1]. However, in today's society, to have any chance of helping reduce our dependence on fossil fuels, an energy source must be able to provide us, reliably, efficiently and cheaply, with electricity. Solar photovoltaic (PV) technology has come a long way since Alexandre-Edmund Becquerel first discovered the photovoltaic effect in 1839 and the first recognisable solar cell was described by Charles Fritz in 1883[1]. Today's industry standard solar cells reach efficiencies up to 24 %, whilst novel cell designs have been developed in laboratories that are capable of over 40 % efficiency. Whilst the PV industry is well established and has seen massive growth in recent years, it still represents a modest market share when compared with fossil fuel based energy generation and even other renewable technologies such as wind power. For PV to become a significant player in the world energy market, dramatic decreases in manufacturing costs and increases in device efficiency must be realised. This may be best achieved through alternative solar cell technologies.

Zinc oxide (ZnO) has been the subject of a great deal of research in recent years in terms of its potential suitability for PV applications, particularly as a transparent front contact for solar cells. With use of appropriate deposition parameters and impurities,

thin films of ZnO can be made to be simultaneously highly transparent and conductive and can be cheaply deposited over large areas. The most established technology for transparent electrodes is based on indium tin oxide (ITO), but indium is a material in short supply and is increasingly expensive. ZnO has the major advantages of abundance and low cost and so is an attractive prospect as a replacement, among other potential applications.

The aim of this thesis is twofold: to investigate the electrical, optical and structural effects of deposition parameters and silicon doping in magnetron sputtered ZnO thin films and to induce precipitation of silicon nanoclusters in ZnO matrices by further increasing the Si content. The work progressed initially by structural and optical optimisation of the ZnO matrix through the deposition parameters. Co-sputtering with ZnO and Silicon targets was then attempted, systematically varying the Si content to find the optimum doping concentration and then increasing it further until Si nanocrystals formed and could be observed.

The optimisation of electrical and optical properties and incorporation of Si nanocrystals were investigated with two potential solar cell configurations in mind. Both configurations aim to use the ZnO thin films to increase the amount of incident solar energy that is converted into electricity. In the first configuration, the ZnO thin film is used as a transparent conducting electrode, where the unique properties of silicon nanocrystals could theoretically be used to absorb high energy photons, and re-emit two or more photons of lower energy, thus making more efficient use of the higher energy end of the solar spectrum. The second configuration would use the ZnO layer as part of a thin film heterojunction on a multi-junction solar cell, with a nanocrystal superlattice potentially able to increase the photocurrent of the solar cell through multiple exciton generation (MEG).

Initial assessment of films deposited by sputter deposition was performed using a photo-spectrometer to measure transmittance as a function of wavelength and through X-ray diffraction (XRD) measurements to gain information about the crystal structure. Resistivity and other electrical properties were determined using a 4-point probe and

Hall measurement techniques. Transmission Electron Microscopy (TEM) techniques were used to image the structure of the samples and observe the Si nanocrystals.

Chapter 2

Background

This chapter begins by introducing some basic solid state physics, which is mostly based on Kittel[2] and Nelson[3]. This encompasses the structure of solid materials, leading to the structural and electronic properties of semiconductors and what happens when different semiconductors are brought into contact. This provides a theoretical background for the subsequent discussion of the physics of solar cells, which describes the photovoltaic process before going on to discuss the design of solar cell modules and the limitations of current technologies. The concept of *multiple exciton generation* is then introduced as a theoretical background for some potential future applications of the the material and techniques investigated in this project. Some structural and electronic properties of ZnO are given and finally, relevant previous work in the area is also summarised and discussed.

2.1 Solid State Physics

2.1.1 Crystal Structure

Solid materials are structurally defined either as crystalline or amorphous. The distinction between the two is in the range over which the materials constituent building blocks are identically and repetitively ordered. A crystal is made up of building blocks consisting of one or more atoms called a *basis*. A material is said to possess an *ideal*

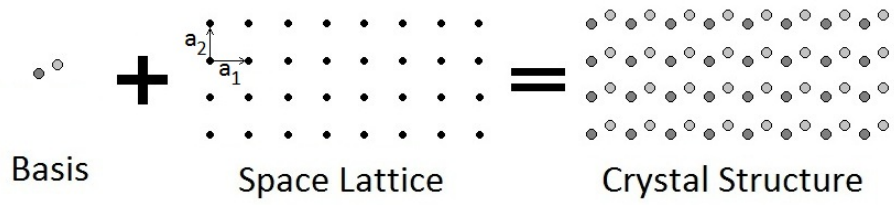

Figure 2.1: The mapping of the basis onto a two dimensional space lattice resulting in a crystal structure.

crystal structure if it consists of a regular repetition of the basis, unchanging throughout its spacial extent. In an amorphous material on the other hand, the bonds between the constituent atoms or molecules are oriented randomly or with only very short range order.

The science of crystallography describes crystal structures mathematically by mapping the basis onto a regular array of points in space, called the *space lattice*, as in figure 2.1. The space lattice in the figure happens to be a two-dimensional square lattice but there are many types of lattice. They are defined by vectors (a_1 and a_2 in this case) which translate one lattice point onto the next and by the angle between those vectors (90 degrees in this case). The vectors are chosen such that upon translation by an integer multiple of the vectors, the surroundings are identical, and they are called *primitive* when they are the smallest possible vectors for which this is the case. All lattice types possess some degree of rotational symmetry under one or more rotations from the following list: 2π, $2\pi/2$, $2\pi/3$, $2\pi/4$ and $2\pi/6$. In three dimensions, there are 14 distinct lattice types, called *Bravais Lattices*, which are divided into *systems* such as cubic, hexagonal and orthorhombic. It is often convenient to pictorially represent a crystal structure with a *cell* (sometimes called a unit cell). A cell is a volume of space containing part of the crystal structure that is chosen such that repetition of that cell by appropriate crystal translation operations will produce the entire crystal structure and fill all space within it. A *primitive cell* is the cell, chosen as described, but with the smallest possible volume for a given lattice. Each lattice type is generally represented by a *conventional* cell, which may or may not be the primitive cell for that lattice type

- an issue of clarity.

Crystal planes are defined mathematically by *Miller indices*. The indices stem from the positions at which the plane intercepts the three Cartesian axes, with respect to the lattice vectors. The reciprocal of these interception points are taken and then changed to the smallest three integers without changing the ratio between them. The result is three integers in parentheses, e.g. a plane with intercepts at positions 2, 2 and 4 would result in the Miller indices *(221)*.

2.1.2 Semiconductors

Crystalline materials can be further subdivided into categories based on their electronic properties. Crucial to a materials ability to generate electricity from light is the concept of an energy *band gap* - a discontinuity in the allowed energy states for electrons in the material. All crystals have an energy gap, but only semiconductors, as opposed to metals and insulators, possess appropriate properties for photovoltaic action.

2.1.2.1 Energy Bands

In Quantum Mechanics (QM), electrons are treated as waves, which essentially represent the probability of finding an electron at a given position. QM tells us that atomic electrons can only occupy discrete energy levels called *orbitals*, and that there are rules governing the occupation of those orbitals. The *Pauli Principle* is key, stating that no two electrons in a bound system can have identical quantum numbers. Thus, only two electrons can occupy a given energy level, with spin quantum numbers $\pm 1/2$. These energy levels are calculated using the Schrödinger equation. When atoms are brought together to form molecules, *molecular orbitals* are formed - one slightly above and one slightly below the original atomic orbital in terms of energy. When more and more atoms are added, the energy levels continue to split into more and more levels until they begin to resemble continuous energy bands. These bands are separated by energy gaps, which are ranges of energy for which there are no electron states. These represent forbidden energy regions for electrons.

The energy distribution of the bands, the gaps between them and their electronic occupation, depend on the atoms that make up the solid and the nature of their bonding. Herein lies the distinction between metals, semiconductors and insulators. A absolute zero temperature, the lowest occupied band is called the *valence band* (VB) and the highest occupied band is called the *conduction band* (CB). If at absolute zero, the CB is partially occupied, then the material is a metal since it can readily conduct electrical charge upon application of an electric field. If however, the VB is completely filled and the CB completely empty then no electrons will move in response to a field, since they are all bonded to atoms, and the material is an insulator. A semiconductor is an insulator at absolute zero temperature, but differs from insulators through the size of the band gap. For a semiconductor, a small number of electrons can be thermally excited across the band gap to the CB for a given temperature, resulting in a small conductivity. So the semiconducting state essentially depends on the ratio E_g/k_BT, where E_g is the band gap energy, T is the absolute temperature, k_B is Boltzmann's constant, and the product k_BT is a measure of the thermal energy in the system. Materials that are semiconducting at room temperature typically have a band gap between 0.5 and 3 eV. Silicon, for example, has a band gap of around 1.1 eV.

2.1.2.2 Band Structure

The photovoltaic action of a semiconductor in a solar cell depends on photons being able to excite electrons across the band gap, so we are interested in the maximum energy level in the VB and the minimum in the CB. To work out the energy of atomic orbitals, one solves the Schrödinger equation, with boundary conditions due to the potential provided by the positively charged atomic nucleus. The same goes for a solid material, the difference being that a crystalline solid is modelled as an infinite lattice, which means there is an infinite, periodic array of atomic potentials to take into account. Since a crystal lattice is made up of an infinite repetition of identical cells, there is no one cell where an electron has a greater probability of being found. Thus the electron probability distribution, or wave function, takes on a periodic, non-localised form, throughout the

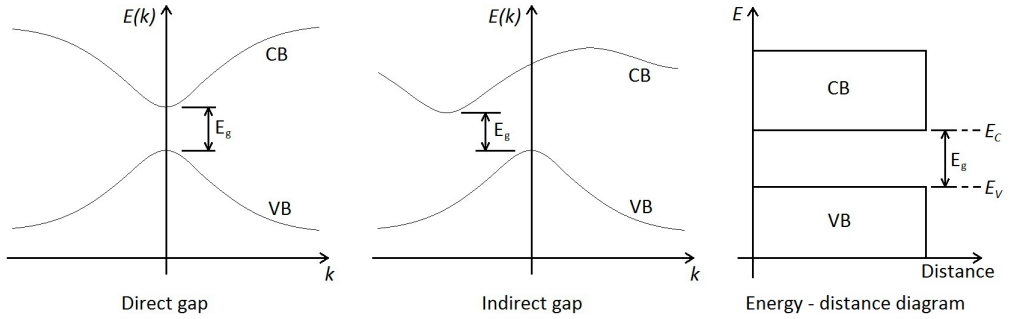

Figure 2.2: Simplified band structure diagrams showing direct and indirect energy band gaps and an energy - distance diagram. E_g is the fundamental band gap.

spacial extent of the lattice. The wave function of an electron in a crystal lattice is described mathematically as a *Bloch function* (equation 2.1), which is the product of two terms, one containing the periodicity of the lattice, u_{ik}, and the other being a plane wave. Each Bloch wave function at a given spacial position, r, is indexed by a particular energy band that originated from a particular atomic orbital, i, and a wave vector, k:

$$\psi(k, r) = u_{ik}(r)e^{ik.r} \tag{2.1}$$

Solving the Schrödinger equation using Block functions results in a continuous set of solutions *E(k)* in each energy band i. These are often plotted against k, forming the *energy band structure*. The wave vector k has units of m^{-1} and is directly related to the momentum of the electron. Depending on the symmetry of a given crystal lattice, the maximum energy state in the VB and the minimum energy state in the CB may or may not occur at the same value of k, as shown in figure 2.2. The difference in energy between the VB maximum and CB minimum is called the *fundamental* band gap. For a direct band gap, a photon with energy $\geq E_g$ alone is sufficient to promote an electron from the VB to the CB. For an indirect band gap however, such a promotion requires a change in momentum, since momentum is a conserved quantity in a crystal. The momentum must be supplied by a phonon, a lattice vibration, and this extra requirement means that such a transition has a lower probability in an indirect band gap semiconductor.

2.1.2.3 Carrier Generation in Semiconductors

Intrinsic Semiconductors Electrical conduction requires that electrons occupy some energy levels in the conduction band, such that they are free to move in response to an applied electric field. To work out or describe the distribution of electrons in a crystal requires two key functions. The first, called the *density of states*, is used to calculate how many quantum states are available for a given energy. This function takes the Pauli principle into account, because there are only two energy states available for each value of the quantum number k as previously discussed. *Fermi Dirac* statistics are then employed to determine which of these states are occupied by electrons at a given temperature under conditions of thermal equilibrium. In this context, the *Fermi energy*, E_F can be defined as the highest occupied energy state at absolute zero temperature. The Fermi Dirac distribution function gives the probability that an electronic state with energy E will be occupied at temperature T:

$$f_0(E, E_F, T) = \frac{1}{e^{(E-E_F)/k_bT} + 1} \tag{2.2}$$

It can be seen that at absolute zero temperature, for energies $E \leq E_F$, $f_0 = 1$, meaning that all available states below E_F are occupied. Conversely, for energies $E > E_F$, $f_0 = 0$, meaning that all available states above the Fermi level are unoccupied. The Fermi Dirac distribution is therefore a step function at absolute zero. At finite temperatures however, some states above the Fermi energy will be occupied, leaving some states below the Fermi energy vacant.

When electrons are excited across the band gap, as in the case of a semiconductor at finite temperature, they leave a net positive charge behind in the form of an unsatisfied bond or vacancy. An applied electric field can cause an electron from an adjacent bond to fill the vacancy, leaving behind a new positively charged vacancy. Though it is the electrons that are moving, it is more convenient, conceptually and mathematically, to consider the positive vacancy as mobile, moving in the opposite direction to the CB electrons in response to an electric field. In fact, the mobile vacancy is treated as a quasi particle, called a *hole*, with particle-like properties such as mobility and effective

mass, analogous to the electron in the CB. The concentration of electrons in the CB can be found from the integral

$$n = \int_{E_C}^{\infty} g_c(E) f_0(E, E_F, T) dE \tag{2.3}$$

and similarly for holes in the VB,

$$p = \int_{-\infty}^{E_V} g_v(E) f_0(E, E_F, T) dE \tag{2.4}$$

where $g_c(E)$ and $g_v(E)$ are the density of available states in the CB and VB respectively and E_C and E_V are the conduction and valence band edges respectively, as in figure 2.2.

In the treatment thus far, we have only discussed *intrinsic* semiconductors - ideal, pure semiconductors, with no defects or impurities. Since the VB is fully occupied and the CB fully empty of electrons at absolute zero, the Fermi energy level is somewhere within the band gap. The position of the Fermi level for the intrinsic semiconductor in equilibrium is often referred to as E_i, the *intrinsic potential energy*. For intrinsic semiconductors, it is usually reasonable to assume that it is far from the band edges, such that $E_C - E_i \gg k_B T$ and $E_i - E_V \gg k_B T$. This is called the *Boltzmann approximation* allowing use of approximate forms of the Fermi Dirac function, equation 2.2, such that in the CB:

$$f_0(E, E_F, T) \approx e^{(E_F - E)/k_B T} \tag{2.5}$$

and in the valence band:

$$f_0(E, E_F, T) \approx 1 - e^{(E - E_F)/k_B T} \tag{2.6}$$

This simplifies equations 2.3 and 2.4 such that they can be evaluated:

$$n = N_C \exp\left(\frac{E_F - E_C}{k_B T}\right) \tag{2.7}$$

and

$$p = N_V \exp\left(\frac{E_V - E_F}{k_B T}\right) \tag{2.8}$$

where N_C and N_V are the *effective density of states* in the CB and VB respectively. A key result is that the product np is found to be a constant of the material. This product

defines the *intrinsic carrier density*, n_i, the concentration of electrons in the CB and, equally, the concentration of holes in the VB for an intrinsic semiconductor in thermal equilibrium:

$$n_i^2 = np = N_C N_V e^{-E_g/k_B T} \tag{2.9}$$

More rigorous derivations are available in many texts such as Kittel[2] and Nelson[3].

Defects and Doping Though electronic and photovoltaic devices use very high quality semiconductor crystals, there are always structural defects at non-zero temperatures. Defects can be categorised as zero-dimensional, 1D, 2D or 3D. Zero-D defects are called point defects and do not extend in any direction. 1D, 2D and 3D defects are called line, area and volume defects respectively. The point defect is the most interesting type for electrical conduction in semiconductors. These come in three main varieties, the simplest being a *vacancy*, which is where an atom is missing from a lattice site. Similarly, another point defect is an atom positioned in the space between lattice sites. This is called an *interstitial*, or more precisely, a *self*-interstitial if the atom is of an intrinsically present element in the material. Vacancies and self-interstitials are intrinsic defects, in that they exist even in the purest, most perfect semiconductor crystals at nonzero temperatures. The equilibrium concentration of intrinsic defects depends exponentially on the temperature[4].

Defects can also be introduced deliberately to influence the electrical properties of the material. The conductivity of a semiconductor is determined by the concentration of conduction electrons and holes and by their mobility:

$$\sigma = q\mu_n n + q\mu_p p \tag{2.10}$$

where μ_n and μ_p are the mobilities of electrons and holes respectively and q is the elementary charge. As previously mentioned, the concentration of conduction electrons, and therefore conductivity in an intrinsic semiconductor at room temperature, is low. Introducing small concentrations of impurities can be used to increase the conductivity. Take silicon for example, which is a group IV element, meaning that it has four electrons

in its outer electron shell. In an intrinsic silicon lattice, all four valence electrons are involved in covalent bonds with adjacent silicon atoms, and are therefore unable to move in response to an external electric field. If some atoms of a group V element such as Phosphorus are introduced and substitute for silicon atoms in some lattice sites, there will be one extra electron in each case that is not occupied by covalent bonds. Such an impurity is referred to as a *donor* since it donates extra electrons. This extra electron is only bound to its atom by a single bond, requiring less energy for it to be broken, promoting the electron into the conduction band. This has the effect of introducing an energy level within the band gap, close to the CB edge (E_C). Conversely, introducing an impurity from group III of the periodic table would result in one unsatisfied bond. This is called an *acceptor* impurity as this unsatisfied bond will readily accept an electron from another bond, leaving behind a hole. This has the effect of introducing an energy level within the band gap, close to the valence band edge (E_V). These new energy levels are localised, since the concentration of donors or acceptors is generally small ($< 10^{19}$ cm^{-3}) relative to the concentration of the native species ($\sim 10^{23}$ cm^{-3}), resulting in discrete levels as opposed to the continuous bands that are formed by the lattice. Deliberately introducing impurities in this way is called *doping* and a doped semiconductor is called an *extrinsic* semiconductor. Figure 2.3 illustrates doping with impurities and the positions of the resulting donor and acceptor energy levels.

Doping with *donor* atoms is called *n type* doping (since the primary charge carriers are negatively charged). At absolute zero temperature, all of the donor energy states are occupied, and thus, the Fermi level moves to a position between E_d and E_C. This effect is important when junctions are formed, as discussed in section 2.3 on page 18. Generally, *dopant* elements are chosen such that effectively all of the donor/acceptor states will be ionised at room temperature. When the donors are all ionised, E_F moves to a position below E_d as shown in figure 2.3 *c)*. Typically the intrinsic carrier concentration is low at room temperature, so the carrier concentration in the doped semiconductor is

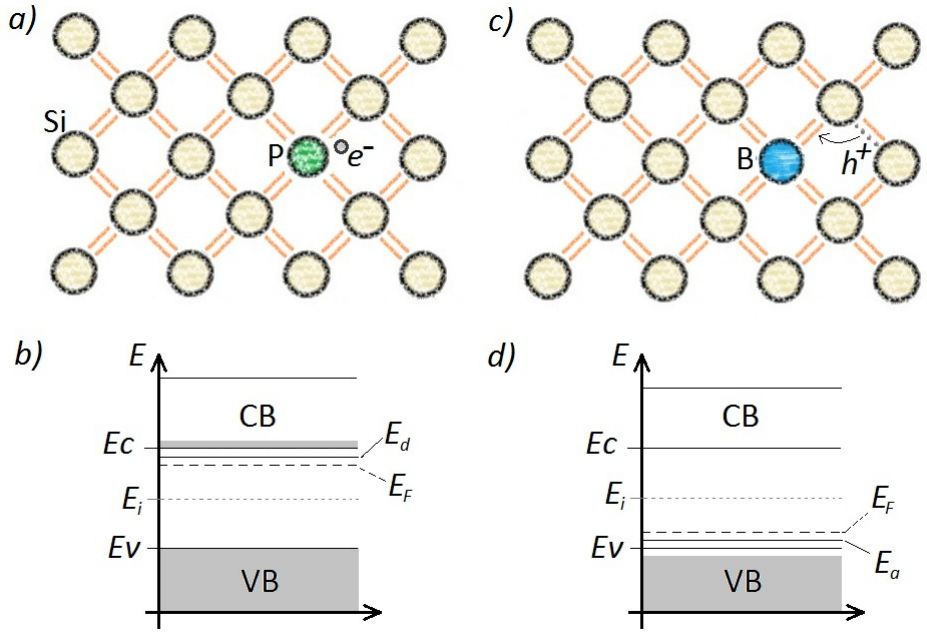

Figure 2.3: Doping: *a)* A phosphorus atom (periodic table group V) has been introduced into a Si lattice (group IV). This acts as a *donor*, since it has one electron left over after all four covalent bonds are made. The extra electron requires less energy to be removed from its Coulombic bond with the P atom and become a charge carrier in the conduction band. *b)* indicates the position (E_d) of the donor energy level, close to the CB edge. In *c)* a boron atom (group III) has been introduced. Having only three valence electrons, this leaves one unsatisfied bond to an adjacent Si atom. When an electron from a neighbouring bond moves in to occupy the unsatisfied bond, it leaves behind a hole ($h+$). The newly ionised boron atom represents a higher energy than the highest level in the valence band and so adds an *acceptor* energy level (E_a) within the energy gap, close to the VB edge as shown in *d*). The donor and acceptor energy levels move the Fermi energy away from its intrinsic position, E_i, up close to the CB edge and down close to the VB edge, respectively. The shaded regions of *c)* and *d)* represent states occupied by electrons at room temperature when all donor and acceptor states are ionised.

effectively the same as the concentration of dopant atoms,

$$n \approx N_d \tag{2.11}$$

and is therefore greatly increased. Using equation 2.9 we can see that the concentration of holes is much smaller:

$$p = {}^{n_i^2}/_{N_d} \tag{2.12}$$

For this reason, electrons in n type semiconductors are called the *majority* carriers, and holes the *minority* carriers. The greatly increased concentration of conduction electrons in n type semiconductors raises the conductivity over the intrinsic value, as can be deduced from equation 2.10.

Doping with *acceptor* atoms is called *p type* doping (since the majority carriers are now positively charged holes). The Fermi level is now forced into a position between E_a and E_V at absolute zero (or just above E_a at room temperature, as shown in figure 2.3 *d)*). In this case, the density of holes is approximately equal to the concentration of acceptor atoms:

$$p \approx N_a \tag{2.13}$$

and

$$n = {}^{n_i^2}/_{N_a} \tag{2.14}$$

Degenerate Semiconductors When a semiconductor is heavily doped, the donor or acceptor energy states are no longer localised since the donor and acceptor atoms become closer together with higher concentration. As a result, the impurity states, located within the forbidden region, split and form bands (analogously to the formation of a crystalline solid), which eventually merge with the *CB* or *VB*, in the case of *n*- or *p*-type doping respectively. This effect is illustrated in figure 2.4. Conductivity is greatly increased, resembling the behaviour of a metal, since the Fermi energy is in the CB and states there are always occupied - thus, to a first approximation, conductivity and carrier concentration become independent of temperature. The optical bandgap also increases, causing a blue-shift in the absorption edge, since incoming photons must

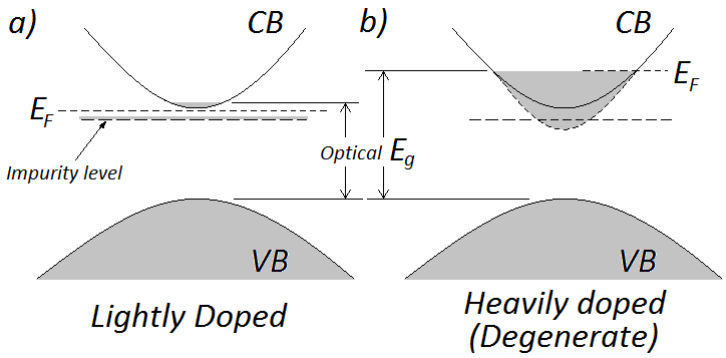

Figure 2.4: Energy band diagrams for an n-type semiconductor in the case of *a)* light doping and *b)* heavy doping. Shaded regions represent occupied states. The *optical* E_g is the energy that an incoming photon must posses in order to excite a valence electron into an available state in the *CB* and so is sometimes referred to as an *effective band gap*.

have enough energy to excite valence electrons into the available states above the new Fermi energy. This is known as the *Burstein-Moss Effect*[5]. These phenomena are important for TCOs as will be discussed in section 2.4.2.3.

2.2 Properties of Zinc Oxide

What follows is a brief summary of the relevant structural, and electrical properties of ZnO, particularly sputtered ZnO. The text by Morkoç and Özgür[6] is the source of much of the information, amongst other articles which are referenced individually.

2.2.1 Structure

ZnO is a group II-VI binary compound semiconductor, which crystallises in the hexagonal wurtzite (Wz) structure under normal ambient conditions[6]. The Wz ZnO unit cell is shown in figure 2.5. It belongs to the space group $P6_3mc$, in the Hermann-Mauguin notation, and has lattice parameters $a = b = 3.2495 \pm (0.00002)$ Å and $c = 5.2069\ (\pm 0.0001)$ Å as determined by x-ray diffraction by Heller et al.[7]. The lattice is made up of two overlapping hexagonal sublattices consisting of Oxygen and Zinc atoms respectively, displaced in the c-axis by a fraction of the c lattice parameter.

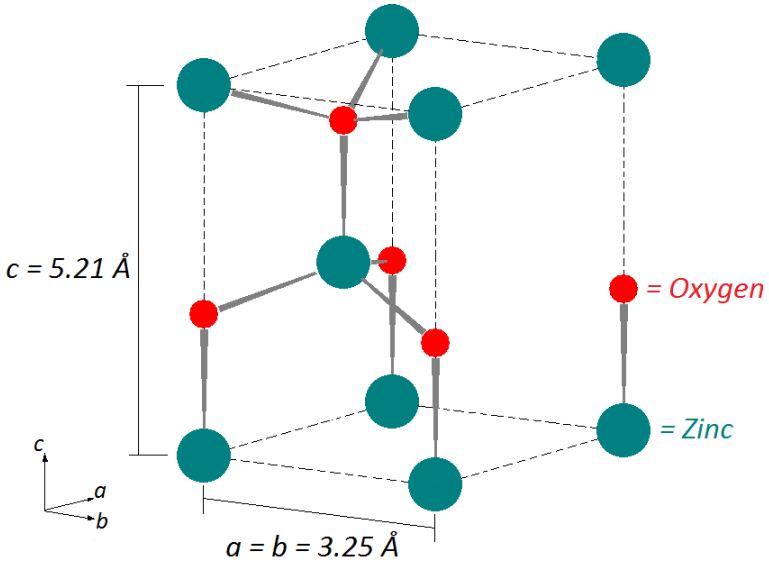

Figure 2.5: A projection of the wurtzite ZnO unit cell. Image adapted from a projection generated using the *Powder Cell* software (version 2.4, Kraus and Nolze).

2.2.2 Electrical Conductivity

It is well known that ZnO is commonly an n-type semiconductor, a fact often attributed to the presence of intrinsic defects. However, the exact mechanism for this is not clear despite much research. Intrinsic defects such as oxygen vacancies, V_O and zinc interstitials, Zn_i can act as donors in ZnO, but the situation is not at all straightforward. Both of these defects have been proposed by different authors to be the prominent donor and there is little consensus. Look et al.[8], for example, put forward Zn_i as the dominating donor in n-type ZnO, but it has a high formation energy. Vanheusden et al.[9] write that though the oxygen vacancy is a shallow donor in ZnO, the intrinsic concentration is not large enough to explain the high carrier densities observed. More recently however, an extensive first-principles investigation into all native defects in ZnO by Janotti et al.[10] finds the Oxygen vacancy to be a deep donor in addition to having low concentration. Either way, it appears that V_O is not the answer, at least not via a conventional donor mechanism. They also conclude that the high formation energy of Zn_i makes it an unlikely source of the observed n-type behaviour, despite being a

relatively shallow donor. The first principles study by Kohan et al.[11] also suggests that none of the native defects in ZnO appear to act as shallow donors with high concentration. Indeed, many now consider unintentional impurity doping, particularly with hydrogen, to be the cause of the n-type behaviour[10]. Hydrogen can act as a shallow donor with a low formation energy and is present in all ZnO growth methods[12].

Thus, n-type doping is relatively easy in ZnO compared with p-type doping, the latter thought to be compensated by intrinsic defects and unintentional impurity doping and being the subject of a great deal of research at present[6]. Many dopants have been shown to lower the resistivity of ZnO, group III elements such as B, Al, Ga and In being the most common at present and it has also been shown that Si, a group IV dopant, can be effective as a donor impurity[13].

2.3 P-n Junctions

Having established the electronic behaviour of semiconductors in isolation in section 2.1.2.3, the next step is to explore what happens when different (or differently doped) semiconductors are brought into contact with each other. In order to produce electricity from light, a material must allow the generation of charge carriers through the absorption of photons. This can occur in semiconductors, as previously discussed, if the incoming photons have energy greater than the band gap for the given semiconductor. If the semiconductor is in isolation however, the electrons will, after a short time, *recombine* with the holes, and thus the charge carriers will be lost. In order for generated charge carriers to be useful, they must be separated by a potential difference, and then removed from the active material, producing a current. In conventional photovoltaic (PV) cells, this is achieved by introducing an asymmetrical resistance to electrons and holes in the material, achieved via a junction between two different or differently doped materials, resulting in a potential that causes electrons to be transported to one contact, while holes are attracted to another. The following discussion of the p-n junction is largely based on Streetman[14] and Nelson[3].

A *p-n junction* is the most common structure for a solar cell's active layer, as well as for many other electronic devices such as diodes, transistors and LEDs. It most commonly consists of separate p- and n-doped regions of a single material in contact - a *homojunction*. As discussed in section 2.1.2.3, the p-type region has a high concentration of holes in the VB and a low concentration of electrons in the CB, whilst the reverse is true for the n-type region. When the regions are in contact, the majority charge carriers near the junction in each region will tend to move into the other region by diffusion - a reaction to the concentration gradient. As electrons leave the n-type region and holes leave the p-type region, they leave uncompensated and immobile positive and negative charges due to the donor and acceptor ions respectively, resulting in a potential difference. Thus an electric field develops, in opposition to the diffusion of majority charge carriers[1], until they cancel each other out. In other words, equilibrium is reached, with the *diffusion current* of carriers exactly equal to the *drift current* due to the electric field. The region over which the uncompensated ionic charges exist is called the *space charge region* or the *depletion region*, since it is depleted of free charge carriers. The potential difference between the p- and n-type regions is almost entirely dropped across the depletion region since outside, in the bulk of the p- and n-type regions, the donor and acceptor ions are compensated by an electron or a hole, leaving them neutral. The Fermi level is constant throughout the material when equilibrium is reached, since there is no net transfer of charge or energy. The separation of the energy bands in the p- and n-type bulk regions is equal to the difference between the Fermi levels when the two regions were independent. The energy band diagram of the p-n junction is given in figure 2.6.

The integrated electric field in the space charge region yields V_{bi}, which is referred to as the *built-in bias* of the junction. This provides the asymmetrical resistance required for the solar cell. The built-in bias is equal to the difference in the shifts of the Fermi

[1]The fundamental definition of an electric field dictates that it acts in the opposite direction to a potential gradient: $E(x) = -\frac{dV(x)}{dx}$.

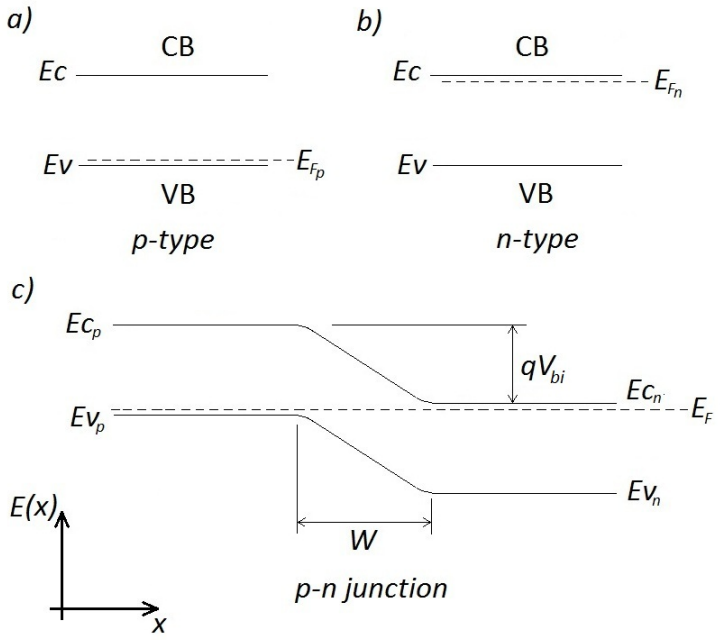

Figure 2.6: Energy band diagrams showing p- and n-type semiconductor regions separately in *a)* and *b)* respectively, and then after being brought into contact in *c)*. The Fermi levels in the two regions, E_{F_p} and E_{F_n} match up causing the band edges to bend in the depletion region, W. A potential, V_{bi} is dropped across this region and is called the *built-in potential* or the *contact potential*.

energy from the intrinsic level, E_i, in the n and p type regions, i.e.

$$V_{bi} = \frac{1}{q}(E_i - E_F) \mid_{p-type} + \frac{1}{q}(E_F - E_i) \mid_{n-type} \tag{2.15}$$

It is convenient to express equations 2.7 and 2.8 in terms of n_i and E_i:

$$n = n_i exp((E_F - E_i)/k_B T) \tag{2.16}$$

and

$$p = n_i exp((E_i - E_F)/k_B T) \tag{2.17}$$

Rearranging equations 2.16 and 2.17 to express them in terms of Fermi level shifts results in the following expression for the built in bias, using equation 2.9 to relate it to the doping levels in each region:

$$V_{bi} = \frac{k_B T}{q} ln\left(\frac{N_d N_a}{n_i^2}\right) \tag{2.18}$$

2.3.1 Under Bias

Application of an external bias, V, across the junction modifies the total potential dropped across the junction,

$$V_j = V_{bi} - V \tag{2.19}$$

assuming that V is positive when a positive external bias is applied to the p-doped region with respect to the n-doped region. This is referred to as *forward bias*, whilst *reverse bias* is the application of a negative external bias to the p-doped region. Thus, a forward bias reduces the size of the potential barrier across the depletion region and a reverse bias increases it. External bias has a similar effect on the depletion region width, and also causes splitting of the Fermi energy level into separate *quasi* - Fermi levels for each of the neutral regions as shown in figure 2.7.

The total current across the junction is given by the sum of the diffusion current of majority carriers and the drift current of minority carriers, which are exactly equal at equilibrium. The diffusion current is the movement of majority carrier electrons in the n-doped region towards the p-doped region in response to the concentration gradient,

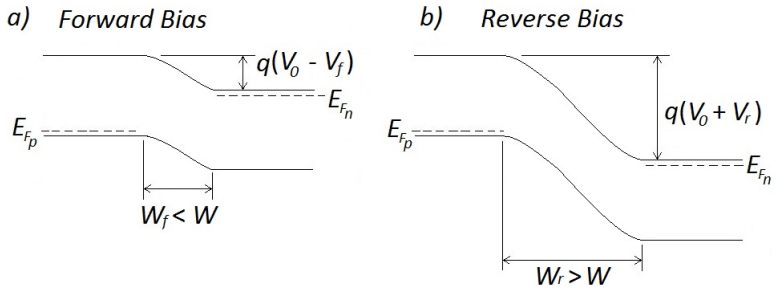

Figure 2.7: Energy level diagrams for *p*-*n* junctions under *a)* forward- and *b)* reverse bias. The depletion widths and electrostatic potentials are given in reference to their equilibrium values, W and V_0 respectively, as shown in figure 2.6.

and visa-versa for majority carrier holes in the *p*-doped region. With no external bias, only a small proportion of majority carriers have enough energy to surmount the built-in potential barrier. When forward bias is applied and the barrier is lowered, this quickly changes and the drift current increases exponentially. Under reverse bias, the barrier becomes too high for any diffusion across the barrier to occur. The drift current is almost independent from the size of the barrier, and therefore the bias voltage. It is limited by the availability of minority carriers, which, in the dark, is determined by thermal generation of electron-hole pairs, and is very small. The result is that the p-n junction has a *rectifying* behaviour, readily allowing the flow of current under forward bias, but not in reverse, as shown in figure 2.8 *b)*. In the language of solar cells, the current response of a diode in the dark is often referred to as the *dark current*, which is approximated by the *ideal diode* equation, and generally expressed in terms of current densities:

$$J_{dark} \approx J_0 \left(e^{qV/k_B T} - 1 \right) \tag{2.20}$$

where J_0 is the drift current density in the dark, called the *diode saturation current density*.

2.3.2 Under Illumination

When light is incident upon the *pn* junction device, electron-hole pairs are created in all regions. Since the concentration of minority carriers is so much smaller than that

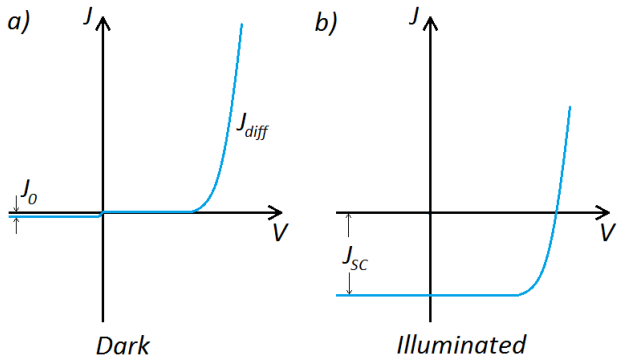

Figure 2.8: The current/voltage relationships for pn junctions, *a)* in the dark, displaying a diode-like response, and *b)* under illumination.

of majority carriers in the respective regions, their resulting increase in concentration is much more significant than that of the majority carriers (both are photogenerated in equal numbers). The minority carriers that are generated within one diffusion length of the depletion region are swept across the junction, increasing the drift current, and therefore changing the current/voltage response in the manner shown in figure 2.8 *b)*, where J_{SC} is the *short circuit current density* - the current that is generated under illumination when no load is present, or when $V = 0$.

2.4 Solar Cells

2.4.1 Summary of Electrical Characteristics

Having introduced the physical electronics of semiconductors and junctions, it is now possible to talk about photovoltaics and how solar cells work in order to provide some context for work on ZnO thin films. Much of this section is based on Nelson[3] and Markvart[15].

The basic function of a solar cell is to absorb incident light, exciting electrons across the band gap to create electron-hole pairs, after which the electrons and holes are separated due to the asymmetric resistance as described in section 2.3, producing a photocurrent. The most useful way to represent the photocurrent is by the *short circuit*

current density, J_{SC}, of the cell (see 'Under Illumination' in section 2.3). A key concept is the *quantum efficiency*, $QE(E)$, which relates J_{SC} to the incident photon spectrum as the probability of creating an electron-hole pair per incident photon:

$$J_{SC} = q \int b_S(E) QE(E) dE \tag{2.21}$$

where b_S is the incident *spectral photon flux density*, or the number of incident photons per second with energy E. When a load is present between the terminals, the current is reduced from the short circuit value by a component acting in the opposite direction that is known as the dark current, as introduced in section 2.3. Thus, the total current density, $J(V)$ is, to a first approximation, the superposition of the photocurrent and the dark current, which oppose each other. By convention, when talking about solar cells as opposed to diodes, the photocurrent is considered positive:

$$J(V) = J_{SC} - J_{dark} = J_{SC} - J_0 \left(e^{qV/mk_BT} - 1 \right) \tag{2.22}$$

where J_0 is the diode *saturation current*, a constant. This is an approximation of the diode equation, with the variable m normally referred to as the *ideality factor* which assumes a value between 1 and 2, representing deviation from ideal diode behaviour in a solar cell. The deviation is due to several factors including recombination in the depletion region, where photogenerated charge carriers recombine with holes before they are able to cross the junction, and series resistance, caused by imperfect electrical contacts between different components of the solar cell. The relation between the current components in the case of an ideal diode ($m = 1$) is shown in figure 2.9. This is the same current response as shown in figure 2.8 *b)*, but with the opposite sign convention.

Isolating the terminals of the cell results in the maximum value of the potential difference, or the *open circuit voltage*, V_{OC}. Since this condition requires that no current is flowing, it is equivalent to the case where the the short circuit current is cancelled out by the dark current. Thus, putting $J_{SC} = J_{dark}$ and solving for V gives an expression for V_{OC}, demonstrating that the voltage is logarithmically dependent on the short circuit

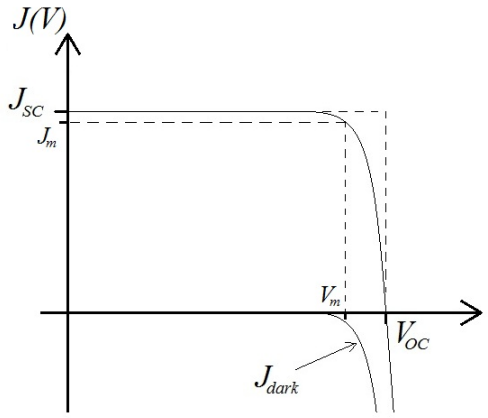

Figure 2.9: Current density versus voltage for a solar cell modelled as an ideal diode under illumination. The maximum power, P_m is given by the area of the inner rectangle.

current and therefore the incident photon flux:

$$V_{OC} = \frac{mk_BT}{q} ln\left(\frac{J_{SC}}{J_0} + 1\right) \tag{2.23}$$

The device operates as a solar cell, producing a photocurrent in the bias range $0 < V < V_{OC}$. Outside this range the device consumes power, rather than generating it. The optimum power density, P_m, for the cell is given by the product of a current density J_m and a voltage V_m as marked in figure 2.9 and this can be used to express the cell's efficiency:

$$\eta = \frac{P_m}{P_s} \tag{2.24}$$

where P_s is the incident light power density. J_{SC} and V_{OC} are more fundamental parameters by which to compare cells. A *fill factor*, *FF*, can be defined which is a measure of how 'square' the $J - V$ curve is, i.e. how closely it matches the outer rectangle in figure 2.9:

$$FF = \frac{J_m V_m}{J_{SC} V_{OC}} \tag{2.25}$$

and this can be used to re-express the efficiency more usefully:

$$\eta = \frac{J_{SC} V_{OC} FF}{P_s} \tag{2.26}$$

Using standard conditions of illumination, solar cell structures can be compared using these key parameters.

2.4.2 Solar Cell Design

2.4.2.1 Standard Design

The current standard solar cell technology is based around p-n monojunctions made from single- and multicrystalline silicon wafers. The wafers are a few hundred microns thick and lightly doped p-type. Single crystal wafers are generally produced using the *Czochralski* process, but sometimes using the more costly *float zone* process, which results in a higher purity material[4]. Multicrystalline wafers are produced by a number of different methods such as casting and ribbon growth[3]. The p-type doping is introduced during the manufacture of the solar grade Si, usually using Boron as a dopant at concentrations of $\sim 10^{16}$ cm^{-3}. The p-type region, referred to as the *base* in analogy with diode terminology, is relatively thick ($\sim 300-500$ μm) to aid absorption, with the light doping intended to increase carrier diffusion lengths. An n-type region is created, usually using *ion implantation* of Phosphorus or by diffusion. This region, called the *emitter*, is much thinner, allowing as much light as possible through to the base, though the thickness must be large enough to avoid high series resistances. High doping levels ($\sim 10^{19}$cm^{-3}) are also required in the emitter to keep series resistances low. These high doping levels result in high carrier recombination in this region and thus, very little carrier collection - hence the desire to keep the emitter region as thin as possible. A textured anti-reflection coating is added to the front surface to aid light trapping and a metal contact applied to the back surface. The front surface contact is achieved via a thin metal grid network.

Dominance Crystalline silicon cells account for roughly 90 % of the photovoltaic solar cell market[16]. This could be considered somewhat surprising since the general consensus at the beginning of the terrestrial PV solar industry (in the mid 1970s) was that crystalline Si solar cells, having been used for space applications, were too expensive for larger scale terrestrial applications[17]. Many assumed that alternative technologies, such as thin films or concentrators, would quickly take over as the future of ground-based PV. However, thanks to government incentive schemes and the resulting ability

for expansion of the market, the cost of manufacturing crystalline silicon solar cells has dramatically fallen, with a 20 % reduction in cost with every doubling of the market. Another major factor for progress towards cost competitiveness was the realisation of the concept of point-of-use, grid connected PV applications[17]. Many advances in manufacturing processes are also responsible, such as the introduction of screen printing for the metallic grid contact, wire wafer sawing and the increasing automation of the whole production line. The rapid progress made in recent decades, as well as the amount of investment in the technology over this time, are contributing factors to the continued dominance of crystalline silicon for PV. The relative simplicity of the device is also an advantage. Many new technologies that aim to overcome its limitations, such as heterostructure cells, introduce significant further manufacturing issues and challenges.

Limitations The *detailed balance limit of efficiency*, published in 1961 by Shockley and Queisser, gives a calculated theoretical limit of around 30 % for p-n junction based crystalline silicon solar cells[18]. The standard PV technology cannot exceed that limit. One contributor to this limitation is the inability to efficiently use the full solar spectrum. Photons with energy less than the band gap energy are not absorbed by the cell, and the excess energy of photons with energy greater than the band gap energy is not used for generating electricity. This is further discussed in section 2.4.2.5 on page 30, along with an approach to improving the situation.

The screen printed metal grid front contact obscures a significant area of the cell's surface. Called *shading*, this effect reduces efficiency since up to 10 % less surface area is available for light absorption[3]. Though reducing the thickness of the metal tracks would reduce this effect, it also increases series resistance, so a compromise must be made.

Though continuous progress is being made in this area, the main obstacle preventing PV solar cells from taking a significant energy market share is still material and manufacturing cost. This is preventing solar generated electricity from eating significantly into the dominance of fossil fuel based electricity generation. For example, the cost

of coal-based electricity is around \$0.04/kWh whilst PV-generated electricity costs in excess of \$0.25/kWh[19]. As a result of the roughly exponential growth of the PV market, manufacturing costs drop by a factor of two every 8-10 years. However, extending the trend into the future, even with this remarkable progress, suggests that PV would only become competitive with coal in 30-40 years[16]. Bringing cost competitiveness forward significantly may require alternative approaches to PV to improve efficiency while keeping costs down.

2.4.2.2 Thin Films

Thin films are loosely defined as having thickness less than a few hundred microns. Due to certain exceptions however, they are perhaps better defined by the nature of their manufacture process - usually physical or chemical vapour deposition. While standard, wafer based solar cells can be made to be quite efficient, the demand on the quality of the material is quite high, resulting in large material and manufacturing costs, as previously discussed, especially in the case of single crystal wafers. The main advantage and the reason for the interest in thin films for PV solar cells is the potential for lower material and manufacture costs. They generally consist of amorphous or polycrystalline structures, and can be deposited relatively easily and cheaply over large areas using chemical- or physical vapour deposition (CVD or PVD) techniques.

2.4.2.3 Transparent Conducting Electrodes

Transparent conducting oxides (TCOs) are essential in many optoelectronic devices, such as flat-panel displays, and they also find application in the field of photovoltaics. They are used in several different configurations, mostly thin film cells such as a-Si, where use of a metal grid contact is impractical, but also in wafer-based configurations, such as the Sanyo HIT cell, the basic structure of which is shown in figure 2.10. First commercialised in 1997, this symmetrical cell configuration uses sputtered TCO layers as both the top and bottom electrodes, with a silver grid contact added on top[20]. An especially thin n-type crystalline Si layer is sandwiched between intrinsic amorphous Si

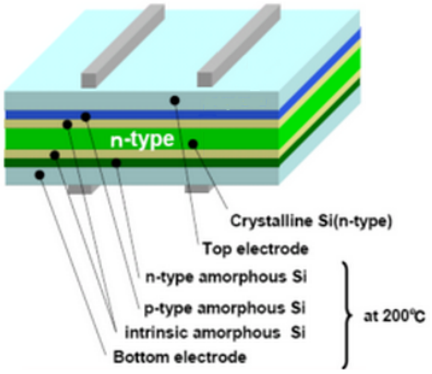

Figure 2.10: The basic structure of the Sanyo HIT solar cell design. Image adapted from the Sanyo web-site[22].

(a-Si) layers, followed by n- and p-type a-Si layers on the illuminated and back sides respectively. This structure has the advantage of using small quantities of material, reducing costs, and low temperature deposition processes as well as above-industry-standard efficiency (22 % in 2008[21]).

Generally speaking, TCO materials are wide band gap, n-type, degenerate, poly-crystalline or amorphous semiconductors[23, 24]. The wide band gap means that the majority of visible and UV light is transmitted and the condition of degeneracy increases the conductivity[2]. Practical TCOs for PV applications generally require resistivity of $\sim 10^{-3}\ \Omega$ cm or less and average transmittance above 80 % in visible wavelengths[23, 24], conditions that can be simultaneously met by degenerate oxide semiconductors such as ITO (Indium doped Tin Oxide) and heavily doped ZnO (common dopants include Ga, Al and, more recently, Si). A major limitation on the properties of TCOs is the mobility - affecting the conductivity of the TCO (see equation 2.10). This is further discussed in section 2.5.

2.4.2.4 Multi-junctions and Heterostructures

Heterostructure solar cell designs provide an opportunity to increase the proportion of incident light that is absorbed by the cell. As opposed to homojunctions, they

[2]See 'Degenerate Semiconductors' in section 2.1.2.3 on page 15.

make use of one or more junctions between different semiconducting materials, called *heterojunctions*, to take advantage of their different band gaps. This is designed to improve the efficiency of the solar cell over that of the standard design, by increasing the range of wavelengths of light that are absorbed. Very large efficiencies have been obtained by heterostructure multi-junction solar cells in laboratories, but they are often prohibitively expensive to produce on a large scale in industry.

2.4.2.5 Nanocrystals and Multiple Exciton Generation

The use of semiconductor nanocrystals exhibiting quantisation effects in PV devices has been a subject of great interest recently since they allow the theoretical possibility of increased solar conversion efficiency significantly above the thermodynamic limit for the standard cell design[25].

As mentioned previously, the theoretical thermodynamic limit on the efficiency of a standard, single-junction, crystalline silicon, PV solar cell is approximately 30 %[18]. One factor that contributes to this limitation is that only a fraction of the solar spectrum is absorbed by the silicon layer in a standard solar cell. If an incoming photon possesses energy less than the band-gap energy, it is unable to excite an electron across the band-gap and is therefore not absorbed. Photons with energy greater than the band gap energy create electron-hole pairs with excess kinetic energy, called *hot carriers*. Unfortunately, this excess energy is quickly lost.

The excess energy of hot carriers can be lost as heat to the crystal lattice via electron-phonon interactions, as shown in figure 2.11 *a)*, or via Auger processes (electron-electron interactions). There are two main approaches to making use of the excess energy. In theory, the carriers could be separated and collected before the energy is lost, resulting in increased solar cell potential, or *photovoltage*. The second option is to increase the *photocurrent* through an 'inverse Auger' process called *impact ionisation* (II)[25].

II can occur in bulk semiconductors such as silicon, creating multiple electron-hole pairs for one incident photon. However, this process has to compete with the rate at which thermal relaxation occurs, which has a time constant on the order of picoseconds

in bulk semiconductors[26]. Also, bulk semiconductors such as Si have indirect band gaps, requiring phonons, as well as photons, to create electron-hole pairs in order conserve momentum. As a result, the threshold energy[3] for II in bulk Si is $\sim 3.5E_g$, which is not useful, since there are very few solar photons with energy above this value (less than 1 %). In addition, the increase in quantum yield above this value in Si occurs very slowly[27, 25].

When the size of a crystalline structure is on the order of a few to tens of nanometres, its electronic structure can, to a good approximation, be described as for a spherical potential well[2], spatially confined in three dimensions. The result is that the energy states are quantised, in a similar way as those for an atom or molecule. This quantisation effect is explained in many quantum mechanical texts, and the relation to nanostructures such as quantum dots is well explained in the text by Owens and Poole[28]. Momentum is not a good quantum number for such a system, effectively making the nanocrystal (or NC) a direct gap semiconductor[4]. Thus, the threshold photon energy for the production of two electron-hole pairs can approach the theoretical minimum of twice the energy gap[27]. In addition, the confinement of charge carriers in a NC results in an increase in the strength of the Coulomb interaction. For II in a bulk material, the initial and final exciton[5] states (before and after II) can be considered separately, by perturbation theory. However, the increased Coulomb strength means that there is a coupling between the initial and final states in the case of II in a NC, resulting in superpositions of single and multiple exciton states. As described in the paper by Shabaev et al. on the theory of multiple exciton generation (MEG) in nanocrystals[29], this increases the rate of Auger processes, including II. MEG is a special case of impact ionisation in nanocrystals, taking the increased exciton binding into account[25]. MEG, or *enhanced impact ionisation* in a quantum dot is illustrated in figure 2.11 *b)*.

[3]The threshold energy is the minimum photon energy required for II to produce additional carriers. It is usually quoted in terms of the band gap energy for the material being discussed.

[4]See section 2.1.2.2 on page 8.

[5]An exciton is defined as an electron-hole pair that is bound by the Coulomb interaction.

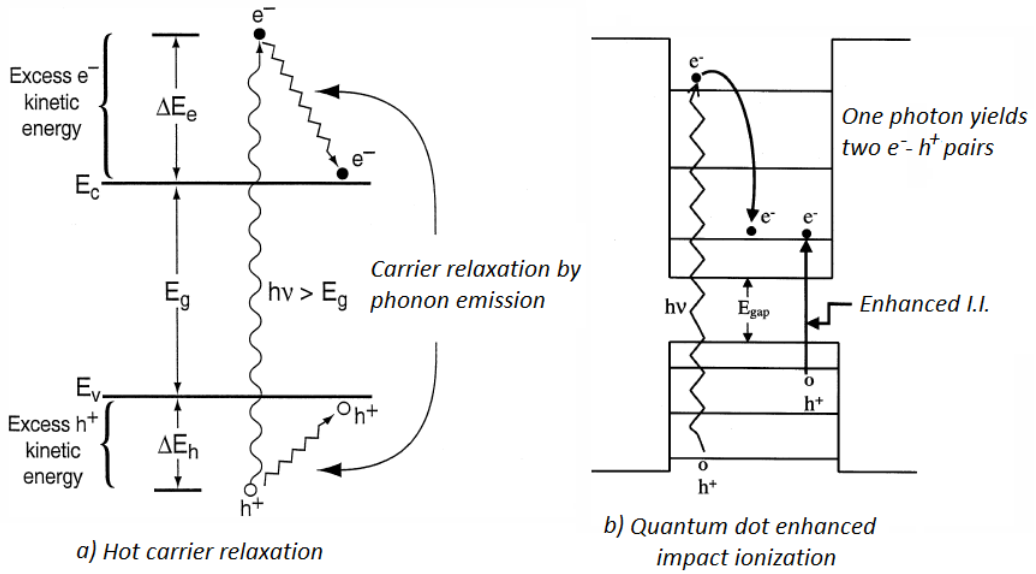

Figure 2.11: *a)* Energy band diagram of the mechanism of thermal relaxation of hot carriers. Figure is adapted from Nozik[30]. *b)* Energy level diagram showing the process of impact ionisation, enhanced by the energy level quantisation in a quantum dot. Figure is adapted from Nozik[31].

The quantisation of the energy levels also reduces the rate of thermal relaxation via phonon interactions, compared to the case of continuous energy bands, since the probability of interactions with phonons of just the right energy for transitions between quantised energy levels is low. This can allow other recombination channels, such as MEG, to become competitive or even dominate in NCs[26]. This is known as the *phonon bottleneck*, and is actually a controversial area of research, since there are several recombination mechanisms that can bypass this effect and many papers are written on the subject, which both confirm and contradict the effect of this phenomenon[25].

The basic concept of using semiconductor quantisation effects for improving solar photo-conversion performance originates from the late 1970s and early 1980s[25]. The first example of observation of efficient MEG in Si nanocrystals was made in 2007 by Beard et al.[27], using colloidal solutions. The suitability of Si for fabrication of MEG-capable NCs is particularly interesting since the vast majority of the PV market is based around Si.

2.4.3 ZnO Solar Cell Configurations

This analysis of sputtered ZnO films with Si nanocrystals is performed with two possible solar cell configurations in mind. Both involve the use of the unique properties of quantum dots for multiple exciton generation.

2.4.3.1 Transparent Conducting Electrodes

One possibility is to use ZnO as a transparent conducting electrode for a solar cell, (perhaps similar in structure to the Sanyo HIT, described in section 2.4.2.3) using Si nanocrystals to produce multiple excitons from each photon having more than twice the energy of the nanocrystalline Si band gap. These excitons would subsequently undergo radiative recombination, thus re-emitting multiple photons per incoming high-energy photon, as depicted in figure 2.12a. This process is called *down conversion*. The result would be an increase in the number of photons arriving at and being absorbed by the active photovoltaic layer - an increased photo-current and therefore thermodynamic efficiency.

2.4.3.2 Thin-Film Heterojunctions

An alternative configuration is to use ZnO as the n-type layer forming a p-n junction with another thin film material (p-type, such as CuO_2), deposited on top of a solar cell, such as a Si wafer cell. In this configuration, shown in figure 2.12b the aim would be to generate multiple excitons in the nanocrystals via the enhanced II/MEG mechanism explained in section 2.4.2.5. In theory, the generated charge carriers would then be collected. At the same time, those photons with energy less than the Si NC band gap energy would pass through this layer to the next active layer. The heterojunction configuration would also result in an increased photocurrent, and some suggest that configurations such as this could push the PV power conversion efficiency in Si based solar cells towards a higher thermodynamic limit of $\sim$ 44 %[26]. This would involve formation of a quantum dot array, or *superlattice* in the ZnO and CuO_2. A superlattice is formed when the distance between quantum dots in the matrix is small enough to

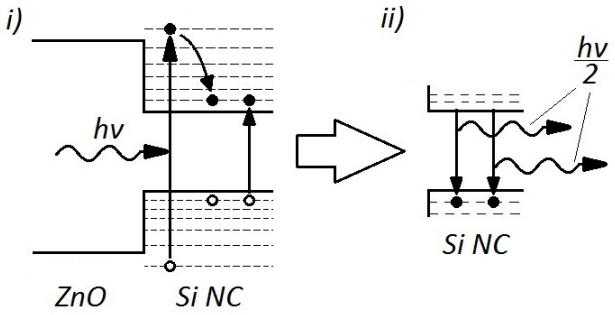

(a) Energy band diagram illustrating the principle for MEG use in a TCO: *i)* A photon with energy hv is absorbed in the ZnO layer, creating an electron-hole pair which subsequently produces a further exciton pair in the Si NC. *ii)* Both exciton pairs undergo radiative recombination, emitting a photon each. Thus two photons are re-emitted from one incident photon.

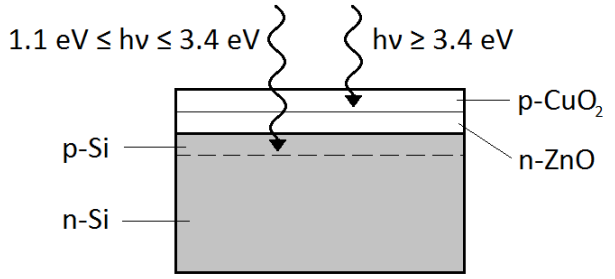

(b) Example of a solar cell structure consisting of a bulk Si homojunction and a thin film ZnO/CuO_2 heterojunction.

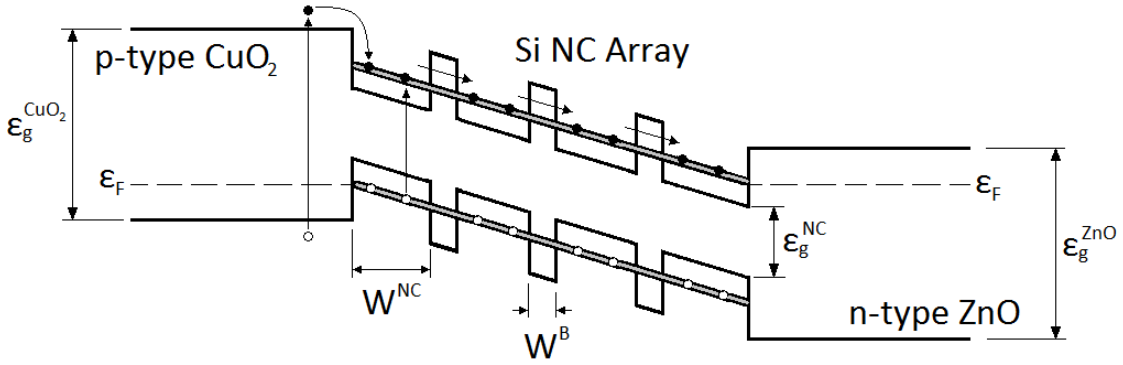

(c) An energy band diagram for a thin-film heterojunction illustrating the MEG and formation of minibands in the silicon NC array.

Figure 2.12: Diagrams for suggested potential applications of ZnO thin films with embedded Si nanocrystals.

permit overlap of electron wavefunctions in adjacent nanocrystals. This causes delocalisation of the energy states, forming energy *minibands*, which can allow carrier delocalisation. The reader is referred to Arthur Nozik's paper on hot electron relaxation dynamics[30] for an in-depth treatment. An illustrative energy band diagram for the thin-film heterojunction can be seen in figure 2.12c. The collection of generated charge carriers poses a problem which is yet to be successfully and efficiently overcome[26].

2.5 Previous Work

This section will briefly summarise some of the key work in the areas of TCOs and MEG for PV applications and will also focus on particularly relevant work in these areas using sputter deposition of ZnO.

2.5.1 Transparent Conducting Electrodes

The first TCO material was a thin film of sputtered cadmium (Cd), oxidised through thermal annealing in air, post deposition. CdO was later deposited using various techniques such as reactive sputtering[32]. A relatively high band gap of 3.35 eV was achieved via the Burstein-Moss effect through heavy doping with Sn, also achieving a very high mobility of 607 [cm^2/Vs] in epitaxially grown films[33]. Despite also having desirable resistivity and optical transmittance values, the potential for applications is highly limited due to the toxicity of Cd[32, 24]. It has also been shown that it is possible to obtain highly transparent and conductive TCOs via intrinsic defects only, including Oxygen vacancies and metal interstitials (i.e. no impurity doping). However, the desirable properties of such intrinsic films have turned out to be unstable at high temperatures and they are deemed ultimately unusable in practical applications[24]. Interest in ITO[6] began in the 1960s, with revelations of highly favourable electrical and optical properties[32]. It is now the most common TCO material with typical res-

[6] Although generally referred to as Sn-doped In_2O_3, ITO is technically an In_2O_3- rich compound of In_2O_3 and SnO_2[34].

istivities of $\sim 1 \times 10^{-4}$ Ω cm (lower values have been obtained in the laboratory)[24]. However, it is well known that the relatively scarce indium is now in increasingly short supply, largely due to its dominance in TCO applications, in the display industry. With demand for such devices rising rapidly, the hunt is on for alternative solutions using cheaper, more readily available and less toxic materials with comparable properties[32].

Despite much research into and various widespread applications of heavily doped TCOs, the doping mechanisms are still not well understood. Since difficulties have been met with reducing the resistivity of TCOs below $\sim 1 \times 10^{-4}$ Ω cm, there has been a great deal of interest in developing the understanding of these mechanisms[34]. One complication with regards to doping mechanisms is that Oxygen vacancies can act as donors in TCOs such as ZnO. Common dopants such as Al, Ga and Si act as donors with their extra valence electron, but they can also getter O in the deposition process. Minami has reported[35] successful doping of ZnO using elements such as Y, Zr, Ti and Hf, which do not donate a valence electron, suggesting that these elements are gettering O and resulting in O vacancies, rather than the conventional extrinsic doping mechanism.

The mobility is a major limiting factor for the conductivity of TCOs, including doped ZnO, representing a key area of present research[23]. Attempting to improve the mobility is not straightforward since there are several scattering mechanisms that can affect the mobility of electrons in the conduction band. Work such as that by Lee[36], on sputtered ITO films, suggests that the dominant electron scattering mechanism in degenerate semiconductors is by ionised impurities and the mobility decreases with increasing carrier concentration above $\sim 10^{20}$ cm^{-3}. This appears to be confirmed by Minami et al.[13] for highly doped ZnO films. However, Elmer et al.[37] suggested that scattering at grain boundaries is the dominant mechanism in ZnO up to carrier concentrations as high as $\sim 2 \times 10^{20}$ cm^{-3}. Work such as the investigation on Al-doped ZnO by Birkholz et al.[38] strongly suggests correlation between the degree of texturisation of the matrix and reduced resistivity exhibited by the film.

Minami et al.[13] investigated Si doped ZnO films and reported resistivity values

as low as 3.8×10^{-4} Ω cm with average optical transmittance of above 85 % in the visible region, therefore nearing parity with the properties of currently used ITO films. There are obvious advantages to using Si with PV applications in mind, since it is highly abundant and the overwhelmingly dominant material in the industry. In addition, group III dopants have been shown to have detrimental effects in application as TCO layers on a-Si based solar cells[13]. These properties were achieved using RF magnetron sputter deposition from a target consisting of a powder mixture of ZnO and SiO_2. They used low substrate temperatures (from room temperature to 250°C) during deposition with no post deposition annealing and the pure Argon gas pressure was kept at 0.8 Pa (≈ 6 mTorr). They found that the carrier concentration in the deposited films and therefore the resistivity were sensitive to the gas pressure, but not to the chosen temperature. Electrical properties for varying SiO_2 content in the target were determined using Van der Pauw Hall measurements and are summarised in figure 2.13a. They find the minimum value of the resistivity to occur with a $1 - 3$ wt% content of SiO_2. In figure 2.13a *ii)*, the Si content is expressed in atomic percent (at%) and the resistivity and carrier concentration are compared with that of Al doped ZnO. Having asserted that Al acts as a donor in ZnO, substituting in a Zn site in the lattice, the comparison is made to suggest that the same mechanism is at work with Si doping. Figure 2.13b shows that the Si doped films had average transmittance above 85 % in the visible wavelength region. A blue-shift with increasing SiO_2 content is apparent and is attributed to the Burstein-Moss effect due to increasing carrier concentration.

2.5.2 Si Nanocrystals for Multiple Exciton Generation in PV Applications

Section 2.4.2.5 introduced and discussed MEG and some of the relevant work. It has also been shown by Lai et al.[39], that it is possible to embed Si nanoclusters in ZnO using sputtering. They used a radio frequency (RF) magnetron co-sputtering system, sputtering simultaneously from high purity ZnO and Si targets and independently varying the RF power on the latter in order to obtain varying degrees of Si content in the

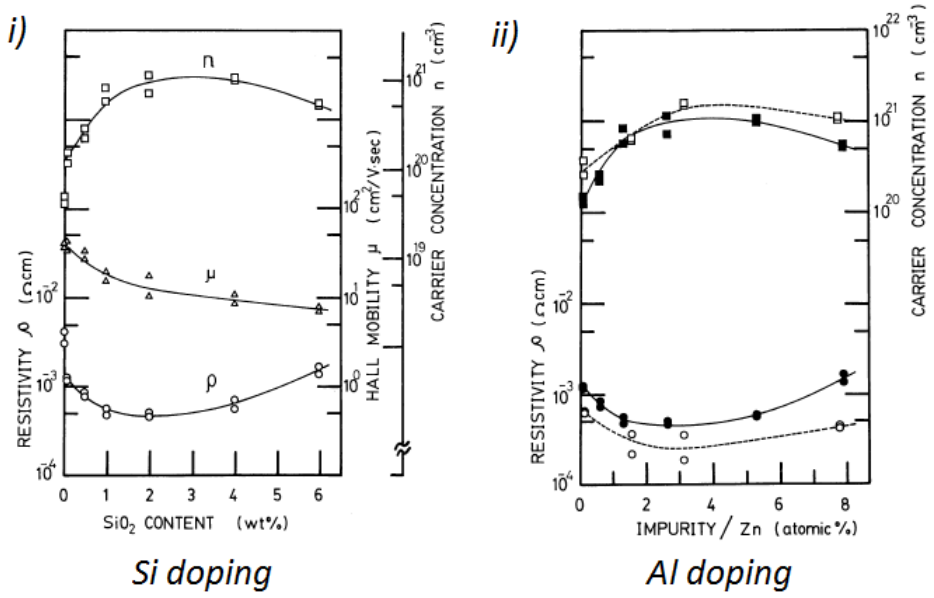

(a) *i)* Resistivity, Hall mobility and carrier concentration variation with ZnO sputtering target SiO_2 content. *ii)* Resistivity (circular markers) and carrier concentration (square markers) variation with Si (filled markers) and Al (unfilled markers) doping content in at%.

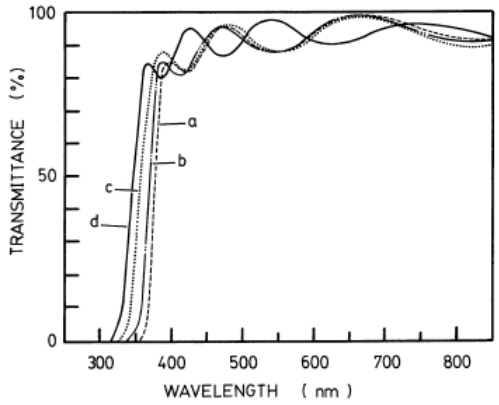

(b) Optical transmittance spectra for ZnO films doped with SiO_2 content of 0.1, 0.5, 1.0 and 2.0 wt% marked *a*, *b*, *c* and *d* respectively.

Figure 2.13: A summary of the results from Minami et al. 1982 using figures taken from their article[13].

resulting ZnO polycrystalline matrix. The deposition was done without substrate heating and with a pure Ar gas flow pressure of 10 mTorr. They studied the key electrical properties of resistivity, carrier concentration and mobility using Van der Pauw Hall measurements, the crystalline structures via XRD scans and observed the Si NCs using high-resolution transmission electron microscopy (HRTEM). A summary of the electrical properties of the six samples of varying Si content, labelled A - F can be seen in table 2.1. The resistivity trend for low Si contents can be seen to agree approximately with the results obtained by Minami et al.[13] in figure 2.13a, in that the lowest resistivity values appear to occur for Si content in the region of a few percent. Lai et al. attributed the reduction in resistivity and increase in carrier concentration with Si content, apparent in samples B - D, to effective donor function of Si. They also observed decreasing carrier concentration and resulting increase in resistivity as Si content is increased above a few percent, and attributed this to excess Si atoms segregating into grain boundaries, no longer serving as effective donors. They observed Si nanoclusters in sample D using high resolution transmission electron microscopy (HRTEM) imaging, as shown in figure 2.14b. From diffraction patterns obtained with the TEM, they also determined that the main reflection index in the nanoclusters corresponded to the Si [011] atomic plane. The XRD patterns they obtained are presented in figure 2.14a and clearly show the ZnO (002) reflection becoming less intense with increasing Si content, disappearing altogether for samples E - F, suggesting degraded crystal quality with Si content above $\sim 25\%$. Si (111), (220) and (311) related reflections we also observed for all samples with Si content, increasing in intensity with Si content. They also observed a SiO_2 related reflection, with Si - O bonds competing with ZnO - O bonds, resulting in reduced crystal quality and degradation of the electrical properties (table 2.1).

Sample	Si target (W)	ZnO target (W)	Compositions Zn:O:Si	Resistivity (Ω cm)	Electron mobility (cm^2/Vs)	Electron concentration (cm^{-3})
A	0	75	48.9: 51.1: 0	1.08×10^{2}	6.24	9.22×10^{15}
B	25	75	47.2: 52.3: 0.5	8.48×10^{-3}	5.72	1.28×10^{20}
C	50	75	44.9: 48.3: 6.8	7.59×10^{-2}	4.04	2.03×10^{19}
D	75	75	43.6: 46.7: 9.7	1.39×10^{-1}	3.02	1.48×10^{19}
E	100	75	35.9: 39.2: 24.9	$2.42 \times 10^{+4}$	0.34	7.54×10^{15}
F	125	75	27.9: 33.6: 38.5	$2.23 \times 10^{+6}$	0.19	1.49×10^{13}

Table 2.1: Summary of the electrical results obtained by Lai et al.[39] on a pure ZnO film (sample A) and 5 samples of co-sputtered ZnO films with varying Si content (samples B - F).

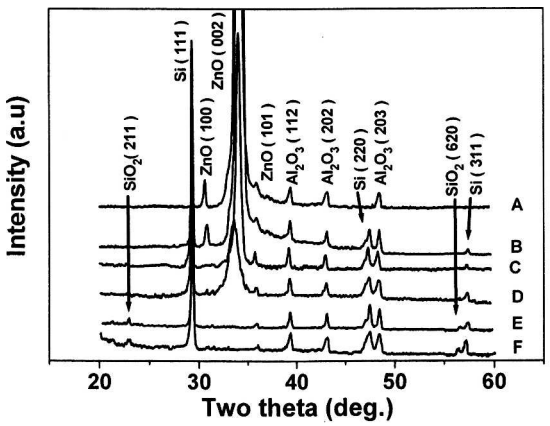

(a) XRD locked coupled scan results for samples A - F.

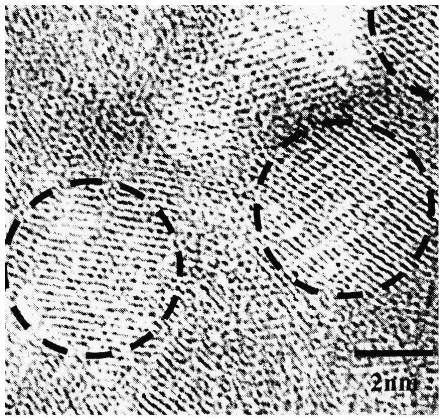

(b) A HRTEM image showing Si nanocrystals (circled) embedded in the ZnO matrix.

Figure 2.14: Selected figures from Lai et al.[39]

Chapter 3

Experimental Methods

This chapter is devoted to explaining the key experimental fabrication and characterisation methods and techniques.

3.1 Sputtering

Sputtering is the name of a process by which atoms are removed from the surface of a material by bombarding it with energetic particles. Its main applications are for (non-selective) etching of surfaces, analysis of material composition (Secondary Ion Mass Spectrometry, or SIMS; see section 3.5) and thin film deposition. It was first developed as a thin film physical vapour deposition (PVD) technique in the 1920s and has since become the prominent alternative to evaporation in microelectronic fabrication. The main advantages of sputter deposition over evaporation are better step coverage, better adhesion and the ability to deposit compound materials and alloys. The texts by Campbell[4] and the chapter on ZnO magnetron sputtering by Szyzka in the text by Ellmer et al.[40] and a review[41], also by Ellmer, were the key sources for the following explanation. Campbell[4] and Chapman[42] were referred to for the discussion of sputtered film growth in section 3.1.5.

A typical sputter deposition system can be described, in a basic sense, as a parallel-plate plasma reactor as shown in figure 3.1. The essential function can be described

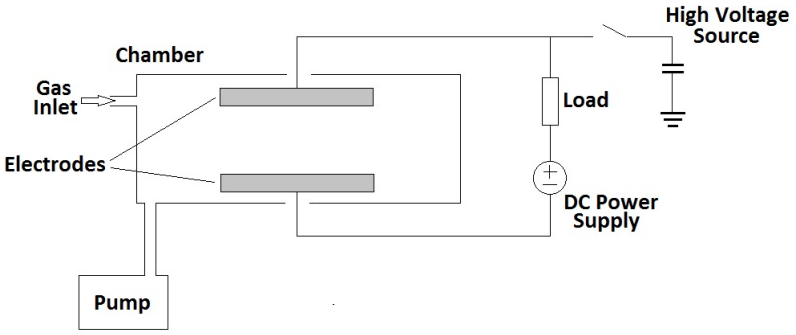

Figure 3.1: A basic DC parallel plate reactor.

as follows: An inert gas is partially ionised to create a self-sustaining plasma, or glow discharge, in a vacuum chamber. The material to be deposited (the *targets(s)*) and the substrates are placed on electrodes of opposing polarity within the chamber. The plasma ions are accelerated towards the target electrode, where the material to be deposited is placed. The target material is bombarded with these ions, and through momentum exchange in the surface layers, target atoms are removed. Due to the low pressure in the chamber, some of these atoms are able to travel across the short gap towards the substrate electrode, where they accumulate on the surface of the substrate.

3.1.1 Plasma Formation

Argon is most commonly used as the inert feed gas in sputter deposition. Partial pressure of reactive gases such as oxygen are sometimes added in order to affect the stoichiometry of the deposited film. The chamber is initially evacuated to pressures below $\sim 10^{-6}$ Torr, before the Ar is fed in at flow rates that are typically tens of SCCM (Standard Cubic Centimetres per Minute), resulting in a working pressure of a few mTorr. The Ar gas will typically contain a small concentration of ions and electrons to begin with. A potential difference is applied between the electrodes, causing the ions to be accelerated towards the negatively charged cathode (the target) and the electrons accelerate (more rapidly, due to their smaller mass) towards the positively charged anode. When the ions reach the cathode and collide with the surface of the

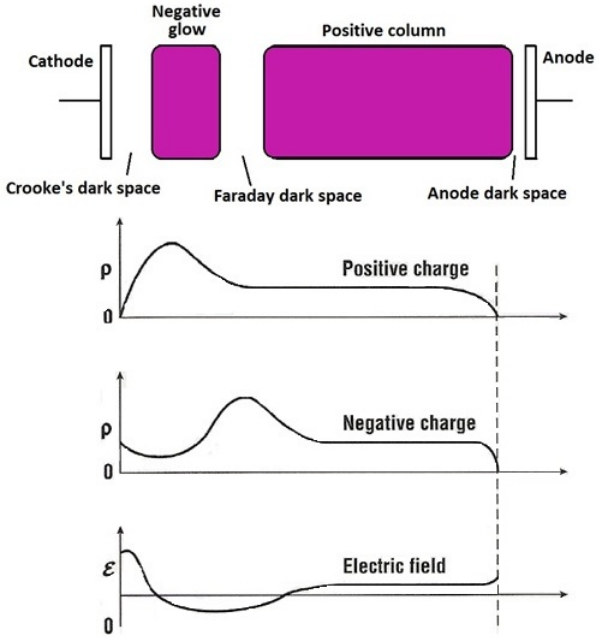

Figure 3.2: Optical emission, positive and negative charge densities (due to ion and electron densities respectively) and the electric field as a function of distance between the anode and cathode. Figure adapted from Campbell[4].

target, a number of processes occur - one of which is the release of secondary electrons from the target as the ions' kinetic energy is transferred. The secondary electrons, in turn, are accelerated towards the anode, gaining energy. When collisions occur between high energy secondary electrons and neutral Ar atoms, further ions are created, thus creating and sustaining a plasma as long as the voltage across the electrodes is sufficient to give the electrons enough energy for ionisation.

Figure 3.2 shows the essential electrical and optical properties in the region between the electrodes. The indicated regions of optical emission, or glow, are a result of a high concentration of electrons with 'moderate' energy - enough to excite atomic electrons in a neutral atom to higher energy states by inelastic scattering, but not enough for ionisation. The atomic electrons quickly return to their ground states through emission of photons - hence the glow. Electrons are rapidly accelerated from the cathode, resulting in a low electron density (compared to the ion density) and a net positive charge in the region close to it as seen in figure 3.2. In this region, named the *Crooke's dark space*, electrons do not have enough energy to cause optical emission. Further from the cathode, electrons have gained enough energy to create ions, increasing their concentra-

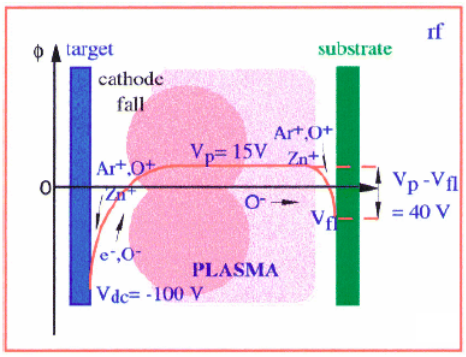

Figure 3.3: Potential (ϕ) distribution in a RF magnetron discharge . Acceleration of ions and electrons are indicated as well as some typical values for the target potential, V_{dc}, the potential within the plasma, V_p and the potential drop between the plasma and the substrate, $V_p - V_{fl}$. The darker shaded regions indicate high concentration of electrons in a torus-like plasma region due to the magnetic field for the case of magnetron sputtering (see section 3.1.3). Figure adapted from Ellmer[41].

tion with distance from the cathode. The positive charge region shields the bulk of the plasma from the cathode, with the result that the ionisation rate is suppressed across the rest of the distance. The Crooke's dark space is the most important region from the point of view of sputtering. The large electric field here causes ions that have drifted or diffused into this region to accelerate rapidly towards the cathode, bombarding the target material situated there. This *ion bombardment* of the cathode is the essential condition for sputtering and defines the process.

When the material on one or more of the electrodes is insulating, the ejection of secondary electrons results in the build up of charge in the surface layers, eventually extinguishing the plasma. Therefore, for insulating electrode materials, an ac signal is used to drive the plasma, at radio frequency. At radio frequency, only the electrons, (not the ions due to their larger inertia), are able to follow the oscillation. Electrons are rapidly accelerated by the oscillating potential, striking alternate electrode surfaces resulting in a net negative charge at both surfaces with respect to the plasma. The resulting electrical potential is shown in figure 3.3. Thus a RF discharge is driven mainly by the oscillation of the electrons in the plasma, as opposed to secondary electrons released from the surface of the cathode in the case of DC sputtering. An asymmetrical

potential, maximising the voltage drop between the upper electrode (target) and the plasma, is achieved by adjusting the relative areas of the electrodes, often by connecting the substrate electrode to the walls of the chamber[4].

3.1.2 Ion Bombardment

Ion bombardment is illustrated in figure 3.4 showing the processes that can occur, depending on the energy possessed by the incident ion. Ions with very low energies (10s of eV), can be reflected from the surface, often being neutralised by transfer of an electron from a surface atom, as shown in the part labelled *1* in figure 3.4. Secondary electrons are also removed from the surface as mentioned above. At energies below $\sim$ 10 eV, the ion can also adsorb to the surface, giving up its energy to lattice vibrations. At very high energies ($\gtrsim$ 10 keV), the ion can penetrate many atomic layers deep below the surface, damaging the lattice. This is the *ion implantation* regime, labelled *2* in figure 3.4. In this regime, theoretical models that approximate the atoms and ions as hard spheres are, to a first approximation, appropriate for describing observations, whereas chemical effects are more important in explaining low energy impacts. Sputtering occurs with ion energies between these two extremes ($\sim$ 30 to 1,000 eV[40]), with the result that physical and chemical effects are important, making theoretical treatment very complicated. A sputtering event, by which one or more atoms are removed from the target material with velocity component perpendicular to the surface, also requires multiple collisions within the surface, as in part *3* of figure 3.4. *Nuclear stopping* is effective in the sputtering energy range, such that the majority of energy transfer occurs within a few atomic layers below the surface. Sputtered atoms and atom clusters typically leave the target surface with energies of around 10 to 50 eV - two orders of magnitude greater than that of evaporated atoms - which gives them surface mobility once they reach the substrate, leading to better step coverage and adherence and reduced stress in the resulting matrix[4, 40].

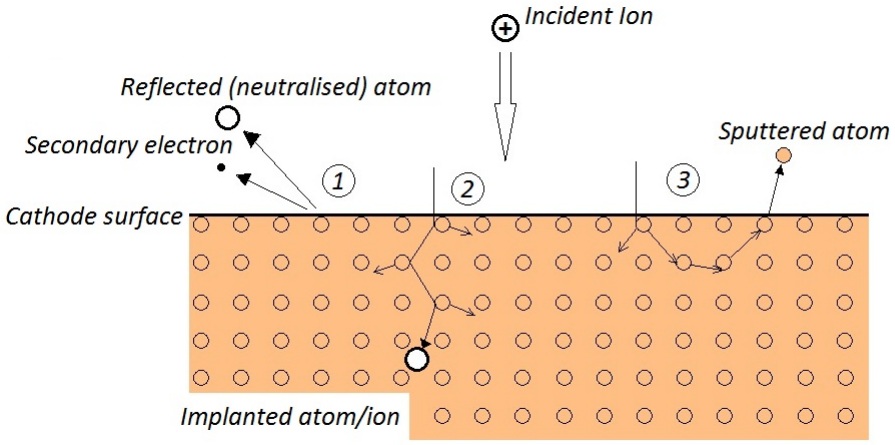

Figure 3.4: The bombardment of the target surface by energetic ions and the three, numbered processes that happen as a result, depending on the ion's energy.

3.1.3 Magnetron Sputtering

The relative concentration of ions in a simple parallel plate (DC or RF) reactor constitutes only a small fraction of the gas. Increasing the concentration of ions is essential to improve the rate of ion bombardment and therefore the sputtering rate. Plasmas that are enriched in this way are generally referred to as *high density plasmas* (HDP). These involve the use of the Lorentz force,

$$F = q\overline{v} \times \overline{B} \tag{3.1}$$

due to the presence of a magnetic field, to bend the path of the electrons in the discharge chamber in a direction perpendicular to both their velocity and the magnetic field. This induces circular motion of charged species with acceleration perpendicular to their motion and the field, with the radius expressed by equating equation 3.1 with the equation for the centripetal force:

$$r = \frac{mv}{qB} \tag{3.2}$$

Due to the large mass of the ions, their path will only be slightly deflected, whilst electrons will follow a helical path, greatly increasing their path length. This results in much greater probability of collisions with neutral atoms and therefore an increased

rate of ionisation. The most common HDP method employed in sputtering is a *magnetron* configuration, in which the electrons being accelerated away from the cathode are trapped within the cathode dark space. A torus-like high density plasma region is formed in this region, eroding the target in a non-uniform manner[41]. This also allows plasma formation at lower chamber pressures (down to $\sim 10^{-7}$ Torr).

3.1.4 Sputter Yield and Deposition Rate

Many factors and parameters affect the rate of deposition in a sputtering system, which can be loosely divided into three steps: the flux of ions impinging on the target, the probability of ejection of an atom as a result and transport of sputtered species across the plasma to the substrate. The second, the probability of ejection is characterised by a parameter called the *sputter yield*, S, which is defined as the number of ejected target atoms, Z_e per incident ion, Z_i[40]:

$$S = \frac{Z_e}{Z_i} \tag{3.3}$$

The comprehensive, and still most accepted theory for the sputtering yield from ion bombardment was given by Sigmund in 1969[43]. The work by Ellmer on ZnO magnetron sputtering[41] uses a semi-empirical approach to the deposition rate, which is quite instructive since it is expressed in terms of sputtering parameters. The sputter yield depends linearly on the ion energy, E_{ion} above a threshold energy, E_{thres}, such that it can be expressed as:

$$S = \text{const.}\,(E_{ion} - E_{thres}) = \text{const.}e\,(V_p - V_{dc} - V_{thres}) \tag{3.4}$$

where V_p and V_{dc} are defined in figure 3.3, $V_p - V_{dc} = V_{ion}$ and $e.V_{ion} = E_{ion}$. The threshold energy, $E_{thres} = e.V_{thres}$, depends on the ratio of the atomic masses of the ions and target atoms and the surface binding energy[41]. The sputtering rate, R, is proportional to the sputtering yield and a term involving the discharge current, I, and γ, the *secondary electron emission coefficient*:

$$R = \text{const.}SI\,(1 - \gamma) \tag{3.5}$$

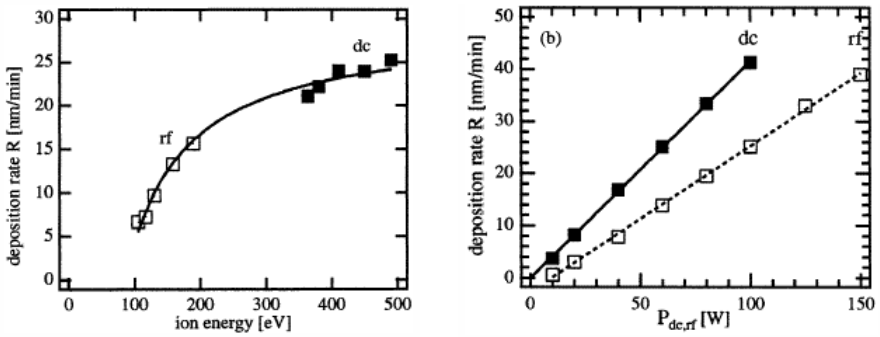

(a) Deposition rate for ZnO by RF and DC magnetron sputtering. The curve is a fit of equation 3.6 to the experimental data.

(b) Experimental data exhibiting the linear dependence of the sputtering rate, R, on the discharge power, P for DC and RF magnetron sputtering.

Figure 3.5: Experimental ZnO magnetron sputtering rate dependence on *a)* E_{ion} and *b)* P. Figures taken from Ellmer[41].

By combining equations 3.4 and 3.5 and re-expressing in terms of the discharge power, $P = IV_{dc}$:

$$R = \text{const.} eP\,(1-\gamma)\left(1 + \frac{V_p - V_{thres}}{V_{dc}}\right) \tag{3.6}$$

So the deposition rate is linearly dependant on the discharge power, a parameter that is easily adjusted in most sputtering setups[41]. This is valid for ion energies up to ~ 750 eV, above which the ion implantation regime begins to dominate[4].

3.1.5 Thin Film Formation

The majority of the sputtered material arriving at the substrate does so in atomic or molecular form. The atom's mobility on the surface is determined by its kinetic energy, the binding energy between the sputtered and substrate species and the nature and temperature of the substrate. These factors have significant influence on the morphology of the resulting film and the geometry and orientation (texture) of crystallites[44, 42]. In terms of potential energy, the surface of the substrate consists of a series of depressions of varying magnitude, known as *adsorption sites*. The more mobile the atom (or *adatom*) is on the surface, the higher its chance of finding an energetically favourable adsorption site for crystal growth, minimising the residual stress in the resulting film. Minimising

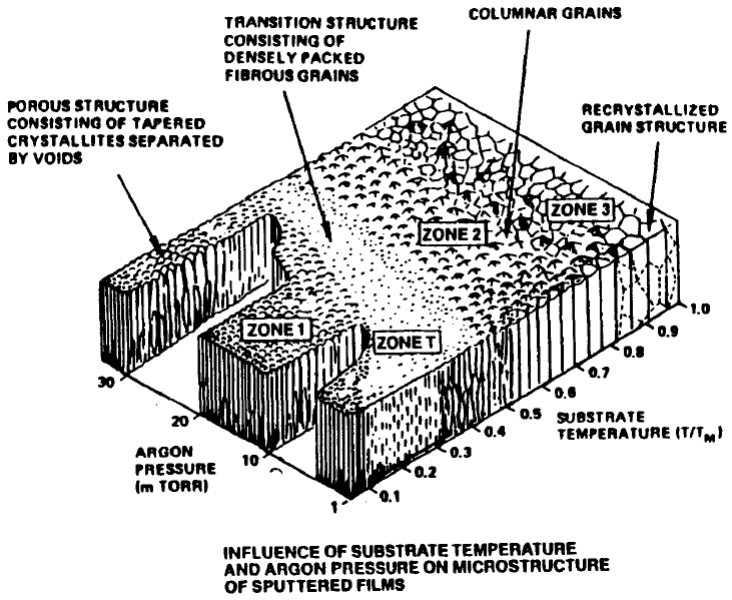

Figure 3.6: The three-zone model of thin film deposition. Figure taken from Thornton[45].

stress is desirable since it is well known that doing so improves the mechanical stability and electrical properties of the deposited thin film[41]. Surface mobility is enhanced by increased substrate temperature, and the situation is also improved if the atom is given enough time to have a good chance of finding a good position, hence low deposition rate. The thin film formation process is then generally described by three main stages: first *nucleation*, where single adatoms join with other adatoms during diffusion on the surface, leading to the formation of islands; second, *island growth*, where the islands grow in size until they meet other islands and begin the final process of *agglomeration* or *coalescence*. A smooth, continuous film results, assuming sufficient surface mobility.

The relationship between the morphology of the film and the key sputtering parameters of Ar gas pressure and substrate temperature is described by a zone model, illustrated in figure 3.6. The model was initially proposed by Movchan and Demchishin[46] and subsequently modified by Thornton[45]. The model is broadly applicable to materials that crystallise[4]. In *Zone 1*, with the lowest temperature and moderate pressure, the film is amorphous due to low adatom surface mobility. Lowering the pressure (thereby increasing the energy of sputtered atoms) and/or increasing the substrate

temperature pushes the growth into *Zone T*, with very small grains forming. Further increasing the temperature or decreasing the pressure results in increased grain sizes. In *Zone 2* these grains are columnar, orientated orthogonal to the surface plane. In *Zone 3*, large, 3D grains are formed.

3.2 X-Ray Diffraction

X-Ray diffraction (XRD) is a useful, non-destructive characterisation technique that can reveal several important properties of powders and thin films. This simple discussion of the working principle of the technique and its application to thin film analysis is mostly based on Kittel[2] and Birkholz[47].

X-rays are suitable for use as probes into crystal structure because they have a wavelength that is smaller than or comparable to the lattice constant. When X-ray photons are incident on a crystal structure, they interact with the material in three different ways. One is *photo-ionisation*, in which their energy and momentum is given to electrons, liberating them from their bound atomic energy states. Similarly, in *Compton scattering*, the energy and momentum is given to an electron, but it remains bound to the atom. These are both inelastic scattering events, where energy and momentum are lost by the incoming photon. The interaction that is important for XRD is called *Thompson scattering*, an elastic scattering process, whereby the electron oscillates at the frequency of the incoming x-ray beam. The energy, and therefore wavelength, of the incoming x-ray beam is unchanged in this process, and Thompson scattered beams are the ones used in XRD analysis. The x-rays also equivalently interact with the atomic nuclei, but the intensity of the scattered beam has an inverse-square relationship to the mass of the interacting object. Since the mass of atomic nuclei is three orders of magnitude larger than that of an electron, events involving interaction with atomic nuclei can be neglected in favour of scattering from their bound electrons, located, to first approximation, at lattice sites.

Depending on the material, each lattice plane might reflect $\sim 10^{-3}$ to 10^{-5} of the

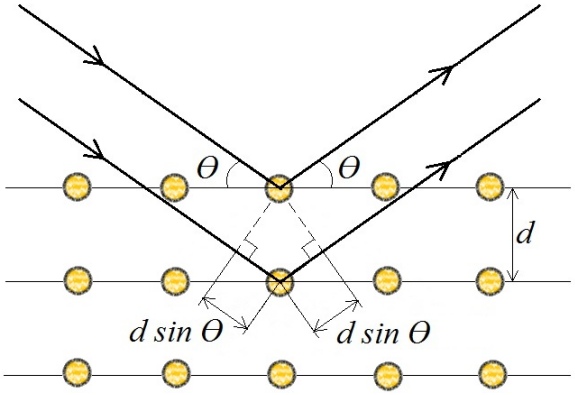

Figure 3.7: A simple diagram illustrating the origin for the Bragg equation. The fine, horizontal lines represent lattice planes in two dimensions, with the second dimension into the paper, and d is the spacing between the planes. The bold lines are the paths of two x-ray beams in the plane of the paper, being scattered elastically by the first and second lattice planes, their paths making angles θ with the planes. The path difference between the two beams after scattering is indicated.

incident radiation, so that hundreds of thousands of atomic layers may contribute to the reflected beam. Depending on the path difference between reflected beams, they interfere constructively or destructively with each other. For constructive interference to occur, and a reflection to be observed, the path difference between contributing beams must be an integral multiple of the wavelength of the beams (which are monochromatic by design). A simple picture of the geometry of this requirement is presented in figure 3.7, resulting in the *Bragg* law - the condition for constructive interference:

$$2d \sin \theta_B = n\lambda \tag{3.7}$$

where λ is the x-ray wavelength, n is an integer, θ_B is the *Bragg angle*, angles of incidence at which constructive interference occurs and d is the lattice spacing. As a result of the periodicity of the lattice, for a monochromatic x-ray beam with a given wavelength, a detector finds peaks in reflected x-ray intensity for Bragg angles of incidence that depend on the lattice spacing which is characteristic for a particular plane direction in a crystal phase of a particular material. These peaks are termed *Bragg reflections* and carry useful information about the structure of the measured sample.

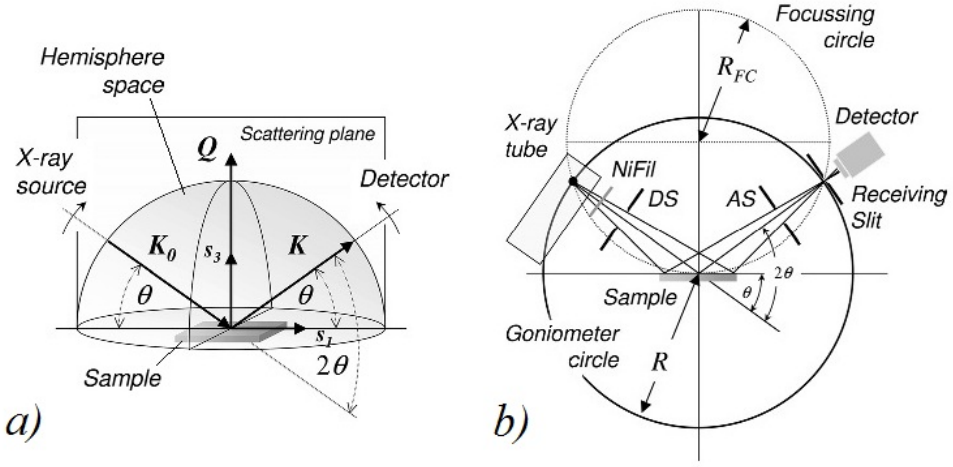

Figure 3.8: *a)* Locked coupled geometry from the reference frame of the measured sample. $\overrightarrow{Q} = \overrightarrow{K} - \overrightarrow{K}_0$ is the *scattering vector*, the difference between the wave vectors of the scattered and incoming beams. It is analogous to the *momentum transfer vector* in particle collisions. *b)* Schematic representation of $\theta/2\theta$ diffraction in Bragg-Brentano geometry. (Figure adapted from Birkholz[47]).

3.2.1 Locked Coupled Scan

The most common XRD experimental arrangement, making use of this phenomenon is the *locked coupled* scan, or $\theta/2\theta$ scan. A schematic representation of the key geometry involved in the scan is presented in figure 3.8. Usually, x-ray source is fixed in place, whilst the sample holder is rotated on its axis with angle θ and the detector rotated with angle 2θ about a circular path labelled the *Goniometer circle* in the figure, with the sample at the origin. Hence a constant distance, R, is maintained between the sample and the detector, which is essential as the intensity of the reflected beam would otherwise depend on this parameter.

The geometry from the reference frame of the measured sample is illustrated in figure 3.8 *a)*. The scattering vector, Q, defined in the figure, is always normal to the surface of the sample in a locked coupled scan, which has the result that in a polycrystalline sample, only crystallites with lattice planes orientated parallel to the surface contribute to a Bragg reflection. This situation is illustrated for the case of a polycrystalline thin-film sample in figure 3.9.

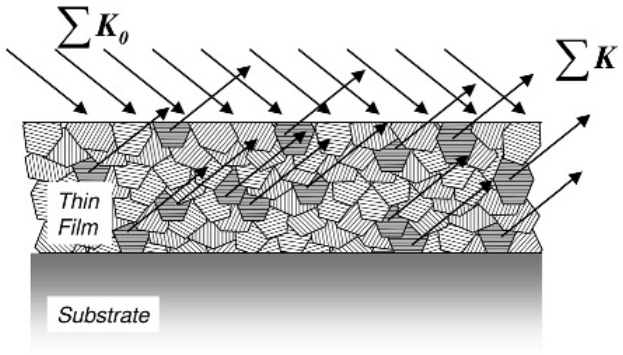

Figure 3.9: Illustration of selective reflection from crystallites with lattice planes parallel to the surface of the sample. (Figure adapted from Birkholz[47]).

The XRD locked coupled scan on thin-film, polycrystalline samples is a source of information in several areas of material characterisation. Firstly, crystalline phases of materials present in the film can be identified from the characteristic position of their Bragg reflection peaks. Further information can then be gleaned by analysing the peak itself.

For example, the measured position of the peak can give the lattice spacing in the direction perpendicular to the surface via the Bragg law, equation 3.7. This, referred to that measured for a powder sample of the material, is a measure of the macroscopic residual strain in the film. This is often a function of the method and parameters in fabrication or deposition of the measured film, and is also often influenced by the presence of intrinsic and extrinsic defects and impurities in the lattice. Cebulla et al.[48] used the following expression to calculate the absolute stress of a film with a hexagonal lattice in the c-direction:

$$\sigma_{film} = \frac{2c_{13}^2 - c_{33}\left(c_{11} + c_{12}\right)}{2c_{13}} \left(\frac{c_{film} - c_{bulk}}{c_{bulk}} \right) \tag{3.8}$$

where c_{11}, c_{12}, c_{13} and c_{33} are elastic constants and the final term in parentheses is equal to the strain in the c-axis direction, ϵ. c_{film} is the c lattice parameter of the sample film and c_{bulk} is the reference lattice parameter. In this project, the lattice parameter from powdered ZnO, from Heller et al.[7] will be used as the reference. Cebulla et al. used the elastic constants for single crystal ZnO, obtained from Landolt and Börnstein[49]

to determine:

$$\sigma_{film} = -233.\epsilon \tag{3.9}$$

in units of [GPa].

The full width of the Bragg reflection at half-maximum intensity (or FWHM) can be used to estimate the size of the crystallites contributing to the reflection. The Scherrer equation, originally provided by Scherrer[50] and derived and adapted in Birkholz[47], relates the peak FWHM to the crystallite size:

$$D_{cube} = \left(2\sqrt{\ln 2/\pi}\right) \frac{\lambda}{\beta_{2\theta} \cos\theta_B} \tag{3.10}$$

which, by evaluating the terms in parentheses, approximates to:

$$D_{cube} \approx 0.94 \frac{\lambda}{\beta_{2\theta} \cos\theta_B} \tag{3.11}$$

where the subscript on D_{cube} refers to the fact that this form of the equation is appropriate for crystallites of approximately cubic shape. The term in parentheses in equation 3.10 converts the equation from the case where the integral breadth of the peak is used in place of the FWHM. $\beta_{2\theta}$ is the contribution to the FWHM of the peak due to the crystallite size. The magnitude of the FWHM is also increased by instrumental broadening, which we will label $\beta_{2\theta_i}$. The instrumental broadening effect can be determined by performing a scan on the (002) peak for single crystal ZnO, since broadening is almost entirely due to the instrument in this case. $\beta_{2\theta}$ should then be calculated by:

$$\beta_{2\theta} = \sqrt{\beta^2_{2\theta_m} - \beta^2_{2\theta_i}} \tag{3.12}$$

where $\beta_{2\theta_m}$ is the measured FWHM of the (002) reflection. For the setup used here, instrumental broadening has been determined to be 0.008°.

In addition, a measure of the texturisation of the film can be determined using a locked coupled scan. *Texture* or the anisotropy of the crystalline orientation, is the degree to which the crystallites in a film are preferentially orientated. A sample with no texture is one in which the crystallites are randomly oriented. Texturing often occurs in thin films, again depending on deposition method and parameters. If a sample

is textured, then one particular Bragg reflection will demonstrate enhanced intensity and other reflections will suffer reduced intensity relative to reflections from randomly oriented grains. This is due to the existence of a larger proportion of grains that are oriented in the preferred direction, resulting in a proportionally greater number of Bragg reflections at the characteristic angle of that particular lattice plane.

The integral intensity, I_h, of a Bragg reflection signal received by the detector in a locked coupled scan depends on many factors and therefore cannot be taken at face value. The following expression is explicitly derived in Birkholz[47] and given here:

$$I_h = I_0 \frac{r_e^2}{\dot{\theta}} \lambda^3 m_h T_h \left(\frac{1 + \cos^2 \theta}{\sin \theta \sin 2\theta} \right) \frac{|F_h|^2}{V_{uc}^2} V \frac{A_{\theta 2\theta}(t)}{2\mu} \tag{3.13}$$

where I_0 is the intensity of the initial x-ray beam, r_e is the classical radius of an electron, $\dot{\theta}$ is the scan velocity, V is the sample volume and μ is the *linear attenuation coefficient*. m_h is the *multiplicity factor*, which takes into account the number of equivalent lattice planes that could all cause a reflection at a given Bragg angle. F_h is a structure factor, which contains information on the electron distribution for the unit cell of the sample and its square is here divided by the square of V_{uc}, which is the volume of a unit cell, giving a term that has the form of an electron density. The terms in equation 3.13 mentioned thus far are all approximately constant for a given sample material. T_h is the *texture factor*, which is equal to unity for a random sample and greater than one for Bragg intensities relating to preferred orientations. It is the influence of this factor that we would like to see when comparing peak intensities. However, there is also an *absorption factor*, $A_{\theta 2\theta}$, which is dependant on the thickness of the sample (as derived by Birkholz[47]):

$$A_{\theta 2\theta} = 1 - \exp\left(-\frac{2\mu t}{\sin \theta} \right) \tag{3.14}$$

where t is the sample thickness. To remove dependence on thickness, thus producing peaks with intensity that, to a good approximation, is only dependant on the relative degree of texturisation, the measured intensity should be divided by $A_{\theta 2\theta}$.

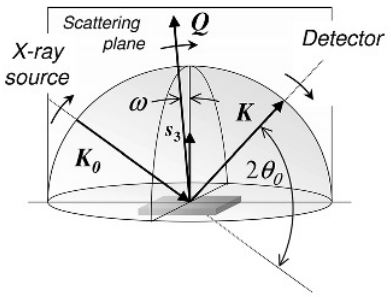

Figure 3.10: An illustration of the geometry of a rocking curve scan. Figure adapted from Birkholz[47].

3.2.2 Rocking Curve

Rocking curves can be used to indicate relative degrees of orientation, as investigated and described by Blanton[51], for example. The following basic description is based on Birkholz[47] and the relevant geometry is illustrated in figure 3.10.

A locked coupled scan generally precedes a rocking curve scan, in order to accurately determine the Bragg angle of the reflection corresponding to the preferred orientation direction. Though the approximate Bragg angle may be known or may have been previously calculated, slight changes in characteristic Bragg angles may be observed due to sample factors such as lattice strain and slight displacement errors in loading the sample[51]. Once the Bragg angle is determined, the detector is fixed at that angle, which is denoted as $2\theta_0$ in figure 3.10, whilst the sample is tilted ('rocked') about the Bragg angle θ_0. The tilt angle, generally renamed by convention to ω, can be measured either from the plane of the sample surface or from its normal. In the case illustrated, it is measured from the normal. The rocking curve is so named for the nature of the motion of the sample, but is also often referred to as either a θ scan (by analogy to the $\theta 2\theta$ scan) or more often an ω scan. The result is a *texture profile*; a plot of detected intensity $I_{rc}(\omega)$ at a fixed scattering angle $2\theta_0$. The intensity drops symmetrically, either side of the peak centre, as a result of the decreasing density of appropriately orientated crystallites for Bragg diffraction as ω is increased. The profile is dependent on other factors such as defocusing and different absorption coefficients, and thus must

be corrected for the latter when comparing samples with different thickness. However, comparison of the FWHM of different samples provides a relative measure of the degree of orientation of the crystallites in a thin film sample.

3.3 Hall Effect Measurements

The *Hall effect* can reveal several useful electrical properties of materials. It is possible to determine the resistivity, $\rho = 1/\sigma$, and the mobility, μ and concentration, n, of charge carriers in semiconductors. By varying the temperature, the concentration and activation energies of donors and acceptors can also be determined. This method of electrical characterisation is particularly useful when applied to materials such as ZnO, since rectifying contacts are not required, only Ohmic contacts, which are easier to form. One disadvantage is that the nature and geometry of the method means that the measured quantities are averaged over the whole sample, such that spacial variations are hidden[52].

3.3.1 The Hall Effect

The derivation of the basic relations pertaining to the Hall effect is based on the approach in Kittel[2], Streetman[14] and Young & Freedman[53]. The derivation describes the mechanism of the effect first observed by E. H. Hall in 1879[54].

We can describe the effect by considering a flat, rectangular sample of a conductive material. Figure 3.11 shows the forces acting on the mobile charge carriers in the sample, in the case where the charge carriers are electrons. Here an electric field, E_x is applied in the $+x$ direction, resulting in a current with density J_x and an electron drift velocity v_d in the opposite direction. A magnetic field, $\overrightarrow{B} = B_y\widehat{j}$ is applied in the $+y$-direction, perpendicular to the current and the plane of the strip. The resulting magnetic force on the charge carriers is in the $+z$-direction, driving the moving charges to the upper edge of the strip with the Lorentz force: $F_z\hat{k} =\mid q \mid v_d\overrightarrow{B}$. In the case where electrons are the charge carriers, this causes a build-up of excess negative charge

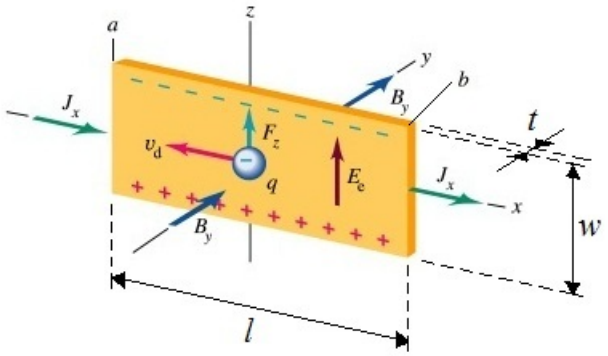

Figure 3.11: Forces on charge carriers in a conductor in a magnetic field. Figure adapted from Young & Freedman[53].

at the upper surface, and thus leaving an excess positive charge on the bottom surface. This charge distribution leads to an electrostatic field, $\overrightarrow{E_e} = E_z\hat{k}$, which builds up until an equilibrium is reached, where the resulting electrostatic force is just large enough to balance the magnetic force. The net force in the z-direction is zero:

$$\overrightarrow{F} = q\left(\overrightarrow{E} + v \times \overrightarrow{B}\right) = 0 \tag{3.15}$$

$$\therefore F_z\hat{k} = e\left(E_z\hat{k} + v_d B_y\hat{j}\right) = 0 \tag{3.16}$$

with e being the *electronic charge*, which is positive by definition. The current now flows in the x-direction, with the carriers following a straight path. It is the establishment of the electric field, E_z, that is known as the Hall effect and the resulting potential difference is called the *Hall voltage*, $V_H = E_z w$, where w is the width of the sample (in the z-direction). The current density is given by:

$$J_x\hat{i} = nq\overrightarrow{v_d} \tag{3.17}$$

assuming a common drift velocity for all of the charge carriers (this assumption holds for degenerate semiconductors). By substitution into equation 3.16,

$$-\frac{1}{ne} = \frac{E_z\hat{k}}{J_x\hat{i}B_y\hat{j}} = R_H \tag{3.18}$$

where R_H is known as the *Hall coefficient*[1], which is negative when electrons are charge carriers, since e is positive, and vice-versa. E_z, J_x and B_y are all known or measured in a Hall measurement and thus, the carrier concentration and type can be deduced from the value and the sign of R_H.

The Hall effect can also be used to determine the resistivity of the sample (the inverse of conductivity), which is measured in Ohms centimetres (Ω cm), via resistance measurements and the dimensions of the sample. In the case of the bar configuration shown in figure 3.11:

$$\rho = \frac{V_{ab}}{I_x}\frac{wt}{l} \tag{3.19}$$

where V_{ab} is the potential difference between points a and b in figure 3.11, I_x is the current in the x-direction and w, t and l are the sample dimensions as labelled in the figure. The mobility, μ, is defined as the drift velocity attained by the charge carrier in response to an external electric field. It can also be expressed in terms of the conductivity and hence the resistivity via equation 2.10, such that $\sigma = qn\mu$ and

$$\mu = \frac{\sigma}{qn} = \frac{R_H}{\rho} \tag{3.20}$$

so that the mobility is simply the ratio between the Hall coefficient and the resistivity.

The geometry in the case of thin films is slightly different, though the principle is the same. In this project, the samples used for Hall measurements measured were ~ 1 cm squares. The soldered contacts were formed at the corners of the sample and the size of these contacts affects the measurement. Thus, a correction factor had to be applied to the measured results[55]:

$$\epsilon = \frac{\delta l}{L} \tag{3.21}$$

where δl is the lateral extent of the contact (triangular contacts are assumed) and L is the length of the sides of the sample. For the carrier concentration:

$$n = \frac{n_m}{1+\epsilon} \tag{3.22}$$

[1]Not to be confused with the *Hall resistance*, which is often given by the same symbol.

where n_m is the measured carrier concentration. For the mobility:

$$\mu = \mu_m (1 + \epsilon) \tag{3.23}$$

In the case of the resistivity, the correction scales with ϵ^2 and is therefore negligible, since the contact diameters were ~ 1 mm.

3.3.2 Temperature Dependent Hall Measurements

To get the most out of Hall measurements, they should be performed over a wide a range of temperatures as possible. The activation energy, E_a, and concentration of electrically active donor and/or acceptor impurities can be found by fitting simulations to measured curves for carrier concentration and mobility variation with temperature.

For a non-degenerate semiconductor, we have the expression for the charge neutrality condition[52]:

$$n + n_d = N_d - N_a^- \tag{3.24}$$

where n is the electron concentration in the CB, N_d and N_a are the concentrations of donor and acceptor atoms respectively and n_d is the concentration of occupied donor electron states. n and n_d are given by:

$$n = N_C \exp\left(-\frac{E_C - E_F}{kT}\right) \tag{3.25}$$

and

$$n_d = N_d \left[\frac{1}{1 + \beta \exp\left(\frac{E_d - E_F}{kT}\right)}\right] \tag{3.26}$$

where E_d is the donor state energy, β is a factor relating to the degree of degeneracy of the donor level and N_C is the effective density of states in the CB. Combining equations 3.24 to 3.26, one can find the expression[56]:

$$\frac{n\left(n + N_a^-\right)}{N_d - N_a^- - n} = \beta N_C \exp\left(-\frac{E_C - E_d}{kT}\right) \tag{3.27}$$

where $E_C - E_d = E_a$. Solving for n gives the following quadratic equation:

$$n^2 + n\left(N_a^- - N_C^{'}\right) - \left(N_d - N_a^-\right) N_C^{'} = 0 \tag{3.28}$$

where

$$N_C' = \beta N_C \exp\left(-\frac{E_C - E_d}{kT}\right) \tag{3.29}$$

The curve fitting performed here (see section 4.4.6.2) assumes one species of donor, partially compensated by one fully ionised species of acceptor. Equations 3.27 and 3.28 both describe the variation of n with temperature. By fitting with TDH measurements of n vs. temperature, the value of $N_d - N_a^-$ and E_a can be determined. Curve fitting of the mobility measurements results would then be required, which gives an expression involving the term $N_d + N_a^-$, in order to extract the values of N_d and N_a.

3.4 Transmittance Measurement

A Shimadzu Solidspec 3700 spectrophotometer was used to measure transmittance through the ZnO films on glass substrates. The system is able to measure light intensity that is directly or diffusely transmitted or the total transmitted light intensity. The latter configuration utilises an *integrating sphere* as shown in figure 3.12, reflecting all diffuse, scattered transmitted light onto a central detector which also detects directly transmitted light. The sphere has two openings and the initial beam is split between these two openings. A *baseline* measurement is performed, with no sample in place, as in figure 3.12*a)*. This is done so that the software can cancel out possible differences in the intensities of the reference and sample beam. The sample is then placed over one of the openings, as shown in figure 3.12*b)* and a measurement is performed.

Transmittance measurements were performed for two purposes. The first was simply to produce optical transmittance spectra for the combined sample and substrate, since one of the potential applications of the ZnO films is as a transparent electrode and this is a representative configuration.

The second purpose of the measurements was to estimate the optical band gap of the sample film. Neglecting interference effects and multiple reflections, the transmitted light intensity through a homogeneous layer follows the Beer-Lambert law with[57]:

$$T(E) = (1 - R)^2 e^{-\alpha(E)d} \tag{3.30}$$

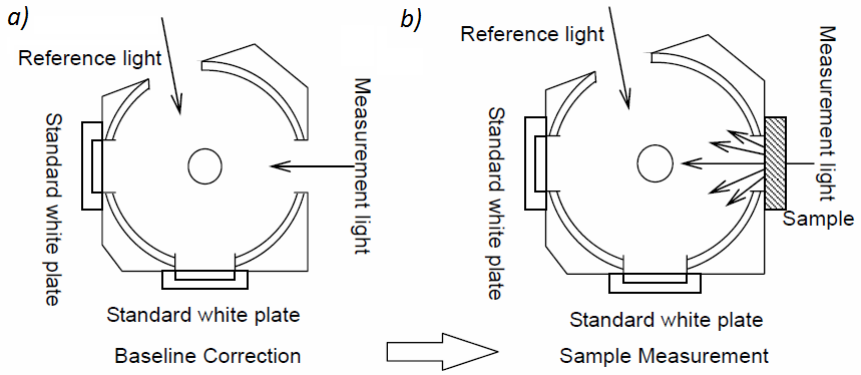

Figure 3.12: Baseline correction and sample analysis using an integrating sphere for measurement of total transmitted light. Figure taken from the Shimadzu 'Training Course for Analysis of Solid Samples' document, for UV/VIS spectrophotometers.

where E is the incident photon energy, R is the reflectivity at the air/layer interface, d is the film thickness and $\alpha(E)$ is the *absorption coefficient* for the semiconductor.

The glass substrate and semiconductor film sample are considered as two layers that each obey the Beer-Lambert law. The transmittance through the plain glass slide, T_{glass}, and the transmittance through the complete substrate/sample structure, T_{sample}, are separately measured. T_{sample} is then normalised to T_{glass} in order to extract an estimate of the absorption coefficient of the semiconductor sample layer via the following expression:

$$\alpha(E) = -\frac{1}{d}\ln\left(\frac{T_{Sample+Glass}}{T_{Glass}}\right) \tag{3.31}$$

where reflection effects have been neglected. The absorption coefficient for a direct band gap semiconductor such as ZnO has the following dependence on the photon energy:

$$\alpha \propto (E - E_g)^{1/2} \tag{3.32}$$

Thus by plotting $\alpha(E)^2$ vs. photon energy E and extrapolating a linear fit to the high absorption region to the x-axis, E_g is estimated.

3.5 Secondary Ion Mass Spectrometry

Secondary ion mass spectrometry (SIMS) is a highly sensitive method of chemical concentration analysis. The following description borrows from Ohring[58], Brandon[59] and Campbell[4].

Mass spectrometry has long been used in chemistry for analysis of gases. The need to measure depth profiles of dopants in semiconductors was one of the main drivers behind the development of SIMS[58], requiring concentration sensitivities down to 100 or even 10 ppb (parts per billion)[59].

SIMS uses sputtering (see section 3.1.2) of the test sample by a beam of Ar^+, O_2^- or Cs^+ ions. Mostly neutral atoms, but also positive and negative ions, are removed from the surface of the sample, entering the gas phase, with low kinetic energies. The charged ions are accelerated towards an electrostatic energy analyser, which bends their path with a radius, r_e, that depends on their kinetic energy, $\frac{1}{2}mv^2$, according to the Lorentz force in an electrostatic field, E:

$$r_e = \frac{mv^2}{qE} \tag{3.33}$$

and a slit then limits the energy range of ions that are passed. The remaining ions then pass through a *magnetic sector* mass filter, which is highly sensitive to the momentum of the ions, according to the Lorentz force in a magnetic field, B:

$$r_m = \frac{mv}{qB} \tag{3.34}$$

The desired charge to mass ratio is thus selected, given by:

$$\frac{q}{m} = \frac{r_e}{r_m^2}\frac{E}{B^2} \tag{3.35}$$

with very high mass resolution.

By scanning the B field, a mass spectrum is produced, giving detection counts per second over a range of ion masses. Analysis can be performed in *static* mode, where the sputter rate is low, giving analysis of the composition of the surface. *Dynamic*

mode requires a higher sputter erosion rate and gives a depth profile. The raw data of detection counts versus sputter time must then be transformed into concentration versus depth. This is far from straightforward, since the detection intensity depends on the erosion rate, the sputter yield (see section 3.1.4) and the probability of ionisation. Thus, calibration must always be performed against a known sample. This is usually provided by ion implantation of the impurity of interest into a pure sample of the matrix. The distribution of the impurity with depth is then well known. Performing a depth profile on this reference sample before and/or after testing the sample of interest allows one to calibrate counts to concentration. The sputter time can be converted to depth by measuring the depth of the SIMS crater after the measurement is complete, assuming a linear relationship. This calibration approach is satisfactory for trace impurities up to concentrations of a few percent. Higher concentrations will affect the ion sputtering yield and the ionisation yield in particular.

3.6 4-Point Probe

The 4-point probe is a simple method for determining the resistivity of semiconductor materials. Within certain boundary conditions on the dimensions of the sample, little preparation is required, making it a good alternative to the Hall effect method in many cases. The following outline of the operating principle of the 4-point probe is based on Valdes[60] and Smits[61].

The measurement mechanism is illustrated in figure 3.13. The four probes are lowered into contact with the surface of the material to be measured. Direct current is passed through the outer two electrodes and the resulting floating potential is measured across the inner two probes. The measured voltage depends on the dimensions of the sample and where on the sample the measurement is performed, relative to boundaries. In this project, samples are rectangular, thin samples, where the thickness of the sample, t, is much smaller (a few hundred nm or less) than the spacing between the probe tips, $s_1 = s_2 = s_3 = s = 1$ mm. In this case, the current emanating from the outer probes

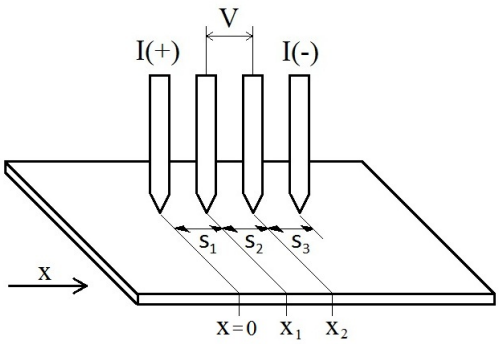

Figure 3.13: A simplified illustration of the 4-point probe measurement method, showing the four in-line probes in contact with a thin rectangular sample. Current, I is supplied by the outermost electrodes, whilst the resulting potential difference is measured across the inner two electrodes.

is taken to have a circular form (as opposed to a spherical form, when $t \gg s$). The differential form of the resistance is given by:

$$\triangle R = \rho \left(\frac{dx}{A} \right) \tag{3.36}$$

where $\rho$is the bulk resistivity, A is the area of the circular protrusion of current and x is the direction indicated in figure 3.13. Integrating between the inner probes, with $A = 2\pi xt$ and given that the total current is $2I$, due to the superposition of the currents, I, provided at each of the outer electrodes:

$$R = \frac{V}{2I} = \int_{x_1}^{x_2} \rho \frac{dx}{2\pi xt} = \int_{s}^{2s} \frac{\rho}{2\pi t} \frac{dx}{x} = \left[\frac{\rho}{2\pi t} \ln x \right]_{s}^{2s} = \frac{\rho}{2\pi t} \ln 2 \tag{3.37}$$

where the integration limits are as indicated in figure 3.13. Rearranging gives the expression for the resistivity of a thin sheet:

$$\rho = \frac{\pi t}{\ln 2} \left(\frac{V}{I} \right) \tag{3.38}$$

which is expressed in units of Ω cm.

Chapter 4

Experimental Details and Results

4.1 Experimental Approach

Previous work (see section 2.5) has shown that the electrical and optical properties of sputtered ZnO films are strongly dependant on the quality of the crystal structure. Therefore, the chosen approach was to initially determine the sputtering conditions for depositing high quality films of pure ZnO. The quality of the films was to be judged via the key factors of the transmittance of light through the film, the texturisation present in the structure, the film stress and the size of the crystalline grains present. The important sputtering parameters were the power delivered to the targets (thus the energy of the bombarding ions and deposited atoms), the temperature of the substrate, the plasma gas flow rate and the addition of any reactive gas - oxygen in this case. Once the optimum deposition parameters had been determined, co-sputtering depositions were performed, varying the power to the Si target, in order to produce samples with a range of levels of Si doping.

Sputtering A Semicore Tri-Axis, balanced field magnetron sputtering system was used, equipped with 3 indirectly cooled 3 inch diameter cathodes provided by Angstrom Science, one DC and two RF. The target cathodes were positioned above the substrate holder, facing it at a small angle from parallel, in order to

allow simultaneous deposition from more than one target. The distance between the target surface and the substrates was ~ 10 cm.

XRD The system used for XRD measurements was a Bruker D8 Discover system with a Cu x-ray source, with wavelengths $k_{\alpha 1} = 1.5406$ Å and $k_{\alpha 2} = 1.54439$ Å and a Goebel mirror was used to separate out the $k_{\alpha 2}$ signal, leaving only $k_{\alpha 1}$.

Optical A Shimadzu Solidspec 3700 DUV spectrophotometer was used for optical transmittance measurements, with light sources allowing use of UV, visible and near-infrared (NIR) wavelength ranges. The wavelength range available using the integrating sphere was 175 - 3300 nm.

Electrical A Lakeshore 7704A Hall measurement system was used to measure the electrical properties of the samples deposited on glass substrates. Temperature control between 10 and 360 K was possible for TDH measurements.

4.2 Samples

The substrates used for the sputtered films were glass and (100) p-type, boron-doped silicon, since the potential applications might require deposition directly onto either material. Each deposition coated four substrates - two glass and two silicon. The glass substrates were microscope slide, cut to size - one measuring 1 cm by 1 cm, for Van Der Pauw Hall measurements, and the other being several times larger, for the purposes of transmittance measurements. The silicon substrates were cut from wafers and measured approximately 1.5 cm by 1.5 cm - large enough for XRD measurements.

4.2.1 Preparation for Sputtering

The glass substrates were cleaned after cutting to remove dust and grease particles. This was done by wiping with acetone followed by 5 minutes submerged in acetone with ultrasonic agitation. The samples were then submerged in ethanol and agitated, before being rinsed in deionised water and dried using compressed nitrogen gas spray.

The RCA wafer cleaning procedure was used for the silicon substrates. This procedure consists of three steps: The first uses a heated (∼80°C) organic solution consisting of a 1:1:5 volume ratio of ammonium hydroxide (NH_4OH) and hydrogen peroxide (H_2O_2) in deionised (DI) water. The wafer is submerged for 15 minutes, to remove dust and grease particles. It is then rinsed in flowing DI water to remove traces of the organic solution. It is then necessary to remove the oxide layer that builds up on silicon on exposure to air and also results from the first step. Oxide stripping is performed by immersion in a dilute (1:50) solution of hydrofluoric acid (HF) in DI water, for a few seconds. A brief DI water rinse is performed again before the final solution, heated hydrogen peroxide and hydrochloric acid (HCL) in DI water (1:1:5), is used to remove the heavy ion impurities that build up as a result of the previous step. Like the first step, this is heated to 80°C and the wafer is submerged for 15 minutes. A final 5 minute DI water rinse is performed and the substrates are dried by spraying with pressurised nitrogen.

4.2.2 Preparation for Hall Measurements

Samples for Hall measurements were deposited on glass slides cut to dimensions of 1 cm by 1 cm. The terminals of the Hall setup substrate holder were soldered to each corner of the sample, using indium, directly onto the ZnO-coated surface, forming Ohmic contacts. These contacts were approximately 1 - 2 mm in diameter.

4.3 Sputtering Pure ZnO

The first step was to optimise the sputter deposition of pure ZnO films on glass and silicon substrates. A 3 inch diameter, 99.99 % purity ZnO target from Semiconductor Wafer Inc. was fitted to one of the RF cathodes.

4.3.1 Predictions and Approach

Initially the effects of the power supplied to the ZnO target and the heating applied to the substrate during deposition were investigated. Increasing the temperature of the substrate is anticipated to increase surface mobility. Increasing the target power should also add to the surface mobility since the sputtered atoms arrive at the surface with more kinetic energy. Increasing the power also increases the deposition rate however, allowing the atoms/molecules less time to relax into an energetically favourable site. Thus, a balance between these two parameters was expected to be found.

The effects of adjusting Ar gas flow rate were investigated next. This directly affects the pressure in the chamber during deposition, and therefore the deposition rate. The higher the Ar gas flow rate, the lower the deposition rate, due to an increase in sputtered atom and ion collisions. A higher flow rate might therefore improve the morphology and reduce stress in the resulting film.

Oxygen in the feed gas has been shown in previous work to have sensitive and somewhat complicated effects on the structure and electrical properties of sputtered ZnO thin films. In general its use has mostly been confined to reactive sputtering for oxidation when sputtering from a metallic Zn target. It has been shown however, in work on Al-doped ZnO sputtering, that introducing O_2 during deposition can decrease the residual stress in the lattice, although the c-axis orientation is reduced[62]. If the films deposited in pure Ar are deficient in oxygen, resulting in the presence of a metallic Zn phase, it is hoped that the introduction of O_2 might reduce the concentration of this phase, perhaps improving the transmittance.

4.3.2 Treatment of Errors

From the ZnO (002) reflection in XRD locked coupled scans, the crystallite size, D, c lattice parameter and film stress, σ, were calculated. This involved analysis of the peaks using the Origin (version 8.1, OriginLab, Northampton, MA) and Eva (version 13, Bruker-AXS) software packages, producing FWHM and centre position measurements.

To evaluate the errors involved in the measurement and calculation of the relevant

parameters, a locked coupled scan was performed twice on the same sample, unloading it from the sample holder and reloading it between measurements. The FWHM and peak position were determined by the same method in the Eva software package and each was carried through the calculations of D, c and σ to obtain two results for each and estimate an error range, δ_m.

To estimate the impact of the chosen software analysis method, the FWHM and peak positions were determined on four different samples using several different analysis methods available in the two software packages. The maximum and minimum values for D, c and σ determined by the various methods were used as an estimated error range due to the analysis technique, δ_a.

The error ranges were then added in quadrature, to give a total estimated error range, i.e. $\delta_r = \sqrt{\delta_m^2 + \delta_a^2}$ for each parameter. In the case of the stress calculation, the lattice parameter for a powder sample is included. In the work by Özgür et al.[63], four c lattice parameter measurements by XRD and energy dispersive x-ray diffraction (EDXD) are given and the range of these results was used in the stress calculation. The calculated error ranges are given in the results tables that follow and are indicated in figures where the above parameters are plotted.

4.3.3 Target Power and Substrate Temperature

Three different ZnO target powers: 50, 150 and 250 Watts, were used in combination with substrate heating at four different temperatures during deposition: 150, 300, 450 and 600°C . The chamber was initially vacuum pumped to a pressure below 2×10^{-6} Torr. The Ar gas feed was then maintained at 50 SCCM, giving a working pressure in the chamber of 11 - 12.5 mTorr.

Locked coupled and rocking curve XRD scans were performed on all samples in order to evaluate their crystal quality. Figure 4.1 shows a full $\theta/2\theta$ scan from 20 - 100 degrees for the sample deposited on glass using a target power of 50 Watts and with the substrate heated to 450°C during the deposition. The prominence of the ZnO (002) peak is clear, demonstrating a strong preferred crystallite orientation in the c-

Substrate	Sample	Target Power (W)	Temperature (°C)	D (±2) (nm)	c (±0.001) (Å)	Film Stress (±0.14) (GPa)
Glass	*a*	50	450	26	5.239	-1.42
	b	50	600	24	5.244	-1.62
	c	150	450	14	5.248	-1.83
	d	150	600	15	5.244	-1.62
Si	*a*	50	300	28	5.225	-0.79
	b	50	450	36	5.225	-0.79
	c	50	600	24	5.205	0.06
	d	150	450	11	5.259	-2.32
	e	250	450	11	5.251	-2.00

Table 4.1: Summarised XRD results for ZnO samples deposited with varying ZnO target powers.

axis direction (perpendicular to the sample surface). Figure 4.2a compares the (002) reflections for several of the glass-based samples. A selection of the samples was chosen for presentation here on the basis of having measurable (002) peaks. The samples were sputtered using a fixed deposition time, so the thicknesses vary between samples with different target power settings. In light of this, the plots in figure 4.2a are normalised to their absorption factors, $A_{\theta 2\theta}$ in order to remove dependence of the peak intensity on the thickness of the sample, as discussed in section 3.2.1. The structural properties of these samples are summarised in table 4.1. The grain size, D, was calculated from the FWHM using equation 3.11 and the c lattice parameter was calculated from the position of the peak on the x-axis using equation 3.7. The samples with the largest grain sizes were chosen for figure 4.2 to aid clarity. Figure 4.2a indicates that the optimum sputtering parameters in terms of target power and substrate temperature on the glass substrate are 50 Watts and 450°C respectively. A similar result was obtained in the case of samples deposited on Si substrates. Again, a selection of the normalised (002) reflections are presented in figure 4.2b. Though the stress was subtly reduced in the case of the 600°C heated sample on the Si substrate (as indicated by the slight shift to the right of the peak position), the 50 Watts, 450°C sample's reflection indicated larger grain size (smaller FWHM) and a higher degree of texturisation.

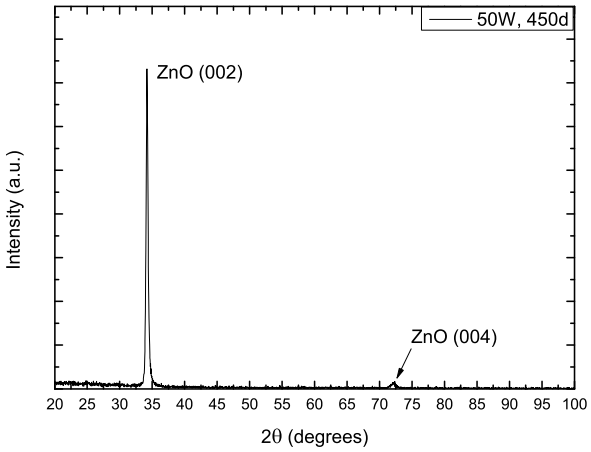

Figure 4.1: ZnO (002) and (004) Bragg reflections obtained in a locked coupled XRD scan. This sample was deposited on glass with a target power of 50 Watts and substrate heating at 450°C.

The transmittance through the samples on glass substrates was then tested. Figure 4.3 shows the optical transmittance results for ZnO films of approximately 100 nm sputtered on glass substrates with target power of 50 Watts and various substrate heating temperatures. Equivalent plots for target powers of 150 W and 250 W are given in appendix A.1 and show similar results. Apart from the deposition with 600°C substrate temperature, the transmittance for the visible region is $> 75\%$, and is $> 80\%$ between $450 < \lambda < 650$ nm. At low wavelengths, below the UV absorption edge, there is a small peak, and the transmittance does not go to zero. This will be commented on in section 4.3.4.

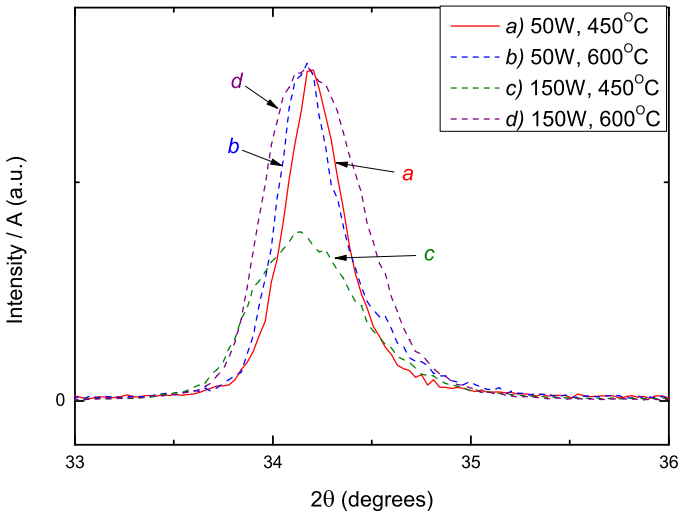

(a) A comparison of the ZnO (002) reflections for a selection of the samples deposited on glass substrates. The peak intensities have been normalised by the absorption factor, $A_{\theta 2\theta}$ in order to remove the dependence on the film thickness.

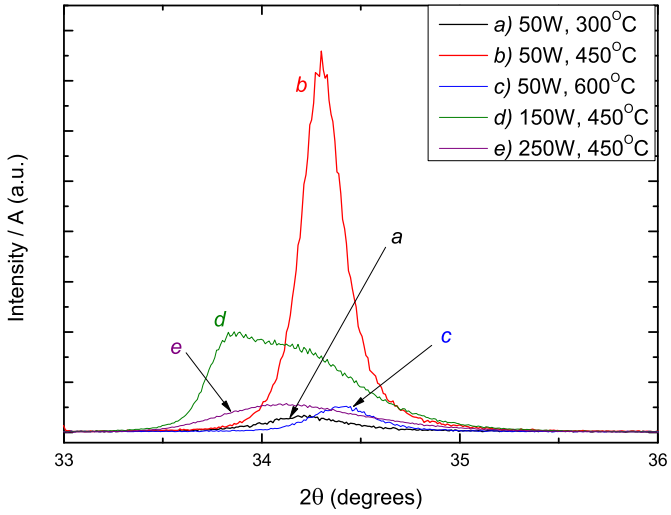

(b) A comparison of the normalised (002) reflections for a selection of the samples deposited on Si substrates.

Figure 4.2: XRD $\theta/2\theta$ scans with varying sputtering power and substrate temperature on glass substrates. In both figures, the intensity shown on the y-axis has a linear scale and arbitrary units. The peaks are indexed with letters corresponding to target powers and substrate temperatures in the legend.

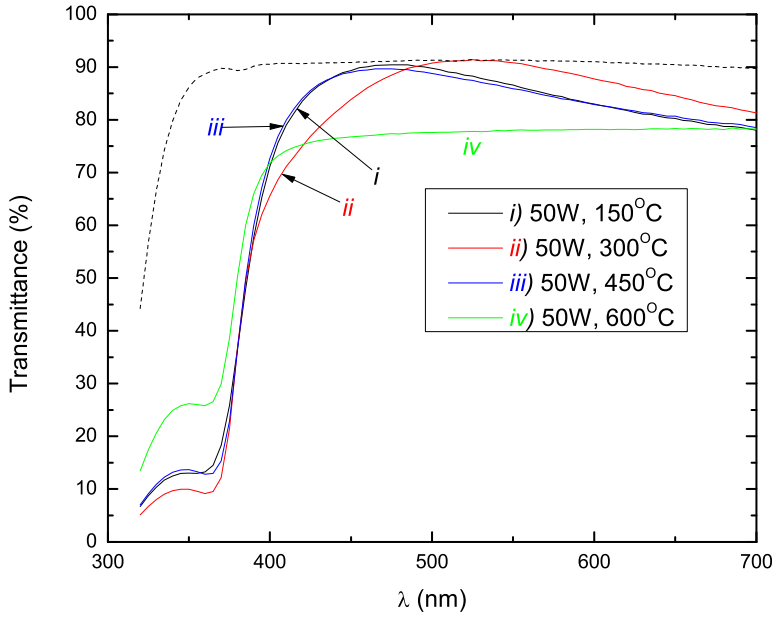

Figure 4.3: Optical transmittance spectra for ZnO films sputtered on glass substrates for 1 hour with target power of 50 Watts. The dashed line is the transmittance spectrum for a plain glass slide, for reference.

4.3.4 Argon Gas Flow

The optimum target power and substrate heating conditions at a constant Ar flow of 50 SCCM were determined in the previous section to be 50 Watts and 450°C respectively. The next step was to determine the optimum Ar flow rate, keeping all other parameters constant. Since the Ar flow rate affects the deposition rate in a predictable manner, the deposition time was varied in order to keep a roughly constant thickness of 100 nm for each sample. This was achieved using deposition rate vs. Ar flow rate data from previous work on the particular sputtering setup used here and the same ZnO target. The flow rates used and their resulting working pressures are summarised in table 4.2 along with the XRD results.

The XRD results are also illustrated using (002) peak comparisons from $\theta/2\theta$ scans in figure 4.4. The most immediately obvious aspect of the two comparison plots is the shift in the position of the (002) reflection for the lowest pressure deposition. This indicates an increase in the c lattice constant, and is expected, since the lowest pressure results in the highest deposition rate. As stated in section 2.2.1, the c-lattice constant for pure ZnO is $c = 5.2069\,(\pm 0.0001)$ Å, so values above this suggest increased mechanical stress in the lattice - an undesirable property, mechanically and electrically, as discussed in section 3.1.5. Taking into account the resulting stress, grain size and degree of texturisation, the 70 and 85 SCCM flow rates give the best properties. Since the

Substrate	Ar flow rate (SCCM)	Chamber Pressure (mTorr)	D (± 2) (nm)	c (± 0.001) (Å)	Film Stress (± 0.14) (GPa)
Glass	15	3.8	21	5.265	-2.59
	50	12.1	21	5.222	-0.66
	70	16.3	28	5.225	-0.82
	85	19.4	25	5.221	-0.66
Si	15	3.8	31	5.272	-2.93
	50	12.1	36	5.220	-0.59
	70	16.3	50	5.213	-0.26
	85	19.4	51	5.213	-0.26

Table 4.2: Summary of XRD results and the chamber pressure during deposition resulting from the chosen Ar flow rates.

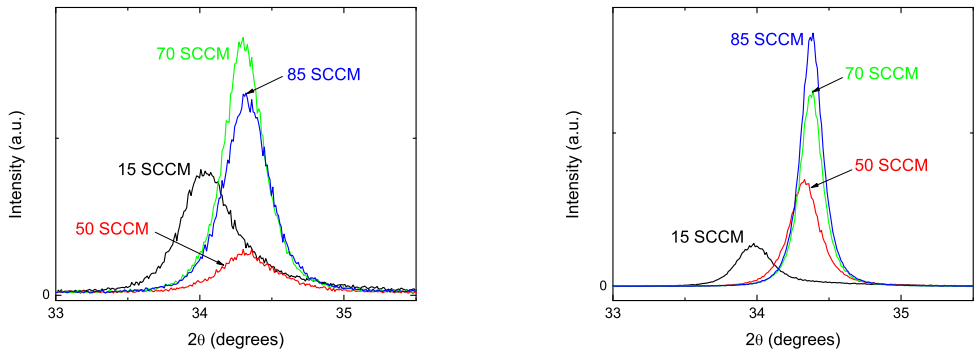

(a) ZnO (002) reflections for varying Ar flow rates during depositions on glass substrates.

(b) ZnO (002) reflections for varying Ar flow rates during depositions on Si substrates.

Figure 4.4: XRD $\theta/2\theta$ scans of the ZnO (002) reflection for varying Ar flow rates.

deposition rate for the 85 SCCM case is so low (~ 50 nm/hour), the 70 SCCM flow rate was chosen in order to obtain the desirable film properties whilst maintaining a practical deposition time (~ 75 nm/hour) going forward.

The transmittance spectrum is given in figure 4.5. The transmittance in the visible region is similar for all samples - consistently $> 70\%$ and $> 75\%$ for the majority of the visible region, (at $450 < \lambda < 700$ nm). The low wavelength peak mentioned in the previous section is also apparent in figure 4.5. A sample was deposited with flow rate of 85 SCCM for five hours in order to obtain a thickness of ~ 200 nm. The transmittance through this sample is also plotted in figure 4.5 and in this case, the transmittance drops to zero at wavelengths smaller than 375 nm. Thus, it is suggested that the low wavelength peak exhibited by the thinner samples is due to effects at the interface between the sputtered layer and the substrate, and is not seen in the case of the thicker sample since the light does not reach the interface.

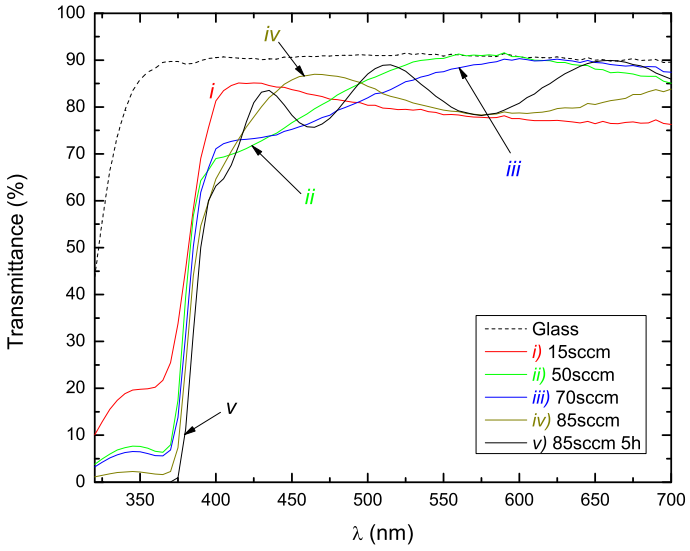

Figure 4.5: Optical transmittance spectra for ZnO films sputtered on glass substrates using various Ar flow rates. Sample *v)* was deposited with gas flow rate of 85 SCCM for 5 hours, as indicated.

4.3.5 Sputtering with Oxygen

Oxygen was introduced into the argon gas feed during deposition. The flow rates of the two gases could be independently controlled, and the total was always maintained at 70 SCCM. Small partial pressures of O_2 were desirable, but the gas feed was unstable or did not operate below a threshold minimum flow rate of around 2 SCCM - a limitation of the flow control. Thus, the minimum flow rate of O_2 required for stability, maintaining a total flow rate of 70 SCCM, was 3 %. Four depositions were made, varying the O_2 flow rate, and compared to a reference sample, *R*, sputtered in pure Ar with the optimum parameters determined in sections 4.3.3 and 4.3.4. The resulting films were analysed using XRD locked coupled and rocking curve scans, and transmittance measurements. The XRD (002) peaks and rocking curves are shown in figure 4.6, the key XRD results are summarised in table 4.3 and the transmittance spectra are plotted in figure 4.7.

No consistent positive effects of the introduction of O_2 were observed in the XRD

analysis. Generally speaking, it did appear to reduce the residual stress in the lattice, with the c-lattice parameter very closely approaching that of the powder ZnO sample, quoted in section 2.2.1, particularly on the Si substrate, as seen in table 4.3. However, it is difficult to discern a trend with increasing O_2 partial pressure. In most cases the O_2 reduced the intensity of the (002) reflections in the locked coupled scans in figures 4.6a and 4.6b, when compared to the reference sample, R. This indicates a reduction in the degree of c-axis orientation, or texturisation. The grain sizes for films deposited on glass substrates were increased by the introduction of O_2 whilst the grain sizes for those deposited on Si substrates were significantly reduced from that of the reference. The insets in figures 4.6a and 4.6b show Gaussian fits to the rocking curves for the same samples, the FWHM of which are noted in table 4.3. The rocking curve FWHM was smallest for the reference sample in both cases.

The transmittance of the films deposited with O_2 is improved over sample R in the visible region close to the UV cutoff. However, this could well be due to small differences in the film thickness or refractive index altering the interference, since the average transmittance across the visible spectrum is similar. Further studies are required to resolve this issue. There is a slight blue-shift in the UV absorption edge with the inclusion of O_2 but it does not vary linearly with increasing partial pressure. The transmittance results do not suggest that O_2 gives any significant advantage over sputtering with pure Ar in this setup.

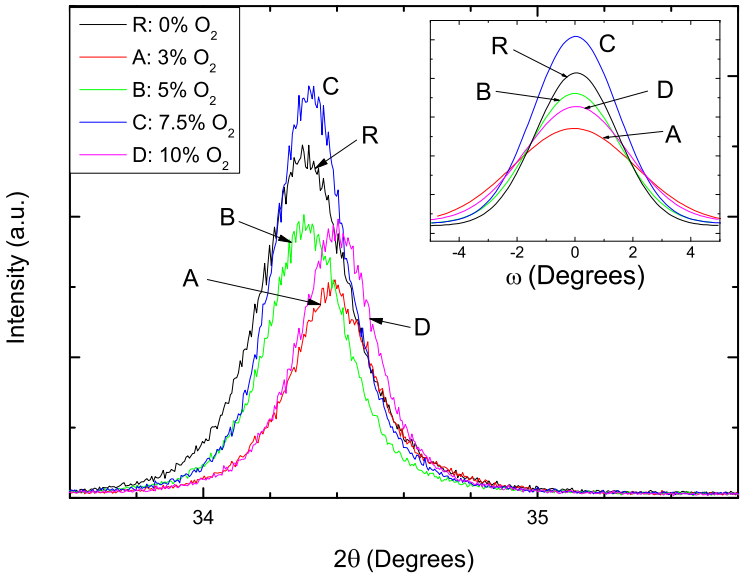

(a) ZnO (002) reflections for depositions with varying partial pressures of O_2 in the Ar feed gas, on glass substrates. The inset shows the rocking curves for the same reflections.

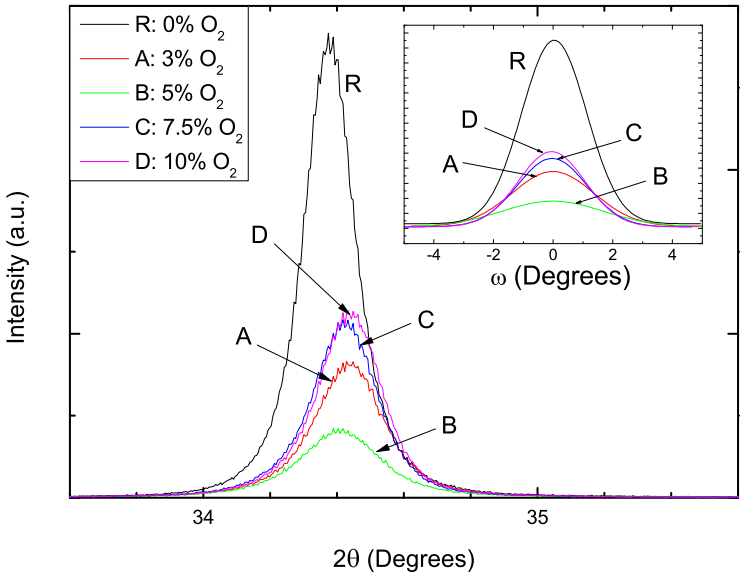

(b) ZnO (002) reflections for depositions with varying partial pressures of O_2 in the Ar gas feed, on Si substrates. The inset shows the rocking curves for the same reflections.

Figure 4.6: XRD results for depositions with varying partial pressures of O_2 in the Ar gas feed. Lattice constants and grain sizes are given in table 4.3.

Substrate	Sample	O_2 Flow rate (%)	D ($\pm$0.2) (nm)	c ($\pm$0.001) (Å)	Film Stress ($\pm$0.14) (GPa)	ω_{FWHM} (degrees)
Glass	R	0	28	5.225	-0.82	3.33
	A	3	31	5.211	-0.17	4.97
	B	5	33	5.224	-0.79	3.65
	C	7.5	34	5.222	-0.69	3.44
	D	10	33	5.209	-0.11	4.21
Si	R	0	48	5.213	-0.26	2.56
	A	3	36	5.205	0.06	3.23
	B	5	31	5.209	-0.11	3.99
	C	7.5	39	5.207	-0.01	2.75
	D	10	39	5.205	0.08	2.63

Table 4.3: Summarised XRD results for ZnO samples deposited with varying partial pressures of O_2.

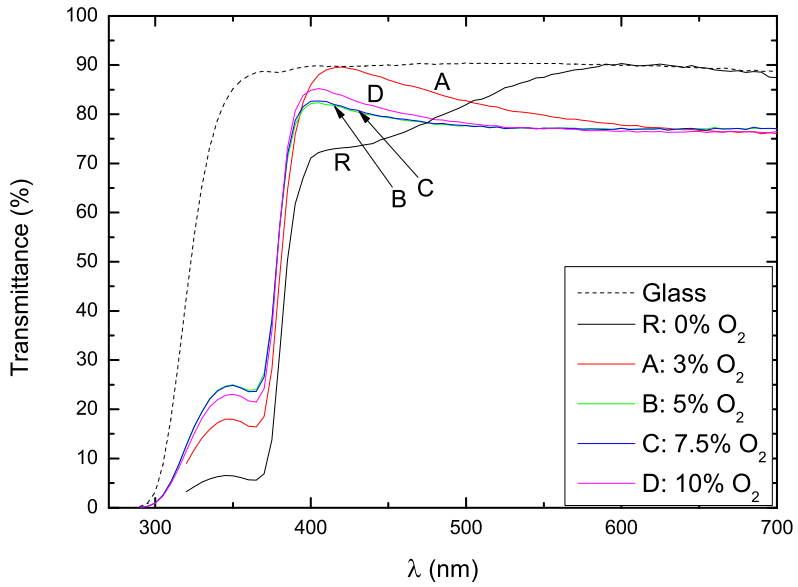

Figure 4.7: Optical transmittance spectra for ZnO films sputtered with varying partial pressures of O_2 in the Ar gas feed.

4.4 Co-sputtering ZnO and Si

4.4.1 Predictions and Approach

From the literature outlined in section 2.5, it was anticipated that a minimum resistivity should be observed with a Si atomic weight percentage of $\sim 1-3\%$. It was thought that this would coincide with optimum structural properties, evidenced by narrow FWHM of the (002) peak in locked coupled XRD scans and a high degree of texturisation. However, the Si content was adjusted through the power applied to the target and the connection between this parameter and the resulting Si content in the film was unknown. The actual content would best be determined by Rutherford back-scattering spectrometry (RBS) analysis, which was not performed here. The work by Lai et al.[39], and specifically table 2.1 was initially used as a rough guide to the Si/ZnO target power ratios, since their co-sputtering approach most closely matched the one used here. The structural, optical and electrical results are compared with the undoped reference sample with the optimum deposition parameters determined in section 4.3. Optimisation of the electrical properties via Si doping, leading to the lowest attainable resistivity value was performed. Subsequently, the effects of increased doping concentration on the lattice and electrical and optical properties were observed.

4.4.2 Determining Si Content

As can be determined from table 2.1, Lai et al. produced six samples with Si target power to ZnO target power ratio, $P_{Si/ZnO} = {}^{P_{Si}}/_{P_{ZnO}}$ between zero and 1.67. In a similar manner, the Si doped samples in this project were sputtered with $P_{Si/ZnO}$ between zero and 2. SIMS depth profiles were performed on the first batch of Si doped samples. The first batch consisted of samples sputtered with $P_{Si/ZnO} = 0.3$, 0.6, 0.8, 1 and 2. Figure 4.8 shows the obtained SIMS profile for the $P_{Si/ZnO} = 0.3$ case. The sample is on the left side of the plot, with the Si substrate on the right. There is a peak at the interface between the sample and substrate in the depth profile. This is a feature that is often seen in depth profiles performed on sputtered samples, and is generally

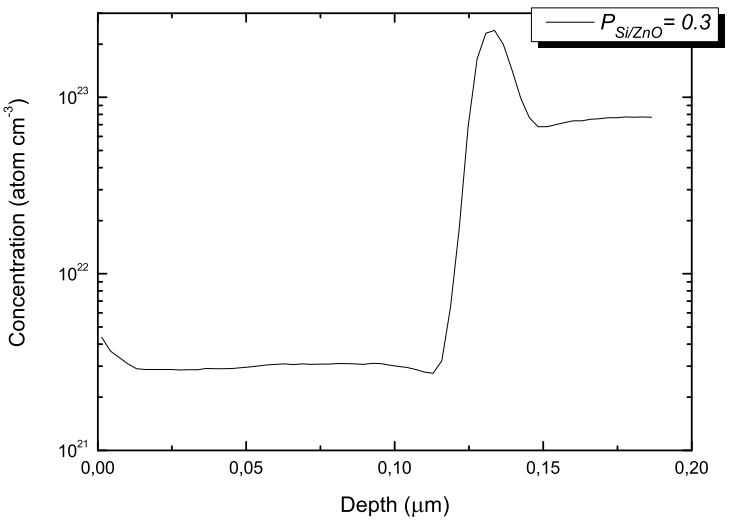

Figure 4.8: SIMS depth profile for Si content in sample sputtered with $P_{Si/ZnO} = 0.3$.

attributed to matrix and mixing effects at the interface, which enhance the ionisation yield of Si. The measured concentration in the sample is $\sim 3 \times 10^{21}$ atoms cm^{-3}. The atomic density of ZnO, calculated using the lattice parameters provided by Heller et al.[7], is $\sim 8 \times 10^{22}$ cm^{-3}, suggesting that the Si content in this sample is $\sim 8\%$. The samples using higher values of $P_{Si/ZnO}$ gave Si concentrations of $\sim 10^{23}$ cm^{-3}, suggesting that the ionisation yield has changed due to significant changes in the matrix with the excessive concentration of Si. Referring to Lai et al., the power ratio of 0.3 was expected to produce a film with Si content of $\sim 0.5\%$, so there is clearly a significant difference in the deposition rate ratio for this setup.

In accordance with this result, a new batch of samples was sputtered, with lower values of $P_{Si/ZnO}$: 0.02, 0.08, 0.14, 0.18, 0.24, 0.34, 0.4, 0.44, 0.5, 0.54 and 0.58. The lower range ($\lesssim 0.4$) were deposited in order to determine a resistivity trend with Si concentration, whilst those with $P_{Si/ZnO} \gtrsim 0.4$ were expected to exhibit much higher resistivity and were to be investigated for the formation of Si NCs.

4.4.3 Structural Properties

The structural properties as determined by locked coupled scans of the ZnO (002) peak are summarised in figure 4.9. For the samples deposited on glass substrates, it is clear that the most desirable structural properties were obtained with $P_{Si/ZnO} = 0.24$. This produced the second largest grain size of ≈36 nm (the largest was produced by the $P_{Si/ZnO} = 0.14$ sample, with $D \approx 37$ nm). This coincided with a minimum absolute stress in the c-axis of ≈ 0.1 GPa, as compared with the undoped case where the stress was ≈ 0.8 GPa. The largest reflection intensity was also obtained with this level of Si doping, indicating the highest degree of texturisation. With this Si content, all three of the key indicators of crystal quality are improved over the equivalent properties of the best undoped ZnO film. In particular, the reduction in stress and increase in grain size suggest introducing the Si during deposition significantly influences the morphology of the film. There is also a strong correlation between these three structural properties as functions of $P_{Si/ZnO}$, with improvements in grain size generally coinciding with improvements in both stress and degree of texturisation. Low Si concentrations appear to initially degrade the crystal quality from the pure ZnO case, and after an optimal doping concentration region is passed, increasing the concentration degrades the crystal lattice again.

Whilst the structure vs. Si doping trend is similar between the two substrate types, there is a significant difference in grain sizes for the undoped sample. The undoped sample deposited on Si has a larger grain size than any of the Si doped samples on either substrate. With Si doping around the optimum region, the grain sizes are quite similar between the two substrates, and the difference is again more pronounced for greater doping concentrations.

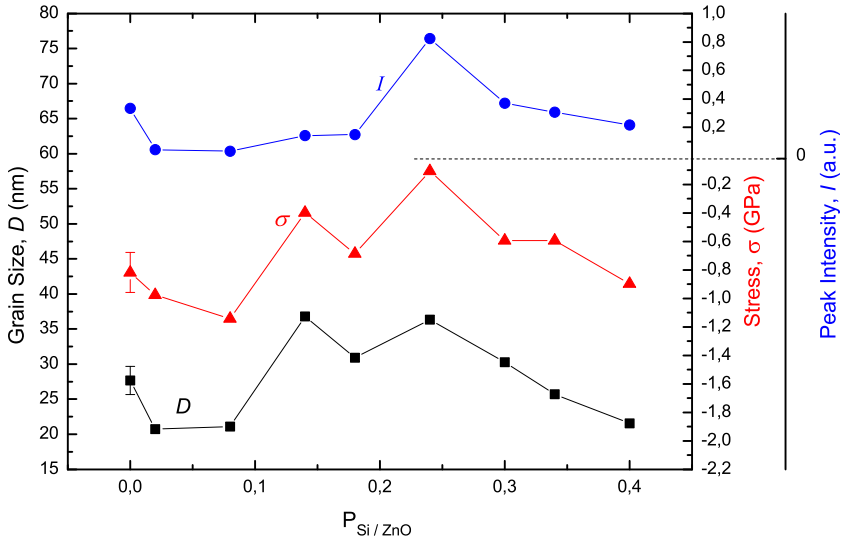

(a) A summary of the XRD properties of the (002) ZnO reflection in Si doped ZnO samples on glass substrates. The y-axes on the right-hand side both share a common origin which is marked with a dashed line.

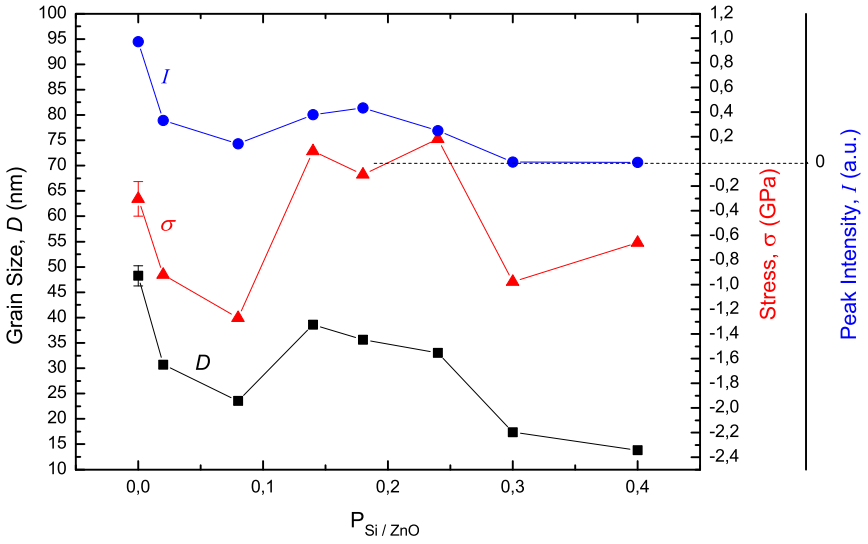

(b) A summary of the XRD properties of the (002) ZnO reflection in Si doped ZnO samples on Si substrates. The y-axes on the right-hand side share a common origin, marked by the dashed line.

Figure 4.9: XRD results for Si doped ZnO samples.

4.4.4 Electrical Properties

The electrical properties of the Si doped and undoped reference samples on glass substrates were determined using Hall measurements at room temperature. There was some difficulty in measuring some of the samples, but the majority with $P_{Si/ZnO}$ between 0.02 and 0.58 were successfully measured. The resistivity trend with Si doping is compared with the grain size trend in figure 4.10a as evidence for the correlation between the structural and electrical properties. Note that the grain size trends for both substrate types are shown, whilst the electrical characterisation was only performed on samples with glass substrates. As was determined in the previous section, the grain size is representative of the key structural crystal quality indicators. The largest grain sizes coincide approximately with the lowest resistivity values. Small values of $P_{Si/ZnO}$, which were shown in section 4.4.3 to degrade the crystal quality, also increased the resistivity significantly (more than an order of magnitude) above that of the undoped film. The ZnO (002) peak vanishes for $P_{Si/ZnO} > 0.4$ and the resistivity increases. This is expected, when taking figure 2.14a into account, though results from Lai et al.[39] and Minami[13] suggested a somewhat more dramatic increase in resistivity with increasing Si content above the optimum level.

A summary of the electrical properties determined using room temperature Hall measurements and the 4-point probe is presented in figure 4.10b. ρ_{Hall} is the resistivity as determined by Hall and ρ_{4p} is the resistivity as determined by 4-point probe measurements. Resistivity, carrier concentration, n, and carrier mobility, μ trends with $P_{Si/ZnO}$ are shown. An initial reduction in the carrier concentration with small levels ($P_{Si/ZnO} = 0.08$) of Si doping was measured. The large difference between ρ_{Hall} and ρ_{4p} (two orders of magnitude) could be taken to indicate a difference in the electrical properties brought on by exposure to light, since the sample is starved of light during a Hall measurement. This is further discussed in section 4.4.6.1. An increase of six orders of magnitude in carrier concentration then coincides with the equally dramatic reduction in resistivity with $P_{Si/ZnO} = 0.18$. A minimum resistivity of 1.3×10^{-3} Ω cm was obtained (as measured by Hall) using $P_{Si/ZnO} = 0.24$, the same power ratio that

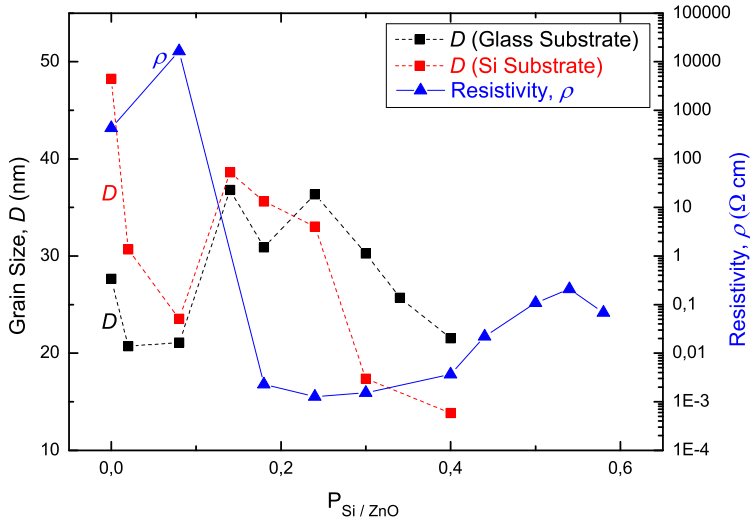

(a) The resistivity as determined by Hall measurements plotted together with the grain size for ZnO films with $P_{Si/ZnO}$ values between 0.02 and 0.58, indicating a correlation between the electrical and structural properties.

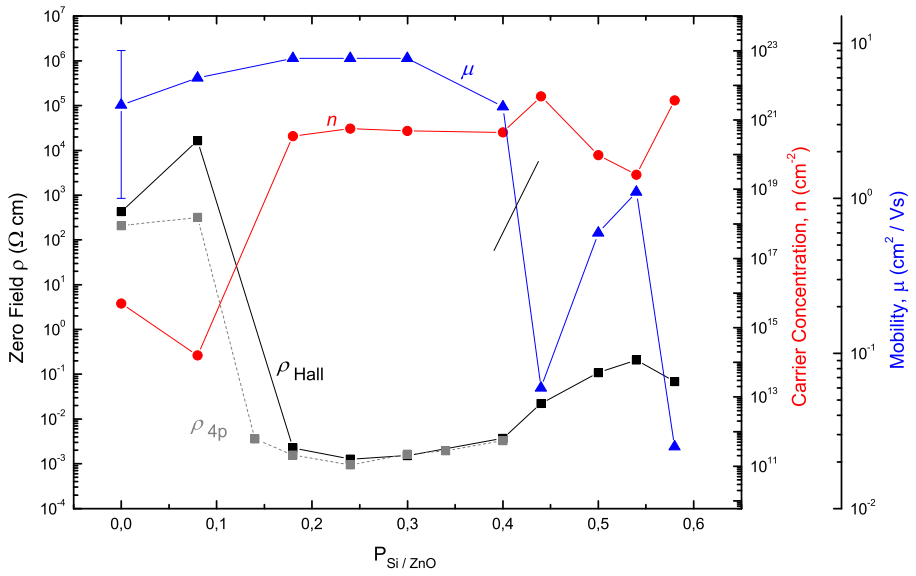

(b) A summary of the electrical results for the Si doped ZnO samples. These measurements were performed at room temperature and the resistivities determined at zero magnetic field. ρ_{Hall} is the zero-field resistivity as determined by room-temperature Hall measurements and ρ_{4p} is the resistivity as measured using the 4-point probe.

Figure 4.10: Electrical measurement results as functions of $P_{Si/ZnO}$.

produced arguably the best structural properties. The resistivity measured by the 4-point probe on the same sample was 9.4×10^{-4} Ω cm. Comparison between ρ_{Hall} and ρ_{4p} for $P_{Si/ZnO} > 0.14$ suggests an estimated error range of about ±10%. Both Lai et al.[39] and Minami[13] attributed the increased carrier concentration and resulting low resistivity to Si atoms substituting on Zn sites in the ZnO lattice, resulting in free electrons. The former backed up this claim by pointing out the similar carrier concentration and resistivity trends and absolute values obtained by doping of ZnO with Al, which they believe to work by the same mechanism.

The line drawn between the mobility results for $P_{Si/ZnO} = 0.4$ and 0.44 is to indicate a point regarding the reliability of the measurements. Repeat room temperature Hall measurements on all of the Si doped samples indicated that mobility values to the left of the line should be attributed an error range of about ±5 [$\mathrm{cm^2/Vs}$], whereas those on the right-hand-side of the line could vary by several orders of magnitude. Thus, the numerical magnitudes of the latter should be disregarded, except to conclude that the mobility is very low and there is a great deal of scattering.

4.4.5 Optical Properties

Figure 4.11a summarises the optical transmittance results for the visible wavelength region for a selection of the Si doped samples, compared with the best undoped sample and the transmittance obtained using the plain glass substrate. The selection was made to aid the clarity of the figure and is representative of the transmittance trends with increasing Si content. The average transmittance between $400 < \lambda < 900$ nm varies little with $P_{Si/ZnO}$ except for higher doping levels where the film loses its structure as indicated by the loss of the (002) reflection in locked coupled scans when $P_{Si/ZnO} > 0.4$. When $0.14 < P_{Si/ZnO} < 0.44$, the transmittance in the visible region is comfortably above 75 % and above 80 % for the majority of wavelengths.

Figure 4.11b compares the transmittance at the UV absorption edge for all Si doping concentrations, split into regions labelled *a*, *b*, *c* and *d*. The dashed arrow from region *a* to region *b* indicates a blue-shift in the absorption edge which takes place between

$P_{Si/ZnO} = 0.14$ and 0.24, coinciding with the dramatic increase in carrier concentration and drop in resistivity observed in section 4.4.4. This blue-shift (the Burstein-Moss effect, see section 2.1.2.3) indicates the onset of degenerate semiconductor behaviour. Once $P_{Si/ZnO}$ is increased above 0.4, the dotted arrow in figure 4.11b marks a further blue-shift in the absorption edge to regions *c* and *d*, where it is increasingly similar in slope and position to that of the plain glass substrate. This is thought to be an indication of increasing occurrence of Si-O bonds forming SiO_2, and also coincides with degradation of both crystal structure and electrical properties of the films.

However, the samples with $P_{Si/ZnO} = 0.44$ and 0.5 have resistivities of 0.02 and 0.1 Ω cm respectively - similar to the resistivities exhibited by the samples in the work by Lai et al.[39] in which Si NCs were observed. As indicated in figure 4.11a, the $P_{Si/ZnO} = 0.40$ and 0.5 samples also have relatively high transmittance in the optical region: $> 75\%$ for $400 < \lambda < 900$ nm. Transmittance spectra are also shown in figure 4.12 for the $P_{Si/ZnO} = 0.24$, 0.4 and 0.5 samples over a greater wavelength range. For the former, the transmittance is $\gtrsim 80\%$ in the region $400 < \lambda < 1400$ nm while for the latter two, the transmittance is $\sim 80\%$ in the range $400 < \lambda < 1500$ nm.

The variation of the estimated optical bandgap with $P_{Si/ZnO}$ is shown in figure 4.13b, as calculated according to the approach outlined in section 3.4 and illustrated in figure 4.13a. The increase in the bandgap from $P_{Si/ZnO} = 0.08$ to 0.24 corresponds to the first observed blue-shift seen in figure 4.11b. The bandgap changes from ∼3.25 eV to ∼3.5 eV on entering the degenerate behaviour regime, as would be anticipated from the discussion in section 2.1.2.3.

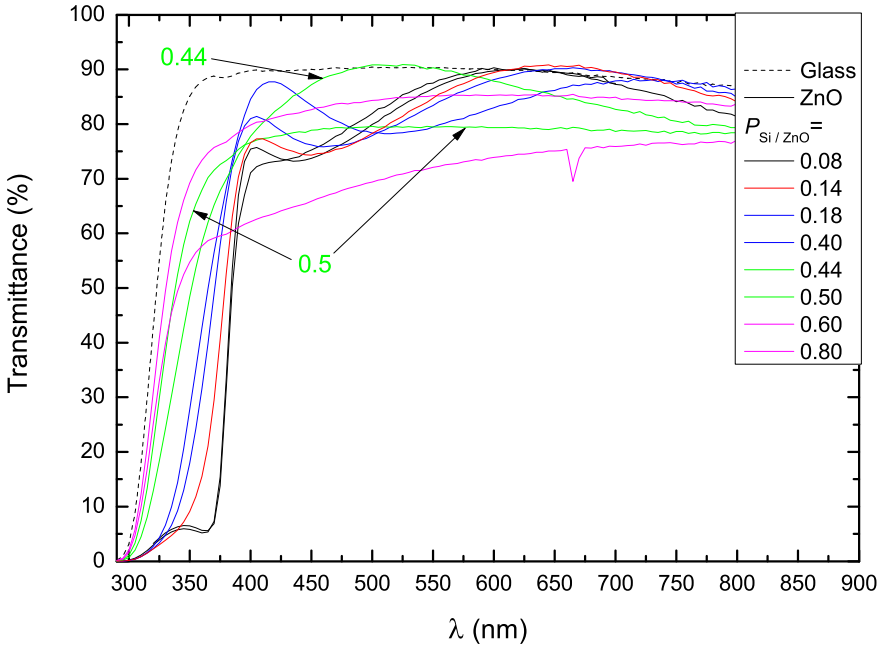

(a) Optical transmittance spectra for a selection of the Si doped ZnO samples. The selection was made for clarity and chosen to indicate the trend with increasing Si content. The downward spikes at around 660 nm are thought to be unknown measurement artifacts. The $P_{Si/ZnO} = 0.44$ and 0.5 transmittance spectra are highlighted.

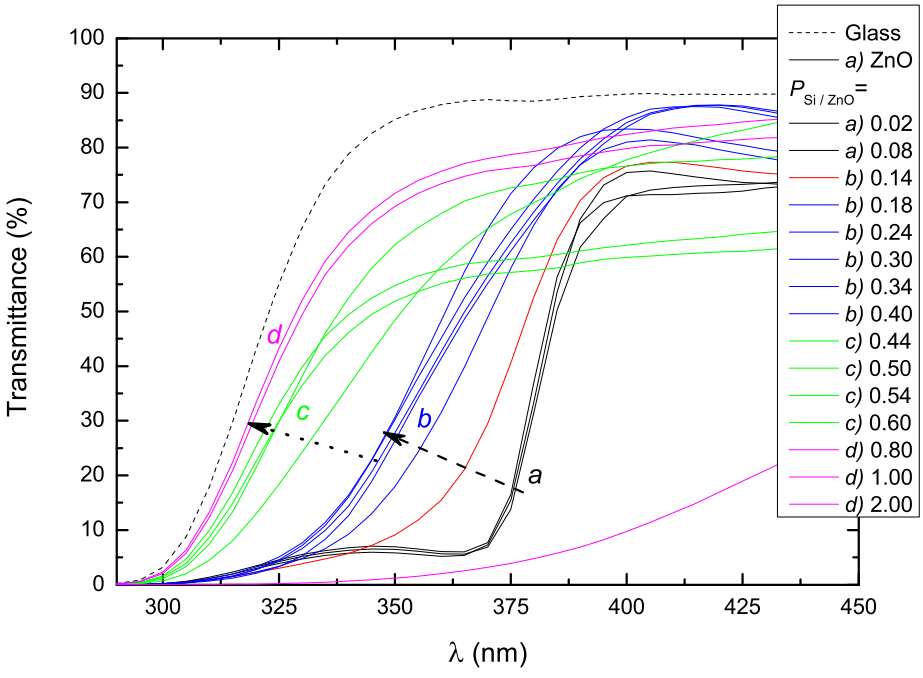

(b) The UV end of the spectrum, including all Si doped samples. The dashed arrow indicates the blue-shift in the absorption edge from region *a)* to region *b)* due to the Burstein-Moss effect, resulting in degenerate semiconductors. The dotted arrow indicates a further blue-shift from *b)* to *c)* with increasing Si content.

Figure 4.11: Optical transmittance spectra for all Si doped samples and the pure ZnO reference sample.

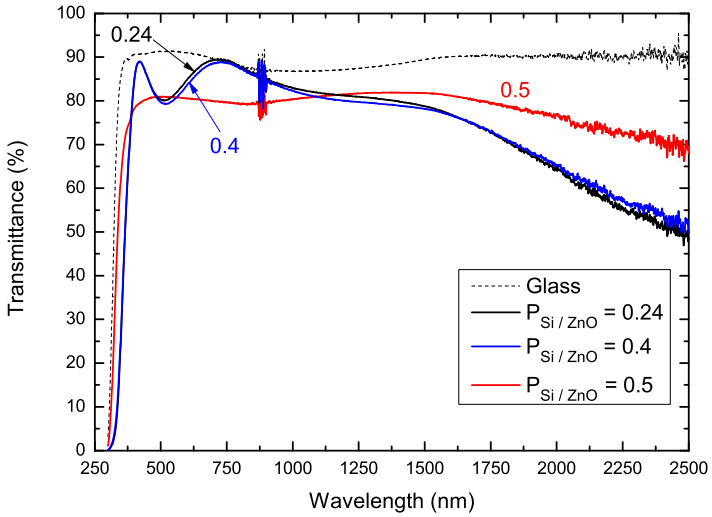

Figure 4.12: Transmittance spectra for the $P_{Si/ZnO} = 0.24$ and 0.5 samples over longer wavelength range from 300 to 2500 nm.

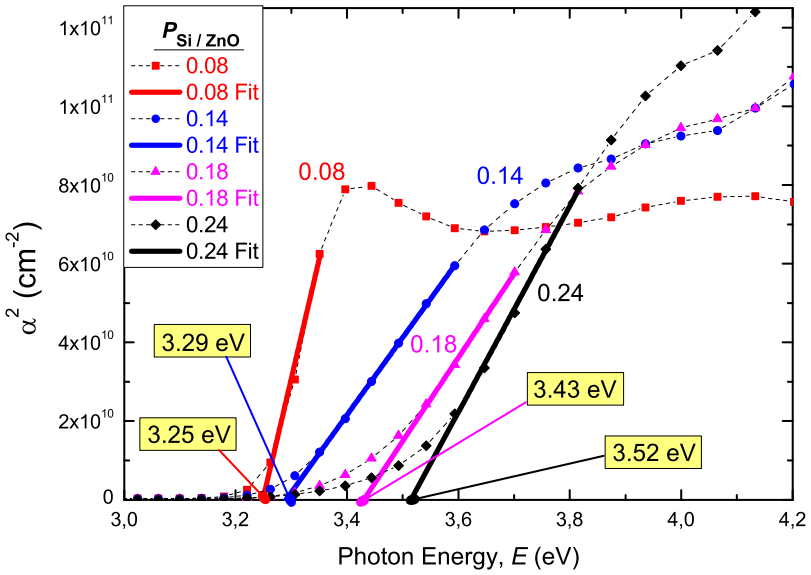

(a) Best fits to the curves for the square of the absorption coefficient vs. photon energy, illustrating the method of bandgap estimation. The samples chosen are those in the region of the blue-shift in the transmittance absorption edge, highlighted again in the figure below.

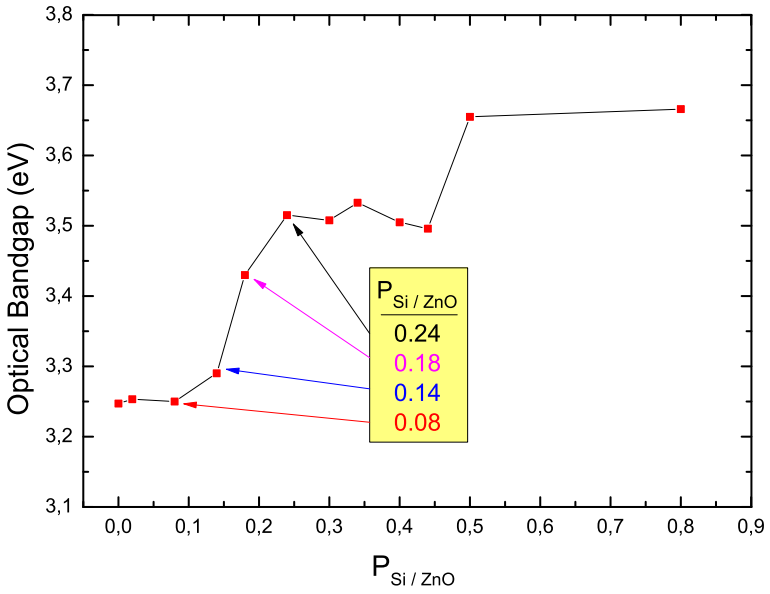

(b) Variation of the optical bandgap with increasing $P_{Si/ZnO}$. The samples for which the absorption coefficient plots are shown in the figure above are highlighted.

Figure 4.13: Estimation of the variation of the optical bandgap with $P_{Si/ZnO}$.

4.4.6 Temperature Dependent Hall Measurements

4.4.6.1 Undoped ZnO

Figure 4.14a shows three TDH resistivity measurements, M_1, M_2 and M_3, all made on the same undoped ZnO sample over a temperature range of $220 < T < 330$ K. M_1 and M_2 were independent measurements, each initiated 2 - 3 hours after entering the sample into the chamber. M_3 however, was a measurement performed after the sample had been in the chamber for ~ 25 hours, and therefore starved of light for that period. Comparing M_1 and M_2 suggests an estimated measurement error for TDH resistivity measurements of $\sim 5\%$.

Between $220 \leq T \leq 290$ K, the resistivity for M_3 is $\geq 50\%$ greater than that for M_1 and M_2. It is clear that exposure to light has a significant impact on the resistivity of the undoped ZnO film. Since the carrier concentration approximately follows the same trend with temperature in M_3 as in M_1 and M_2 (though with high degree of scattering), it is suggested that the effect is unrelated to the defect that is responsible for providing the free carriers. It is suggested instead that some kind of metastable defects are influenced by exposure to light, improving the mobility and the resistivity as indicated by figure 4.14a and also figure 4.16, where mobilities from the three measurements are compared.

4.4.6.2 TDH Curve Fitting

Curve fitting was performed on the experimental carrier concentration data shown in figure 4.14b, using a MATLAB® (The MathWorks, Natick, MA) code written by Dr. Ramòn Schifano[52, 64].

The inputs for the fitting program are the activation energy, E_a, the concentration of the donors, N_d, and the concentration of compensating acceptors, N_a. Arbitrary estimated values for these quantities were used to begin with. Several iterations of the fit were performed, adjusting E_a and the value of $N_d - N_a$ in order to obtain the best fit to the measured data. Figure 4.15 shows the measured carrier concentration plotted

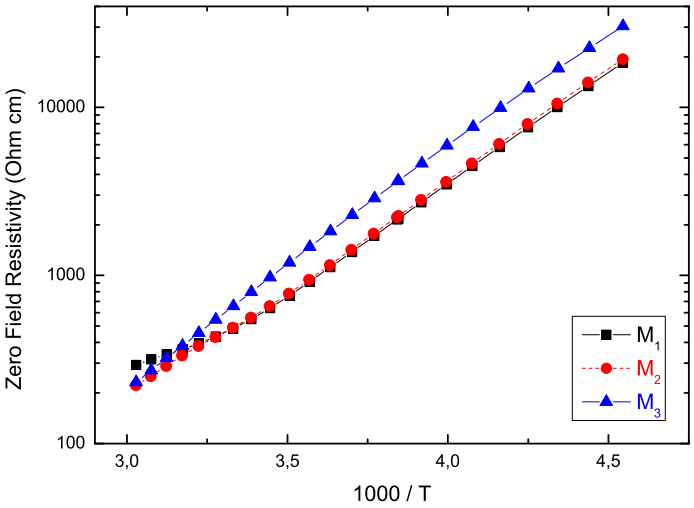

(a) TDH resistivity measurements on the undoped ZnO sample.

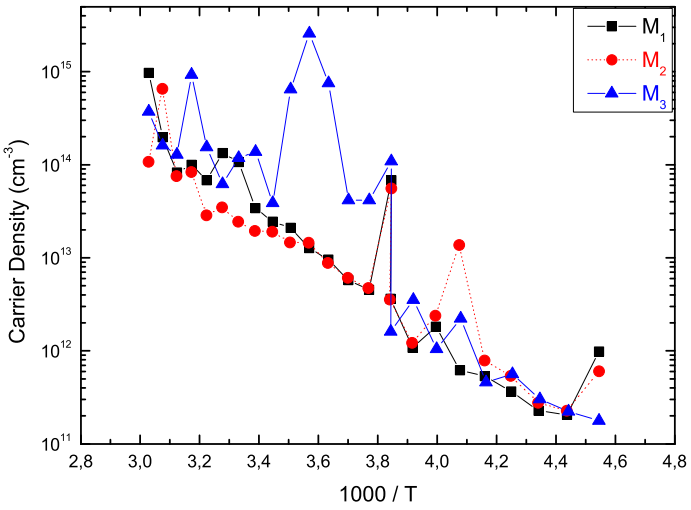

(b) TDH carrier concentration measurements on the undoped ZnO sample.

Figure 4.14: TDH measurements repeated three times on the same sample. M_1 and M_2 are independent measurements and M_3 is a measurement that was initiated after the sample had been in the sample chamber, (i.e. without exposure to light) for ~ 25 hours.

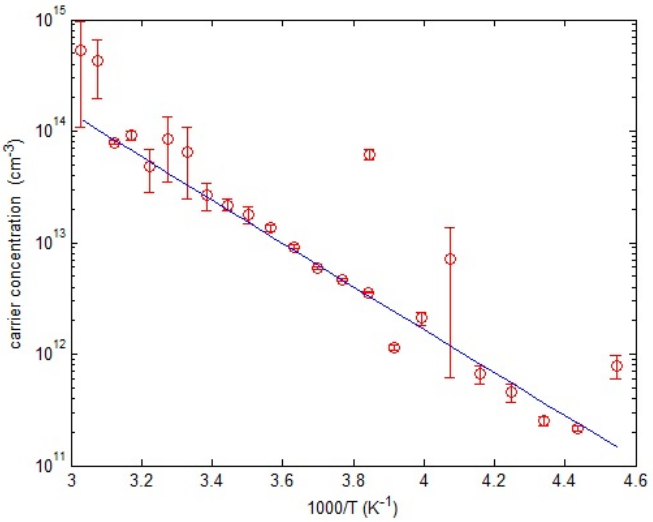

Figure 4.15: The measured carrier concentration data vs. inverse temperature with the line indicating the fit obtained by the MATLAB® script.

against $^{1000}/_{T}$ and the fitted line obtained by the program. The best fit shown in the figure used $E_a = 0.35$ eV and $N_d - N_a = 9.1 \times 10^{16}$ cm^{-3}. This energy corresponds to a defect that is generally observed in both single and polycrystalline ZnO[52], though its origin is an area of some controversy. It is generally labelled E_3 and often attributed to oxygen vacancies, V_O, acting as donors. Most agree that E_3 is intrinsic in nature since it appears regardless of the deposition method, and some attribute it to the second ionisation level of the zinc interstitial, Zn_i.

In order to extract independent values for N_d and N_a, a curve fit to the mobility is required, as mentioned in section 3.3.2. The mobilities for the same TDH measurements on the same undoped ZnO sample are shown in figure 4.16. Since this is a polycrystalline material, it is anticipated that the mobility will be largely determined by the transport of electrons through the grain boundaries. As explained in the work by Bube[65], the mobility determined by grain boundary transport is modelled by considering potential barriers at grain boundaries, with the mobility:

$$\mu_g = \left(\frac{e\bar{v}}{NkT}\right) e^{-\phi/kT} \tag{4.1}$$

where $\bar{v}$ is the thermal velocity of electrons, N is the number of potential barriers with

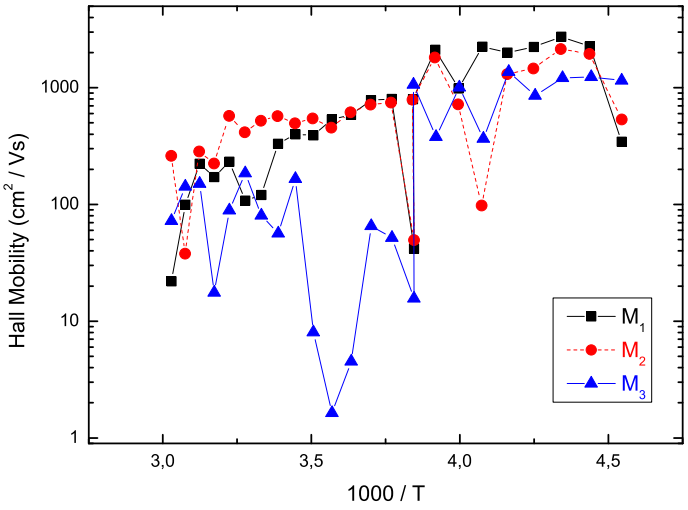

Figure 4.16: The three TDH measurements, M_1, M_2 and M_3, of the mobility of the undoped ZnO sample.

height, ϕ, per cm. Thus, one would expect the mobility to increase exponentially with decreasing $^{1000}/_{T}$, whereas figure 4.16 shows the opposite behaviour. Due to this and the high degree of scattering in the mobility measurements, the simulation could not be continued further.

It should also be noted, from figure 4.16, that the measured mobility values are very high. At $T \approx 295$ K, the measured mobility in $M_1 \sim 300$ $^{cm^2}/_{Vs}$ and in $M_2 \sim 570$ $^{cm^2}/_{Vs}$, and at lower temperatures, $T \approx 225$ K, the mobility is ~ 2000 $^{cm^2}/_{Vs}$ in both cases. For comparison, with single crystal ZnO one might expect a mobility of a few hundred $^{cm^2}/_{Vs}$ at similar temperatures[66]. Additionally, the mobility value plotted for the undoped sample in figure 4.10b was ~ 4 $^{cm^2}/_{Vs}$ with an estimated error range based on repeat measurements of about ± 5 $^{cm^2}/_{Vs}$. This value was obtained by variable field Hall measurements at room temperature in air, whereas the TDH measurements M_1 and M_2 were obtained whilst the sample was in a helium atmosphere. It is speculatively suggested that the difference in ambient atmosphere could be a source of discrepancy between TDH and room temperature Hall measurements since, for example, the chemisorption

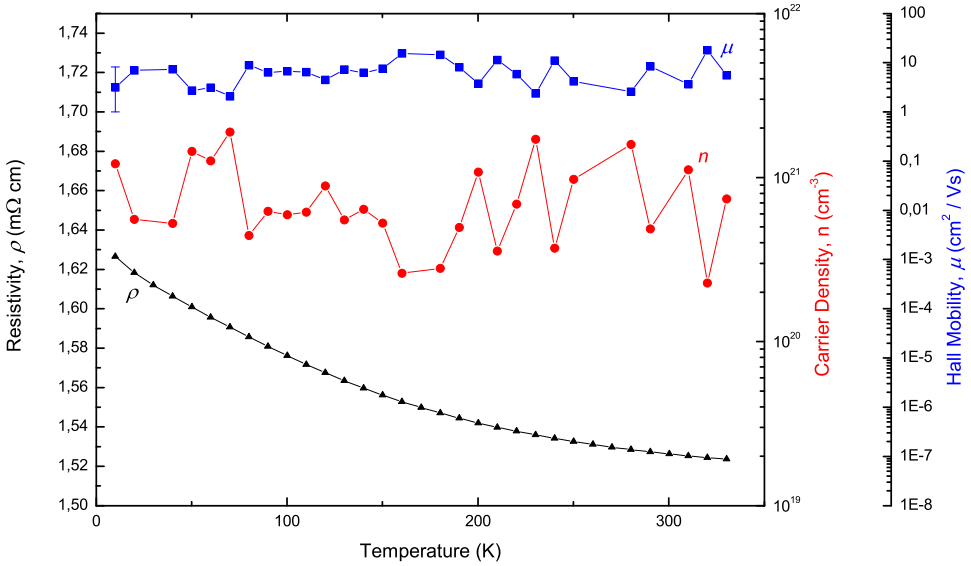

Figure 4.17: A summary of the results of a TDH measurement on the $P_{Si/ZnO} = 0.3$ sample with temperature variation between 10 and 330 K.

of oxygen on the ZnO surface can lower the surface conductivity[67]. In any case, measurements of mobility of several hundred or several thousand $^{cm^2}/_{Vs}$ should be treated with suspicion, particularly when, as is the case in figure 4.16, it is seen to vary by orders of magnitude over ~ 5 K changes in temperature. Further investigation into this would be required in order to draw any conclusions.

4.4.6.3 Degenerate n-type ZnO

Figure 4.17 shows the results of a TDH measurement performed on the $P_{Si/ZnO} = 0.3$ sample. This shows little variation in electrical properties with temperature - only ~ 100 $\mu\Omega$ cm change in resistivity and approximately constant carrier concentration and mobility, as expected for a degenerate semiconductor (see section 2.1.2.3).

4.5 Si Nanocrystal Formation

4.5.1 Predictions and Approach

The work by Lai et al.[39] found that the formation of Si-O bonds with increasing Si concentration (unsurprisingly) reduced the Si nanocluster density. However, they also observed a steep increase in the resistivity (five to six orders of magnitude) when this began to occur with increasing Si concentration. They attributed this to excess Si segregation into grain boundaries when the Si concentration is above a few percent. Nanocrystal formation was observed with Si concentration of 9.7 %, where the resistivity had increased to $\sim 0.1\ \Omega$ cm.

Optical evidence has been found here (shown in figure 4.11b) for the formation of Si-O bonds, indicated by the second blue-shift in the absorption edge with increasing $P_{Si/ZnO}$ values above 0.4. If Si nanocrystals were to form, it was considered likely that they would do so with target power ratio between $P_{Si/ZnO} = 0.40$ and 0.5 since at higher concentrations, the Si-O bonds may prevent the formation of NCs. The $P_{Si/ZnO} = 0.5$ sample has a resistivity of 0.1 Ω cm - very similar to the sample in which Lai et al. observed Si NCs by HRTEM imaging, so this was considered a likely candidate.

4.5.2 XRD

XRD locked coupled scans were initially used to search for reflections that might be associated with crystalline Si planes. Lai et al. successfully used the same approach as an initial indication of the presence of Si NCs before imaging them using transmission electron microscopy. They observed small Si related reflections corresponding to the Si (111), (220) and (311) reflections, as shown in figure 2.14a on page 40. Several locked coupled scans were performed on all Si doped samples with increased acquisition times running overnight, but Si related reflections could not be observed. Annealing at 800°C was attempted on samples with $P_{Si/ZnO} = 0.18$, 0.3 and 0.6 to see if this would encourage crystallisation of Si in the matrix, but further locked coupled scans still did not find Si related peaks.

4.5.3 Transmission Electron Microscopy

Transmission electron microscopy (TEM) was used to study the morphology of the undoped (figure 4.18), $P_{Si/ZnO} = 0.4$ (figure 4.19) and $P_{Si/ZnO} = 0.5$ (figure 4.20) samples on Si substrates. High resolution images provided insight into the films' micro-structure and the defects present in them. Energy filtered TEM (EF-TEM) facilitated the understanding of the distribution of various elements present in the films, thus complementing the XRD results. It was an important tool for visualising the variety of nanostructures present in the films.

TEM is a powerful imaging tool that incorporates many techniques for microstructural imaging and analysis. The operating principle is well explained in many texts such as that by Brandon and Kaplan[59]. Electrons are accelerated towards the sample, which must be prepared such that it is $\sim$ 10s of nanometres thick. As the name suggests, the images are formed by electrons that are transmitted through the sample. In a crystalline sample, some of the electrons pass straight through, while some are inelastically scattered. The most common imaging mode, *bright field* (BF) imaging, uses only the directly transmitted electrons, such that the contrast depends on the thickness and density of the sample. Conversely, *dark field* (DF) imaging allows only the diffracted beams to contribute, such that brighter regions of the image correspond to Bragg scattered electrons, and so the crystalline phases stand out against a dark background. High resolution TEM (HRTEM) uses the interference between diffracted and transmitted beams and is capable of resolving individual atoms in a lattice. Selected area electron diffraction (SAED) patterns can also be created, which allow identification of lattice planes in crystal structures. The final imaging method used here is energy filtered TEM (EF-TEM), an extension of the electron energy loss spectroscopy (EELS) technique. Here, the transmitted electrons are separated by a magnetic field, according to their energy. Their energy loss through inelastic scattering on passing through the sample is characteristic of the elements that they interact with. In EF-TEM, images are formed, where the bright regions correspond to detection of electrons with a particular energy, chosen using a slit, that is associated with the element that one wishes to

observe.

4.5.3.1 Undoped Sample

In Figure 4.18, four TEM images of the undoped ZnO sample are shown. Image (a) is a TEM micrograph of a cross section of the sample. The general structure of the film can be seen - the dark contrast running vertically from the substrate (bottom) to the film surface indicates a columnar structure, as expected from XRD measurements in section 4.3.3, which showed strong texturisation, with preferred orientation of grains being perpendicular to the sample surface. Though the nominal thickness of the samples was chosen to be $\sim$ 100 nm, this sample appears to be approximately 150 nm thick. Image (b) shows a selected area electron diffraction (SAED) pattern, which indicates a preferred [100] plane orientation in the direction parallel to the sample surface. This suggests that the preferred orientation in the direction perpendicular to the surface is the [002] plane, which again agrees with the XRD locked coupled scans in section 4.3.3. Image (c) is a high resolution TEM (HRTEM) image of the sample shown in *(a)*, focusing on the region close to the Si substrate/sample interface. The white horizontal line across the image suggests a $\approx$ 2 nm layer of SiO_2 at the interface, which means there will not have been epitaxial growth with the Si substrate in the early stages of the deposition. The approximate size of a single grain (measured in the direction parallel to the surface) is indicated on the image to be $\approx$ 20 nm. XRD measurements on the same sample, discussed in section 4.3.4, with results listed in table 4.2, indicated a grain size of 50 ± 2 nm, as measured in the direction perpendicular to the surface. In general, the grain size is underestimated in measurements via XRD, as regions close to the grain boundary will have a high density of defects and therefore the lattice may not not satisfy the Bragg condition in these regions. The significantly smaller grain size measurement in the horizontal direction via TEM further suggests a morphology consisting of columnar grains, with a long and a short axis. Image (d) is a HRTEM image showing stacking faults within a ZnO grain. The apparently high density of such defects within the grains will affect electron transport, thus limiting the conductivity

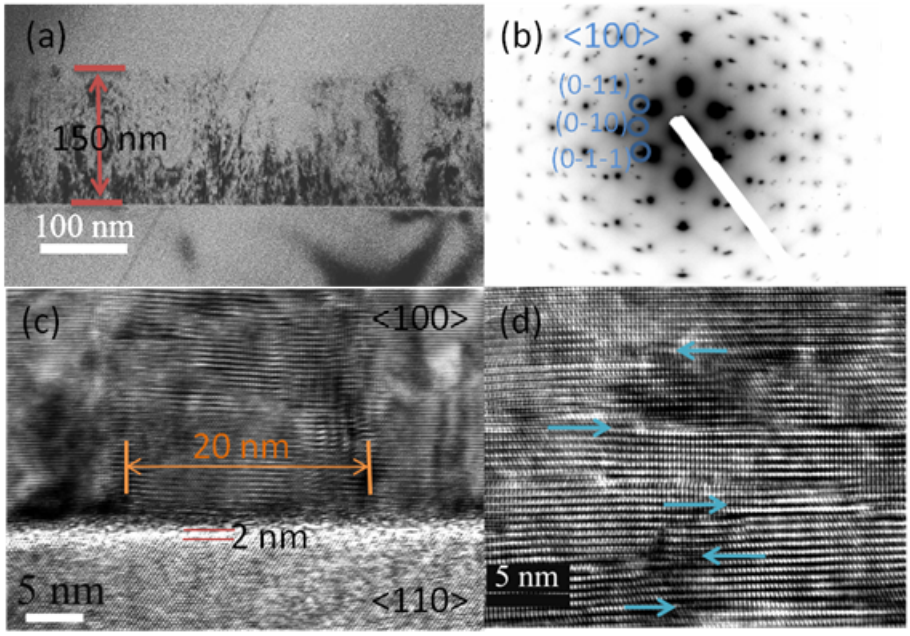

Figure 4.18: (a) A TEM micrograph of a cross section of the undoped ZnO film. The approximate thickness is marked. The columnar structure of the ZnO sample can been seen in dark contrast running vertically from the substrate to the film surface. (b) Selected area electron diffraction (SAED) pattern. (c) High resolution TEM image of *(a)*. An approximate measurement of grain size, in the horizontal direction, of 20 nm is indicated here. (d) HRTEM image of stacking faults within a single grain.

of the film.

4.5.3.2 Samples with Heavy Si Doping

The sample sputtered with $\mathbf{P_{Si/ZnO} = 0.4}$ was also imaged using various TEM techniques as shown in figure 4.19a. Image (a) is a TEM micrograph of a cross section of the sample, showing that there is still a columnar overall structure to the film. The thickness appears to be lower than that of the undoped sample in figure 4.18, at ~ 100 nm. This is unexpected as with the same deposition time, power applied to the ZnO target and the addition of sputtering from a Si target, it was anticipated that the thickness would increase slightly. Image (b) is a HRTEM image in the region of the interface, again indicating the roughly 2 nm thick SiO_2 layer at the interface that was also seen in the undoped sample.

Image (c) is a HRTEM image within the ZnO/Si sample revealing a large number of nanocrystals. We can look to the SAED pattern in image (d) to tell us more about what is seen in the HRTEM image. The dark spots in the diffraction pattern originate from the Si substrate, but there are also two sets of rings visible in the pattern. Dark spots correspond to crystal lattices, whereas rings in diffraction patterns originate from small, nano-scale crystal structures. As indicated in the image, two of the rings correspond to the (111) and (002) Si planes - evidence for the presence of Si nanocrystals. Two more rings in the pattern correspond to the ZnO (002) and (100) planes, as indicated in the figure. The XRD locked coupled scan for this sample exhibited a small intensity of the (002) peak compared to samples with lower Si content (see figure 4.9b on page 85), suggesting a significantly reduced degree of texturisation. In addition, the grain size was seen to have been reduced to ~ 14 nm. The SAED observation of rings corresponding to these planes indicates that the ZnO in this sample is in the form of nanocrystals without a strong preferred orientation. Image (e) is a dark field image of the sample, where the white regions suggest an approximate size for the observed NCs of $\sim 10 - 20$ nm, agreeing approximately with the XRD grain size measurement.

Figure 4.19b shows energy filtered TEM (EF-TEM) images, where the contrast depends on the elemental composition of the sample. In image (a), the slit is set to 17 ± 2 eV, such that the light regions in the image correspond to Si - hence the substrate in the lower part of the image is light, and the bright regions in the sample imply Si NCs present in the sample layer. Again, the scale suggests an approximate size between 10 and 20 nm. In image (b), the slit is set to 22 ± 2 eV, such that the bright regions correspond to SiO_2. The ~ 2 nm layer at the interface, seen also in figure 4.18 *(c)* and 4.19a *(b)* is visible as a white line across the lower region of the image. White spots are also visible in the sample layer, implying SiO_2 nano-grains, which are amorphous, since they did not appear in the SAED pattern in figure 4.19a or the XRD scans in section 4.4.3. Image (c) is a core loss map for the oxygen K-edge. The approximately uniform white appearance of the sample indicates that it is almost completely oxygenated, though the grey line to the left side of the sample in the

image indicates an oxygen deficient region which may be related to a grain boundary. Image (d) is an EF-TEM image showing an approximately uniform distribution of Zn in the sample, which, according to the SAED pattern in figure 4.19a, is in the form of nanocrystals.

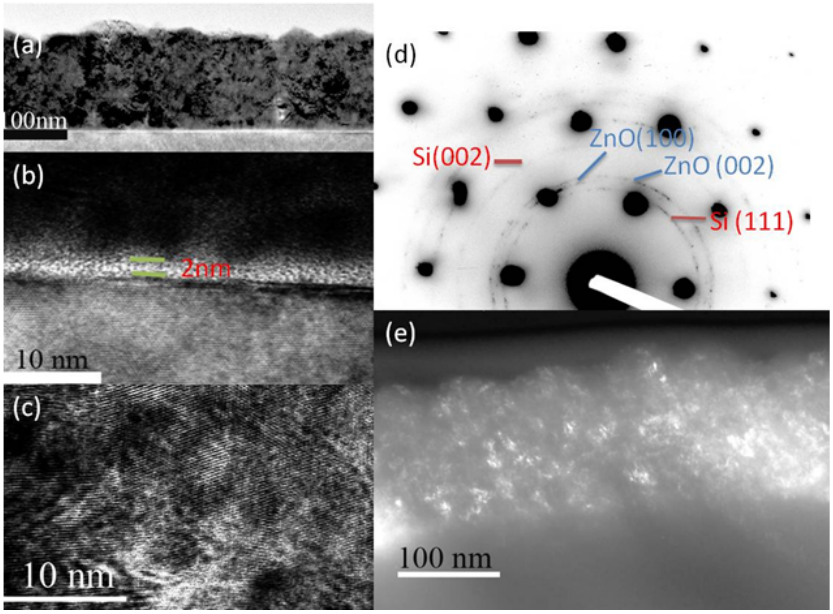

(a) (a) A TEM micrograph of a cross-section of the $P_{Si/ZnO} = 0.4$ sample, with the substrate at the bottom of the image and the sample across the centre. The thickness is measured to be ~ 100 nm. (b) The ~ 2 nm thick SiO_2 layer visible at the substrate/sample interface. (c) HRTEM image of the ZnO/Si layer, showing multiple nanocrystals. (d) The SAED pattern - the indicated rings correspond to both ZnO and Si nanocrystalline phases. The dark spots originate from the substrate. (e) A dark field image of the ZnO/Si layer. The light spots on the image are nanocrystals of $\sim 10-20$ nm.

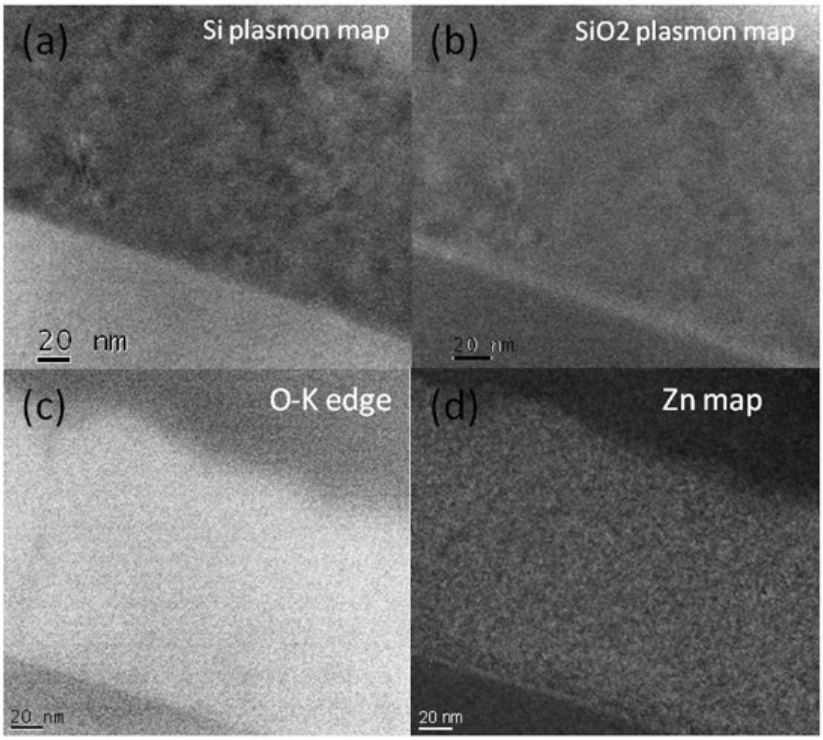

(b) Energy filtered TEM (EF-TEM) element mapping for Si, SiO_2, O and Zn in the $P_{Si/ZnO} = 0.4$ sample.

Figure 4.19: TEM images obtained from the $P_{Si/ZnO} = 0.4$ sample.

The sample sputtered with $\mathbf{P_{Si/ZnO} = 0.5}$ was also investigated using TEM imaging. For this sample, the resistivity of $\sim 0.1\ \Omega$ cm was similar to that of the sample that exhibited Si nanocrystals in the work by Lai et al. However, as discussed in section 4.4.3, the (002) peak is no longer visible in XRD locked coupled scans, suggesting significant reduction in preferred orientation and loss of crystal structure.

Figure 4.20 shows the TEM and EF-TEM imaging results. Image (a) is a HRTEM image taken at the interface, with the substrate on the left hand side and the sample on the right. The SiO_2 layer at the interface, measuring approximately 2 nm, is present as in the previous two samples investigated by TEM. A degree of columnar structure to the growth is still present, but the columns are narrower than in the undoped sample ($\sim$ 10 nm). Image (b) is an EF-TEM image showing Si-rich regions as bright against a dark background, with the bright Si substrate on the left and the sample on the right. This image, as well as image (c), where SiO_2 is highlighted, appear to show that Si and SiO_2 are largely present in the boundaries between the ZnO grains. This is considered likely to be the source of the increase in resistivity, which is nearly two orders of magnitude greater than that of the $P_{Si/ZnO} = 0.4$ sample (assuming the resistivity is similar to that of the equivalent glass-substrate sample in both cases). The mobility in the glass-substrate equivalent of this sample was significantly reduced from that of the previous two samples, as shown in figure 4.10b on page 87 and it is suggested that Si and SiO_2 in the grain boundaries are the likely cause of this - the same conclusion drawn by Lai et al.[39]. Finally, image (d) is an EF-TEM image that indicates the distribution of Zn in the sample, signified by bright regions against the dark background. It suggests that the film is relatively Zn-rich close to the interface, with increasing Si and SiO_2 content with distance from the substrate. The ZnO grains appear to be approximately 10 nm in size, but neither these, nor the Si or SiO_2 grains are crystallised. This is the reason why there was no signal when performing the locked coupled XRD scan on this sample.

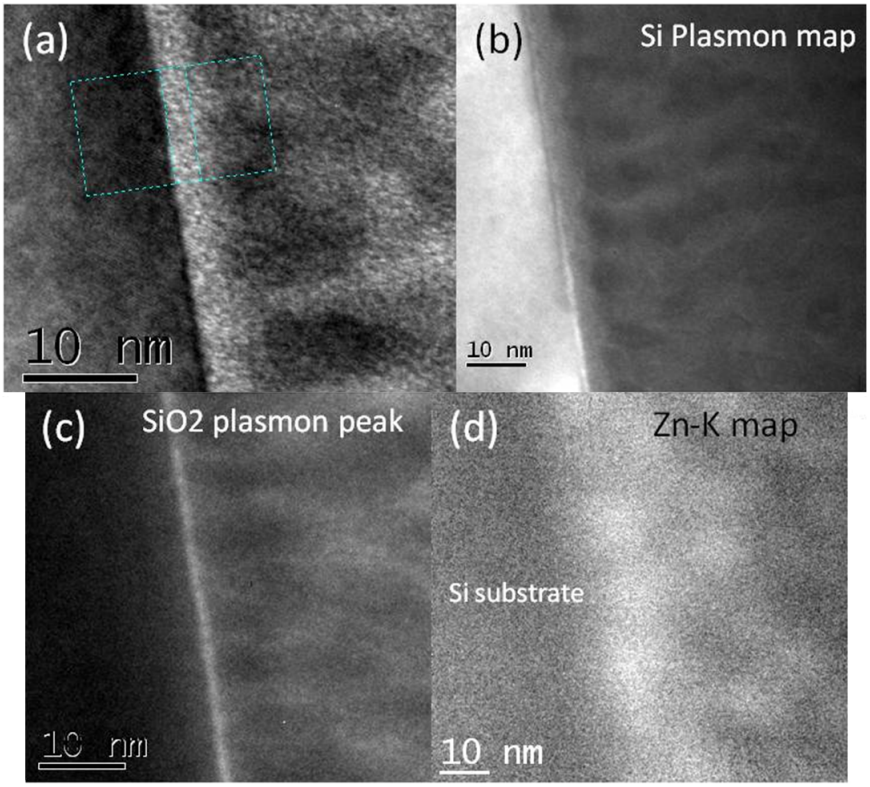

Figure 4.20: (a) HRTEM and (b, c and d) EF-TEM images for the sample sputtered with $P_{Si/ZnO} = 0.5$.

4.5.3.3 Discussion

TEM imaging has provided strong evidence for the formation of Si nanocrystals for the sample with $P_{Si/ZnO} = 0.4$. The equivalent glass-substrate sample exhibits a transmittance of $> 78\%$ in the optical region between 400 and 1500nm, an estimated optical bandgap of ~ 3.5 eV, a carrier concentration of $\sim 4 \times 10^{20}$ cm^{-3} and a resistivity of $\sim$3.7 mΩ cm. Assuming a similar resistivity of the Si-substrate sample, it appears that Si is participating in doping as well as forming nanocrystals. SiO_2 was also observed, which could be taken to indicate that the doping mechanism may in fact be via the creation of oxygen vacancies, which can act as donors. The TCO review by Minami[24] suggests that successful candidates for TCOs should have resistivity of $\sim 10^{-3}$ Ω cm or below, carrier concentration $\sim 10^{20}$ cm^{-3} and transmittance above $\sim 80\%$ in the visible wavelength range, suggesting that ZnO films incorporating Si nanocrystals could potentially be candidates for TCO applications in light of results such as these. The imaging also suggests that further increasing the Si content destroys the crystallinity of the film structure and promotes instead the formation of amorphous grains of ZnO, Si and SiO_2. An upper limit on the power ratio can be set at $P_{Si/ZnO} < 0.5$ for future work on incorporating Si NCs in ZnO films by co-sputtering.

4.6 X-Ray Photoelectron Spectroscopy

X-ray photoelectron spectroscopy (XPS) is a technique which measures the elemental composition of a sample within the top ~ 10 nm below the surface. A monochromatic beam of x-ray photons is absorbed by atoms in the sample, ejecting secondary electrons with energy that is characteristic of the element from which they were ejected. The working principle is well explained in texts such as that by Brandon and Kaplan[59]. It was used on a selection of the Si-doped samples in order to obtain an estimate as to their Si content.

The sample with the best properties obtained by Si doping was sputtered with target ratio of $P_{Si/ZnO} = 0.24$ (see section 4.4.4). The Si content was determined by XPS to

be $\sim$ 2.3 atomic percent. This was approximately as expected, with reference to the previous work with Si doping of ZnO. Both Lai et al.[39] and Minami[13] found the optimum electronic properties were obtained with Si content of $\sim 1-3$ atomic percent, as discussed in section 2.5.

XPS measurements were also performed on the samples that were investigated with TEM, sputtered with power ratios $P_{Si/ZnO} = 0.4$ and 0.5. In the case of the $P_{Si/ZnO} = 0.4$ sample, in which Si nanocrystals were observed, the Si content was measured to be $\sim$ 3.6 at%. Again, for comparison, Lai et al.[39] observed Si nanocrystals with Si contents between 0.5 and $\sim$ 40 at%, with the largest diameter measured when Si content was $\sim$ 10 at%. The Si content for the $P_{Si/ZnO} = 0.5$ sample was measured by XPS to be$\sim$ 19 at%, while the Zn content was measured to be only 9 at%. Looking at the EF-TEM imaging for this sample in figure 4.20, image (d), it was apparent that the film was relatively Zn-rich close to the interface, whilst Si and SiO_2 was present in increasing concentration towards the surface. Since the XPS measurement will only have measured the content within the top $\sim$ 10 nm of the film, it is no surprise that the Si content is so high, whilst the Zn content is very low.

It is suggested that the Rutherford back-scattering spectroscopy is used in future work, to measure the elemental composition of the samples in order to find the relationship between $P_{Si/ZnO}$ and the Si content.

Chapter 5

Conclusion

5.1 Summary

Radio frequency magnetron sputtering of ZnO thin films was performed on Si and glass substrates. The sputtering parameters, specifically the target power, substrate temperature, gas flow pressure and oxygen content, were varied in order to optimise the structural and optical properties of the resulting films. Co-sputtering was then performed, to obtain Si doped ZnO thin films of $\sim$ 100 nm thickness. The power applied to the Si target was varied, keeping all other sputtering conditions fixed in order to obtain films with a wide range of Si contents. The variation of the electrical, structural and optical properties with Si content was assessed in order to find the optimum sputtering conditions for producing highly transparent and conductive films. Higher Si content films were investigated for the formation of Si nanocrystals using TEM and EF-TEM imaging techniques

An optimum combination was achieved between the sputtering parameters, with the best undoped ZnO film exhibiting a high degree of texturisation and grain size of $\sim$ 28 nm and $\sim$ 50 nm on glass and Si substrates respectively, as measured in the c-axis direction, by XRD. HRTEM images of the sample on Si substrate indicated a grain size of $\sim$ 20 nm in the horizontal direction. The best undoped ZnO films were deposited using a target power of 50 Watts, a substrate temperature of 450°C and a pure Ar

gas flow rate of 70 SCCM (working pressure of 16.3 mTorr). Doping with Si, using a co-sputtering target power ratio of $P_{Si/ZnO} = 0.24$ was seen to result in a grain size increase from ~ 28 nm to ~ 36 nm over the undoped case (on glass substrates), whilst the film stress was reduced from ~ 0.8 GPa to ~ 0.1 GPa. The expected correlation between structural and electrical quality was confirmed, since the $P_{Si/ZnO} = 0.24$ sample also exhibited the lowest resistivity of $\sim 1 \times 10^{-3}$ Ω cm, with a carrier concentration of $\sim 5 \times 10^{20}$ cm^{-3}. This represented a reduction in resistivity over five orders of magnitude from the undoped case. The low mobility of ~ 8 $^{\mathrm{cm}^2}/_{\mathrm{Vs}}$ was likely to have been the main obstacle for further improvements in resistivity. The transmittance for this sample was $\gtrsim 80\%$ in the wavelength range $400 < \lambda < 1400$ nm.

The prominent E_3 donor defect was identified through TDH measurements on the undoped ZnO sample, and curve fitting to the temperature dependence of the carrier concentration suggested that its position in the band gap was $\sim E_C - 0.35$ eV and that the difference between the concentration of donors and compensating acceptors present was $(N_d - N_a) \sim 9 \times 10^{16}$ cm^{-3}. The TDH measurements also revealed a significant increase in resistivity and decrease in mobility as a result of samples being starved of light for ~ 24 hours. It is suggested that some kind of metastable defects are responsible, which are influenced by exposure to light. Both TDH measurements and transmittance measurements confirmed degenerate semiconductor behaviour of samples with $0.14 \lesssim P_{Si/ZnO} \lesssim 0.4$.

TEM and EF-TEM investigations of the micro-structure of the $P_{Si/ZnO} = 0.4$ sample on Si substrate revealed the presence of Si nanocrystals, ~ 20 nm in size. Assuming electrical properties similar to the equivalent sample on glass substrate, this film maintains a relatively low resistivity of $\sim 3 \times 10^{-3}$ Ω cm, carrier concentration of $\sim 10^{20}$ cm^{-3} and mobility on the same order of magnitude as the $P_{Si/ZnO} = 0.24$ sample discussed above. This suggests that Si is participating in doping as well as forming nanoclusters, even though significant formation of SiO_2 is apparent. The crystal structure is entirely lost in the $P_{Si/ZnO} = 0.5$ sample and TEM images show migration of Si and SiO_2 into the grain boundaries, likely causing the significant increase in resistivity. Thus, an upper

limit has been placed on the power ratio of $P_{Si/ZnO} < 0.5$ for investigation of ZnO films incorporating Si nanocrystals, and it is suggested that the co-sputtering technique has potential for further work on developing such films.

5.2 Further Work

5.2.1 Si Doping of ZnO

Further work is necessary to try to increase the electron mobility of Si-doped ZnO films, since this appears to be the limiting factor. Other workers on ZnO using similar sputtering methods had similar mobility results for Si doped films[39, 13]. It would be interesting to investigate the unexplained effects observed in Hall measurements: Firstly, the effect on the resistivity that seems to be caused by exposure to light, and secondly, the effect of the presence of gases such as oxygen in the sample chamber during measurements (see section 4.4.6). It may also be worth investigating the influence of the film thickness on the electrical properties of the Si doped ZnO films. Minami[13] found that the mobility of such films was dependent on thickness below ~ 300 nm. The Si content should also be determined using RBS. Finally, further studies into the nature of the Si doping mechanism in ZnO are suggested.

5.2.2 Si Nanocrystals

It has been established here that incorporating Si NCs into transparent, conductive films of ZnO is possible using the co-sputtering method with a target power ratio of $P_{Si/ZnO} = 0.4$. It has also been found that the crystal structure of the nanograins is lost at $P_{Si/ZnO} = 0.5$, but a lower limit has not yet been set. Therefore, further TEM investigation is suggested, to establish the power ratio range over which Si NCs form and their size variation could then be investigated as a function of Si content or target power ratio. Lai et al.[39] found that the Si NC diameter increases linearly with increasing RF power of the Si target and that the density of NCs is approximately constant up to a threshold where an increase in Si-O bonds precludes their formation. Investigation into

the electrical and optical properties of the NCs would perhaps be the next logical step, in particular using photo-luminescence (PL) measurements to determine the bandgap.

Appendix A

Supplementary Results

A.1 Pure ZnO Transmittance

The plots below are supplementary results from section 4.3.3, showing the transmittance results for the 150W and 250W sputter depositions at the four substrate temperatures.

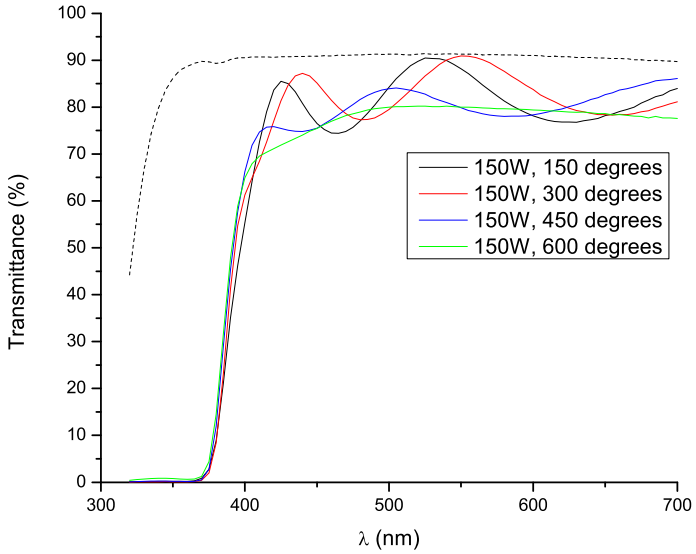

(a) Optical transmittance spectra for ZnO films sputtered on glass substrates for 1 hour with target power of 150 Watts.

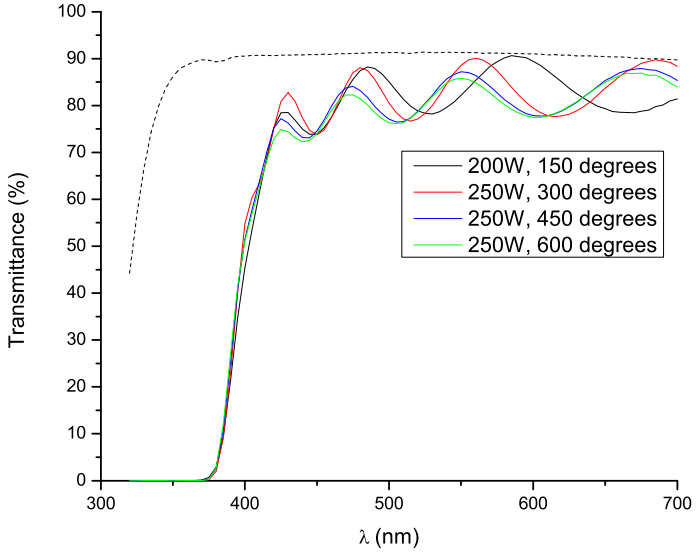

(b) Optical transmittance spectra for ZnO films sputtered on glass substrates for 1 hour with target power of 250 Watts.

Figure A.1: Optical transmittance spectra for 150 and 250 Watt film depositions with varying substrate temperatures.

Bibliography

[1] V. Petrova-Koch. Milestones of Solar Conversion and Photovoltaics. In *High-Efficient Low-Cost Photovoltaics*, volume 140 of *Springer Series in Optical Sciences*, pages 1–5. Springer Berlin, Heidelberg, 2009.

[2] C. Kittel and P. McEuen. *Introduction to Solid State Physics*. Wiley New York, 8th edition, 2005.

[3] J. Nelson. *The Physics of Solar Cells*. Imperial College Press, 2009.

[4] S. A. Campbell. *Fabrication Engineering at the Micro- and Nanoscale*. The Oxford Series in Electrical and Computer Engineering. Oxford University Press, 3rd edition, 2008.

[5] E. Burstein. Anomalous Optical Absorption Limit in InSb. *Physical Review*, 93(3):632, 1954.

[6] H. Morkoc and U. Ozgur. *Zinc Oxide: Fundamentals, materials and device technology*. Vch Verlagsgesellschaft Mbh, 2009.

[7] R. B. Heller, J. McGannon, and A. H. Weber. Precision Determination of the Lattice Constants of Zinc Oxide. *Journal of Applied Physics*, 21:1283, 1950.

[8] D. C. Look, J. W. Hemsky and J. R. Sizelove. Residual Native Shallow Donor in ZnO. *Physical review letters*, 82(12):2552–2555, 1999.

[9] K. Vanheusden, C. H. Seager, W. L. Warren, D. R. Tallant and J. A. Voigt. Correlation between photoluminescence and oxygen vacancies in ZnO phosphors. *Applied physics letters*, 68:403, 1996.

[10] A. Janotti and C. G. Van de Walle. Native point defects in ZnO. *Phys. Rev. B*, 76(16):165202, Oct 2007.

[11] A. F. Kohan, G. Ceder, D. Morgan and C. G. Van de Walle. First-principles study of native point defects in ZnO. *Phys. Rev. B*, 61(22):15019–15027, Jun 2000.

[12] C. G. Van de Walle. Hydrogen as a Cause of Doping in Zinc Oxide. *Phys. Rev. Lett.*, 85(5):1012–1015, Jul 2000.

[13] T. Minami, H. Nanto, and S. Takata. Highly conductive and transparent zinc oxide films prepared by rf magnetron sputtering under an applied external magnetic field. *Applied Physics Letters*, 41(10):958–960, November 1982.

[14] B.G. Streetman and S.K. Banerjee. *Solid State Electronic Devices*. Pearson Prentice-Hall, 6 edition, 2010.

[15] T. Markvart and L. Castaner, editors. *Solar Cells: Materials, Manufacture and Operation*. Elsevier, 2005.

[16] A. Slaoui and R.T. Collins. Advanced inorganic materials for photovoltaics. *MRS bulletin*, 32(03):211–218, 2007.

[17] R.M. Swanson. A Vision for Crystalline Silicon Photovoltaics. *Progress in Photovoltaics: Research and Applications*, 14(5):443–453, 2006.

[18] W. Shockley and H.J. Queisser. Detailed Balance Limit of Efficiency of p-n Junction Solar Cells. *Journal of Applied Physics*, 32(3):510–519, 1961.

[19] The Solar Buzz website at www.solarbuzz.com, 2011.

[20] M. Tanaka, S. Okamoto, S. Tsuge, and S. Kiyama. Development of HIT solar cells with more than 21 percent conversion efficiency and commercialization of highest

performance HIT modules. In *Proceedings of 3rd World Conference on Photovoltaic Energy Conversion, 2003.*, volume 1, pages 955–958. IEEE.

[21] Y. Tsunomura, Y. Yoshimine, M. Taguchi, T. Baba, T. Kinoshita, H. Kanno, H. Sakata, E. Maruyama, and M. Tanaka. Twenty-two percent efficiency HIT solar cell. *Solar Energy Materials and Solar Cells*, 93(6-7):670–673, 2009.

[22] The 'Solar' section of the Sanyo US website at us.sanyo.com/Solar, 2011.

[23] T. J. Coutts, T. O. Mason, J. D. Perkins and D. S. Ginley. Transparent Conducting Oxides: Status and Opportunities in Basic Research. In *National Renewable Energy Laboratory*, 1999.

[24] T. Minami. Transparent Conducting Oxide Semiconductors for Transparent Electrodes. *Semiconductor science and technology*, 20:S35–S44, 2005.

[25] A. J. Nozik, M. C. Beard, J. M. Luther, M. Law, R. J. Ellingson, and J. C. Johnson. Semiconductor Quantum Dots and Quantum Dot Arrays and Applications of Multiple Exciton Generation to Third-Generation Photovoltaic Solar Cells. *Chemical Reviews*, 110(11):6873–6890, 2010.

[26] A.J. Nozik. Multiple Exciton Generation in Semiconductor Quantum Dots. *Chemical Physics Letters*, 457(1-3):3–11, 2008.

[27] M.C. Beard, K.P. Knutsen, P. Yu, J.M. Luther, Q. Song, W.K. Metzger, R.J. Ellingson, and A.J. Nozik. Multiple Exciton Generation in Colloidal Silicon Nanocrystals. *Nano Lett*, 7(8):2506–2512, 2007.

[28] F.J. Owens and C.P. Poole. *The Physics and Chemistry of Nanosolids.* Wiley-Blackwell, 2008.

[29] A. Shabaev, A. L. Efros and A. J. Nozik. Multiexciton generation by a single photon in nanocrystals. *Nano letters*, 6(12):2856–2863, 2006.

[30] A.J. Nozik. Spectroscopy and hot electron relaxation dynamics in semiconductor quantum wells and quantum dots. *Annual Review of Physical Chemistry*, 52(1):193–231, 2001.

[31] A. J. Nozik. Quantum Dot Solar Cells. *Physica E: Low-dimensional Systems and Nanostructures*, 14(1-2):115–120, 2002.

[32] H. Liu, V. Avrutin, N. Izyumskaya, U. Ozgur, and H. Morkoc. Transparent conducting oxides for electrode applications in light emitting and absorbing devices. *Superlattices and Microstructures*, 2010.

[33] A. W. Metz, R. John, J. G. Zheng, R. P. Lobo, Y. Yang, J. Ni, C. L. Stern, V. P. Dravid, N. Bontemps, C. R. Kannewurf and others. Transparent Conducting Oxides: Texture and microstructure effects on charge carrier mobility in MOCVD-derived CdO thin films grown with a thermally stable, low-melting precursor. *Journal of the American Chemical Society*, 126(27):8477–8492, 2004.

[34] K. Ellmer. Resistivity of Polycrystalline Zinc Oxide Films: current status and physical limit. *Journal of Physics D: Applied Physics*, 34:3097, 2001.

[35] T. Minami. New n-Type Transparent Conducting Oxides. *Mrs Bulletin*, 25(08):38–44, 2000.

[36] H.C. Lee. Electron scattering mechanisms in indium-tin-oxide thin films prepared at the various process conditions. *Applied surface science*, 252(10):3428–3435, 2006.

[37] K. Ellmer and R. Mientus. Carrier Transport in Polycrystalline Transparent Conductive Oxides: A comparative study of zinc oxide and indium oxide. *Thin Solid Films*, 516(14):4620–4627, 2008.

[38] M. Birkholz, B. Selle, F. Fenske, and W. Fuhs. Structure-function relationship between preferred orientation of crystallites and electrical resistivity in thin polycrystalline ZnO:Al films. *Phys. Rev. B*, 68(20):205414, Nov 2003.

[39] Li-Wen Lai, Chih-Hong Liu, Ching-Ting Lee, Li-Ren Lou, Wen-Yung Yeh and Mu-Tao Chu. Investigation of silicon nanoclusters embedded in ZnO matrices deposited by cosputtering system. *Journal of Materials Research*, 23:2506–2511, 2008.

[40] K. Ellmer, A. Klein, and B. Rech. *Transparent Conductive Zinc Oxide: Basics and applications in thin film solar cells.* Springer Verlag, 2008.

[41] K. Ellmer. Magnetron Sputtering of Transparent Conductive Zinc Oxide: Relation between the sputtering parameters and the electronic properties. *Journal of Physics D: Applied Physics*, 33:R17, 2000.

[42] B. Chapman. *Glow Discharge Processes: sputtering and plasma etching.* Wiley New York, 1980.

[43] P. Sigmund. Theory of sputtering. I. Sputtering yield of amorphous and polycrystalline targets. *Physical Review*, 184(2):383, 1969.

[44] F. C. Van de Pol, F. R. Blom and T. J. Popma. RF planar magnetron sputtered ZnO films I: structural properties. *Thin Solid Films*, 204(2):349–364, 1991.

[45] J.A. Thornton. Influence of Apparatus Geometry and Deposition Conditions on the Structure and Topography of Thick Sputtered Coatings. *Journal of Vacuum Science and Technology*, 11(4):666–670, 1974.

[46] B. A. Movchan and A. V. Demchishin. Study of the Structure and Properties of Thick Vacuum Condensates of Nickel, Titanium, Tungsten, Aluminium Oxide and Zirconium Dioxide. *Phys. Met. Metallogr.*, 28(4):83–90, 1969.

[47] M. Birkholz, P.F. Fewster, and C. Genzel. *Thin film analysis by X-ray scattering.* Vch Verlagsgesellschaft Mbh, 2006.

[48] R. Cebulla, R. Wendt, and K. Ellmer. Al-doped zinc oxide films deposited by simultaneous rf and dc excitation of a magnetron plasma: Relationships between plasma parameters and structural and electrical film properties. *Journal of applied physics*, 83:1087, 1998.

[49] H.H. Landolt and R. Bornstein. *Landolt-Bornstein Zahlenwerte und Funktionen Aus Naturwissenschaften und Technik: Neue Serie*, volume 17. Springer, 1983.

[50] P.Scherrer. Bestimmung der Größe und der inneren Struktur von Kolloidteilchen mittels Röntgenstrahlen. *Nachr. Königl. Gesell. Wiss. Göttingen*, 98, 1918.

[51] C. L. Barnes T. N. Blanton, M. Lelental. The use of X-ray diffraction rocking curve methodology for assessment of the c-axis orientation in Bi—Sr—Ca—Cu—O superconducting thin films. *Physica C: Superconductivity*, 184:119–126, December 1991.

[52] R. Schifano. *Schottky contacts and electrical characterization of n-type hydrothermally grown ZnO.* PhD Thesis, University of Oslo, 2009.

[53] H.D. Young and R. A. Freedman. *Sears and Zemansky's University Physics with Modern Physics.* Pearson Education, 11 edition, 2004.

[54] E.H. Hall. On a New Action of the Magnet on Electric Currents. *American Journal of Mathematics*, 2(3):287–292, 1879.

[55] R. Chwang, B. J. Smith and C. R. Crowell. Contact size effects on the van der Pauw method for resistivity and Hall coefficient measurement. *Solid-State Electronics*, 17(12):1217–1227, 1974.

[56] M. Kvalbein. Electrical Transport Mechanisms in Hydrothermal ZnO. Masters thesis, University of Oslo, June 2010.

[57] O. Stenzel. *The Physics of Thin Film Optical Spectra: An Introduction*, volume 44. Springer Verlag, 2005.

[58] M. Ohring. *The Materials Science of Thin Films.* Academic Press, 1992.

[59] D.G. Brandon, W.D. Kaplan, and D. Brandon. *Microstructural Characterization of Materials.* Wiley Online Library, 1999.

[60] L.B. Valdes. Resistivity Measurements on Germanium for Transistors. *Proceedings of the IRE*, 42(2):420–427, 1954.

[61] F. M. Smits. Measurement of sheet resistivities with the four-point probe. *Bell Syst. Tech. J*, 37(3):711–18, 1958.

[62] T. Tsuji and M. Hirohashi. Influence of oxygen partial pressure on transparency and conductivity of RF sputtered Al-doped ZnO thin films. *Applied surface science*, 157(1-2):47–51, 2000.

[63] U. Ozgur, Y. I. Alivov, C. Liu, A. Teke, M. A. Reshchikov, S. Dogan, V. Avrutin, S. J. Cho, and H. Morkoc. A comprehensive review of ZnO materials and devices. *Journal of Applied Physics*, 98:041301, 2005.

[64] R. Schifano, E. V. Monakhov, B. G. Svensson, W. Mtangi, P. Janse van Rensburg, and F. D. Auret. Shallow levels in virgin hydrothermally grown n-type ZnO studied by thermal admittance spectroscopy. *Physica B: Condensed Matter*, 404(22):4344–4348, 2009.

[65] R.H. Bube. Electronic Transport in Polycrystalline Films. *Annual Review of Materials Science*, 5(1):201–224, 1975.

[66] D. C. Look. Recent Advances in ZnO Materials and Devices. *Materials Science and Engineering B*, 80(1-3):383–387, 2001.

[67] V. E. Henrich and P. A. Cox. *The Surface Science of Metal Oxides*. Cambridge University Press, 1996.